Computational Fluid Dynamics investigation of a Single Screw Extruder: A flow and heat transfer analysis

Politecnico di Torino

Master of Science in Chemical and Sustainable Processes Engineering

Candidate:

Nicola D'Intinosante

Supervisors:

Prof. Marco Vanni

Dr. Graziano Frungieri

December 2020

To my "Ciao brutto gufo, da dove vieni? da Moscufo?"
hardworking Dad Fabrizio,
my philosophical and great reader Mum Filomena
and my "little" brilliant Sister Marina

Riassunto del lavoro di tesi

Lo scopo di questa tesi era quello di realizzare un modello 3D per studiare il comportamento fluidodinamico di un estrusore monovite. Per questo motivo sono state eseguite sia simulazioni isoterme che simulazioni non isoterme e per far ciò si è sfruttato il software ANSYS Polyflow v19.0. Risolvendo sia l'equazione di trasporto del momento sia quella del trasporto di energia è stato possibile studiare il campo di moto ed il trasferimento di calore all'interno dell'estrusore. In aggiunta, siccome la geometria assegnataci è caratterizzata dall'interruzione del filetto, si è voluto analizzare se queste interruzioni avessero in qualche modo delle influenze sul comportamento del fluido. Nel modello CFD il materiale preso in cosiderazione è un polimero della classe shear-thinning ed è considerato totalmente fuso. Infatti è importante sottolineare che durante le simulazioni si è trascurato il passaggio di fase da pellets solidi a polimero fuso. In aggiunta alcune ipotesi semplificative sono state fatte per non complicare troppo il modello e appesantire le simulazioni: densità costante del fluido, dipendenza della viscosità dalla temperatura trascurata. Per eseguire delle simulazioni stazionarie si è sfruttata la simmetria presente all'interno del nostro modello. Infatti sfruttando la tecnica del "rotating reference frame" l'asse di riferimento è stato posizionato sulla vite e si è fatto ruotare il barrel. In questo modo il dominio di fluido non cambia nel tempo e le simulazioni stazionarie possono essere eseguite. L'adozione di questo stratagemma equivale a simulare un sistema con vite in rotazione e barrel fermo, utilizzando un sistema di riferimento non rotante. Il lavoro totale è stato suddiviso in quattro capitoli. Nel Capitolo 1 si è eseguita un'introduzione al "polymer processing" e all'estrusore monovite. Il Capitolo 2 spiega l'approccio utilizzato per realizzare il modello partendo dalla realizzazione delle geometrie e delle meshes fino ad arrivare al setup delle simulazioni. Il Capitolo 3 riporta i risultati ottenuti sia per le simulazioni isoterme sia per le non isoterme. Infine il lavoro si conclude con il Capitolo 4 dove appunto sono riportate le conclusioni analizzando i punti di forza del modello e gli studi aggiuntivi che potrebbero essere applicati in un ipotetico futuro.

Introduzione

In tutti gli strumenti utilizzati nel "polymer processing" è possibile individuare degli steps comuni:

1. Fusione: Il polimero deve essere fuso e per questo motivo è necessario trovare la configurazione geometrica ottimale dello strumento che permetta di ottenere le migliori condizioni di fusione.

2. Pressurizzazione: Il polimero fuso deve essere trasportato fino alla testa di estrusione e per far ciò è necessario che un incremento di pressione venga generato all'interno dell'estrusore. Questo step è completamente controllato dalle proprietà reologiche del fluido.

3. Miscelazione: Il polimero fuso è miscelato dal prevalente moto laminare presente all'interno dell'estrusore dovuto all'alta viscosità del polimero stesso. Le operazioni di miscelazione permettono di uniformare la temperatura del polimero fuso.

L'estrusore monovite è stato per molti anni e lo è tuttora uno degli strumenti più utilizzati nell'industria dei polimeri. I suoi punti di forza sono il suo costo relativamente contenuto, la sua semplice configurazione e la sua affidabilità.

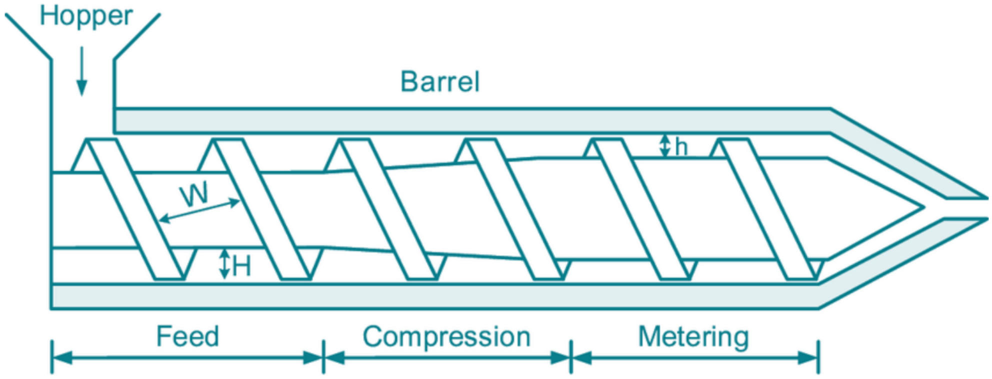

Figure 1: Rappresentazione di un estrusore monovite.

L'estrusore monovite (Figura 1) è costituito da un cilindro cavo (barrel) che molto spesso viene riscaldato tramite resistenze. La superficie interna del cilindro è rivestita da un metallo per limitare l'usura dato che durante il processo si raggiungono alte temperature. La configurazione dell'estrusore si completa grazie alla presenza di una vite all'interno del barrel che è la chiave del processo di fusione. Infatti in base alle principali caratteristiche della vite quali la lunghezza, la presenza di interruzioni del filetto, il diametro è possibile agire in modo diretto sulle condizioni termiche del fuso. In generale la vite di un estrusore è costituita da tre sezioni differenti:

1. Zona di alimentazione: Il materiale entra all'interno del sistema tramite delle tramogge e lo fa sfruttando la gravità. Una volta che è entrato all'interno dell'estrusore il materiale si troverà nella sezione anulare tra la vite ed il barrel che la circonda. La vite ruota ed il barrel è mantenuto fermo. Nel momento in cui il sistema è in funzione, le forze di attrito generate sia sulle pareti del barrel che su quelle della vite agiranno sul polimero e sono responsabili sia del trasporto del materiale stesso (fino a che il materiale resta al di sotto della sua temperatura di fusione) sia della generazione di calore per dissipazione viscosa. Man mano che il polimero viene spinto in avanti si riscalderà e nel momento in cui supera la temperatura di fusione ha inizio la zona di plastificazione.

2. Zona di compressione o plastificazione: Per plastificazione si intende il passaggio di stato da polimero solido a polimero fuso. L'azione di sfregamento tra polimero e barrel e tra polimero e vite genera calore. L'azione combinata tra calore generato per dissipazione viscosa e calore introdotto dal barrel riscaldato, permette al polimero di raggiungere la temperatura di fusione e di raggiungere la condizione di polimero fuso. Man mano che il materiale viene

spinto in avanti, la quantità di solido presente è sempre minore a favore della formazione di polimero fuso. Quando il polimero solido è scomparso del tutto la zona di misurazione ha inizio.

3. Zona di dosaggio: In questa zona è presente esclusivamente polimero fuso, il quale viene movimentato e trasportato dal drag flow e dal pressure flow. Il bilancio tra questi due termini restituisce la portata finale di polimero fuso in uscita. Nella zona di misurazione il polimero fuso viene pompato verso la testa di estrusione. Nel momento in cui il polimero fuso passerà all'interno della testa, assumerà la forma di quest'ultima. Siccome la testa di estrusione esercita una resistenza è necessario generare un incremento di pressione all'interno dell'estrusore affinché il polimero raggiunga la parte finale.

Metodi

Il presente lavoro è stato suddiviso in quattro fasi principali, le quali sono riportate nello schema mostrato in Figura 2.

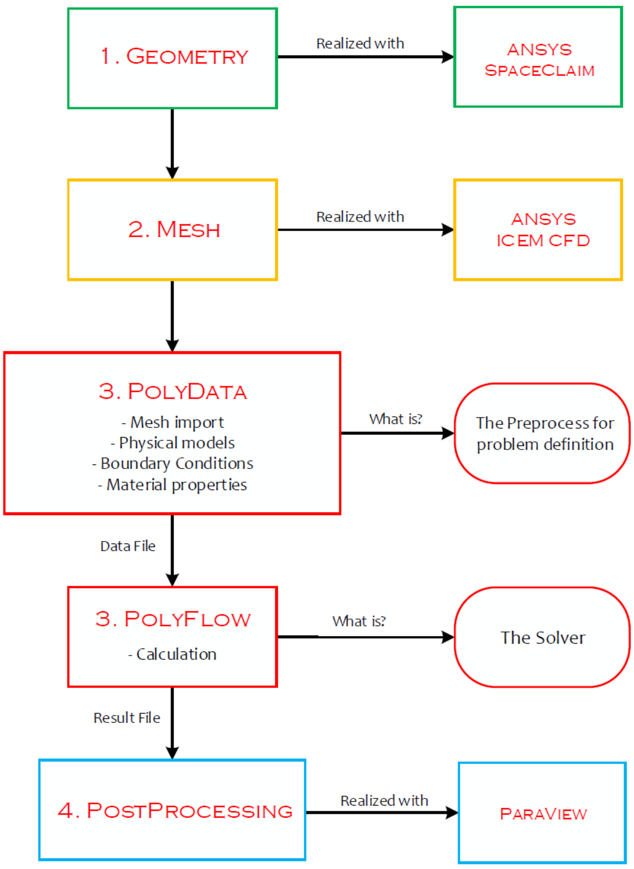

Figure 2: Schema di flusso della totale suddivisione del lavoro.

- Geometria: La prima fase è stata caratterizzata dalla realizzazione, tramite il software ANSYS SpaceClaim, della geometria richiesta da Continental AG. La geometria creata è un modello 3D che rappresenta un estrusore realmente esistente nei dipartimenti di ricerca dell'azienda.

- Mesh: La seconda fase è stata caratterizzata dalla realizzazione della mesh sfruttando il software ANSYS ICEM CFD. Dopo la realizzazione della mesh le quattro "boundary surfaces" (Inlet, Outlet, Barrel and Screw) sono state create.

- Simulazioni: Il software utilizzato per realizzare le simulazioni è ANSYS Polyflow. Questo programma ci ha permesso di risolvere l'equazione di trasporto del momento e l'equazione di trasporto di energia tramite l'utilizzo del metodo degli elementi finiti.

- PostProcessing: La fase finale è stata caratterizzata dall'analisi del risultati ottenuti dalle simulazioni. Per far ciò è stato sfruttato il software chiamato Paraview che ci ha permesso di estrapolare i contour plots delle principali proprietà fisiche del polimero.

Geometria

Sfruttando ANSYS SpaceClaim sono stare realizzate due geometrie 3D, caratterizzate dai seguenti parametri comuni:

- L = Lunghezza assiale della vite = 90 cm

- δ_f = Gap = 1 mm

- D_s = Diametro della vite = 90 mm

- D_b = Diametro del barrel calcolato come $D_b = D_s + 2\delta_f = 92$ mm

Le principali caratteristiche delle due geometrie sono riportate di seguito:

1. *Nominal screw geometry*: Questa geometria è quella richiesta dall'azienda e la principale caratteristica di questa geometria è il fatto che la vite è caratterizzata dall'interruzione del filetto.

2. *Full screw geometry*: Per capire se le interruzioni del filetto avessero delle influenze sul comportamento del polimero fuso, questa seconda geometria è stata generata. Quest'ultima è caratterizzata da un filetto continuo della vite e per questo motivo è chiamata *Full screw geometry*.

Per completare le geometrie, un barrel cilindrico contenente la vite è stato introdotto. Il barrel è stato disegnato in modo da garantire che la distanza minima tra la vite e lo stesso barrel (gap) fosse di un millimetro. In Figura 3 la *Nominal screw geometry* viene mostrata con il rispettivo barrel.

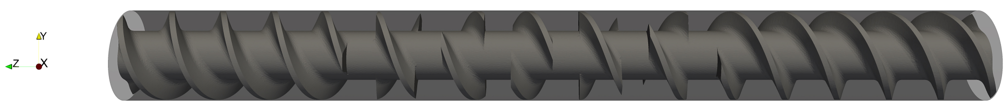

Figure 3: Rappresentazione 3D della *Nominal screw geometry* circondata dal barrel

Allo stesso modo in Figura 4 viene mostrata la *Full screw geometry*:

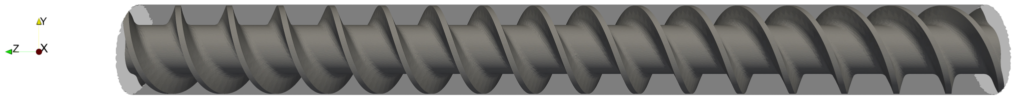

Figure 4: Rappresentazione 3D della *Full screw geometry* circondata dal barrel

L'ultimo passaggio che è stato eseguito su ANSYS SpaceClaim è stato quello di estrapolare il volume di fluido presente tra la superficie esterna della vite e la superficie interna del barrel. Proprio questo volume di fluido è quello che è stato meshato.

Mesh

In questo lavoro si è sfruttata una mesh ibrida costituita da elementi tetraedrici e prismatici. Infatti nel dominio di fluido possono essere individuate due zone principali:

1. Gap tra la vite ed il barrel: Questa viene considerata una zona critica perchè lo spessore della zona stessa è molto contenuto (1 mm). Infatti nel momento in cui una mesh costituita da elementi tetraedrici viene applicata sull'intero modello, in questa zona il numero di nodi generati (dove il solver risolve le equazioni di trasporto) è basso. Questo può risultare in errori o inaccuratezza durante la risoluzione delle equazioni. Per questo motivo nelle zone critiche è stato necessario introdurre una mesh più raffinata e caratterizzata da prismi, in modo da ottenere un numero più alto di nodi.

2. Bulk del fluido: Questa zona non necessita la stessa accuratezza della precedente e per questo motivo è stato sufficiente inserire una mesh caratterizzata da elementi tetraedrici.

In Figura 5 entrambe le zone con le rispettive mesh vengono mostrate.

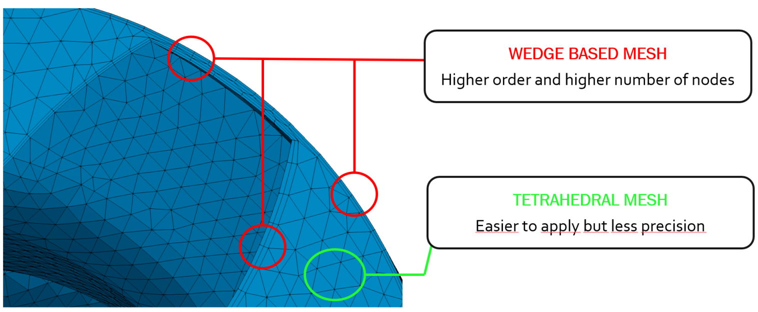

Figure 5: Dettagli delle due zone con le loro mesh.

Può essere visto che adottando questo approccio, un numero più alto di elementi è stato generato nel gap e nelle regioni vicino alla vite rispetto al bulk del fluido. In Figura 6 un dettaglio della mesh è mostrato tramite una rappresentazione basata sui nodi presenti nel dominio di fluido.

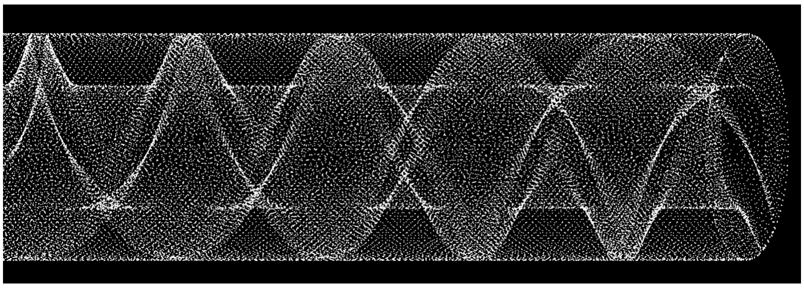

Figure 6: Discretizzazione del volume di fluido grazie ad una rappresentazione dei nodi.

Per quanto riguarda la *Nominal screw geometry* maggiori informazioni riguardo la mesh generata sono riportate di seguito:

$$\text{Numero di volumi} = 2245946$$

$$\text{Numero di facce} = 4863229$$

$$\text{Numero di nodi} = 601420$$

Le stesse informazioni sono riportate per la *Full screw geometry*:

$$\text{Numero di volumi} = 2227608$$

$$\text{Numero di facce} = 4841799$$

$$\text{Numero di nodi} = 607557$$

Dopo la creazione della mesh, sulle due geometrie è stato necessario definire le quattro boundary sections. "Inlet" and "Screw" boundary sections sono mostrate in Figura 7 mentre "Outlet" and "Barrel" boundary sections sono mostrate in Figura 8.

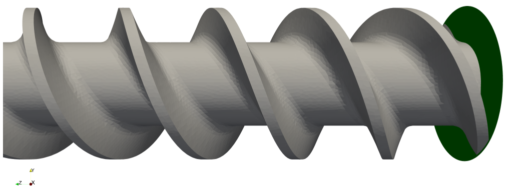

Figure 7: Inlet (verde) e Screw (grigio) boundary sections.

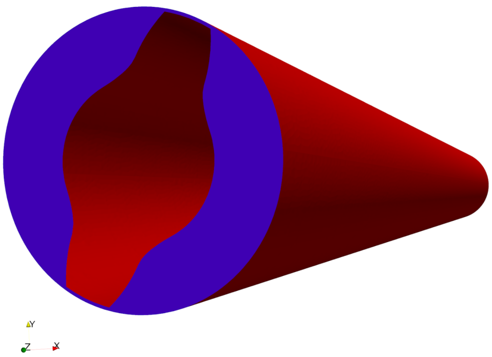

Figure 8: Outlet (blu) e Barrel (rosso) boundary sections.

Una volta che le meshes sono state generate e le boundary sections sono state create è stato possibile procedere alla realizzazione delle simulazioni.

Simulazioni

Per eseguire le simulazioni si è sfruttato il programma ANSYS Polyflow v19.0, software di fluidodinamica computazionale (CFD) che sfrutta il metodo degli elementi finiti per simulare situazioni dove la reologia del fluido ricopre un ruolo molto importante. Più precisamente questo programma viene sfruttato per risolvere problemi nei processi dei polimeri e delle plastiche. I calcoli relativi a questi processi sono basati su meccaniche dei fluidi non Newtoniani. Infatti su Ansys Polyflow è possibile utilizzare la categoria Generalized Newtonian Flow che include sia fluidi Newtoniani che non Newtoniani. Le analisi eseguite tramite questo software possono essere isoterme o non isoterme, le geometrie 2D o 3D. ANSYS Polyflow si è rivelata un'ottima scelta per la nostra analisi perchè offre la possibilità di eseguire complesse simulazioni riguardo la coestrusione di diversi fluidi o appunto l'estrusione in tre dimensioni. Per quanto riguarda il fluido si è imposta una dipendenza della viscosità dallo shear rate ed in particolare si è adottata una legge di potenza:

$$\eta = K \cdot \dot{\gamma}^{n-1} \tag{1}$$

Where:

- K = indice di consistenza
- $\dot{\gamma}$ = shear rate
- n = indice della legge di potenza che è una proprietà del materiale analizzato

In Figura 9 viene mostrata la curva viscosità-shear rate sperimentale del polimero in analisi.

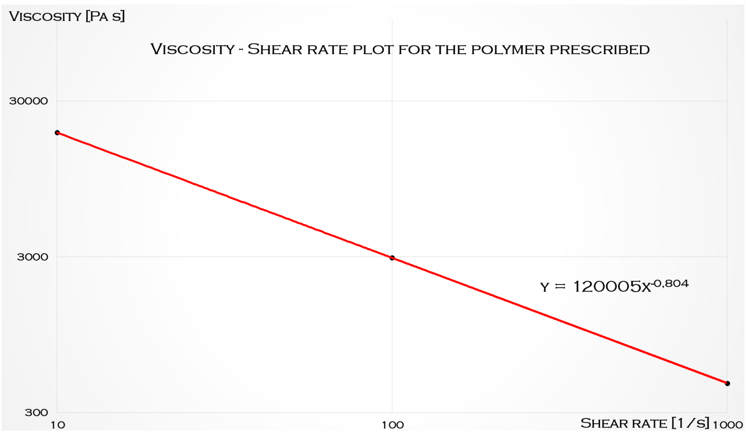

Figure 9: Grafico viscosity-shear rate derivante da dati sperimentali per il polimero in analisi.

I dati sperimentali sono rappresentati dai punti neri mentre la linea rossa rappresenta la legge di potenza che si è sfruttata per interpolarli. Interpolando con la legge di potenza i dati sperimentali forniti, la comune decisione è stata di impostare i seguenti parametri per la legge di potenza:

$$n = 0,1957$$

$$K = 120000 \ \mathrm{N\,s^n\,m^{-2}}$$

Risolvere un problema in ANSYS Polyflow richiede la definizione delle condizioni al contorno. Quelle relative al campo di moto necessarie alla risoluzione dell'equazione di trasporto del momento sono mostrare in Figura 10:

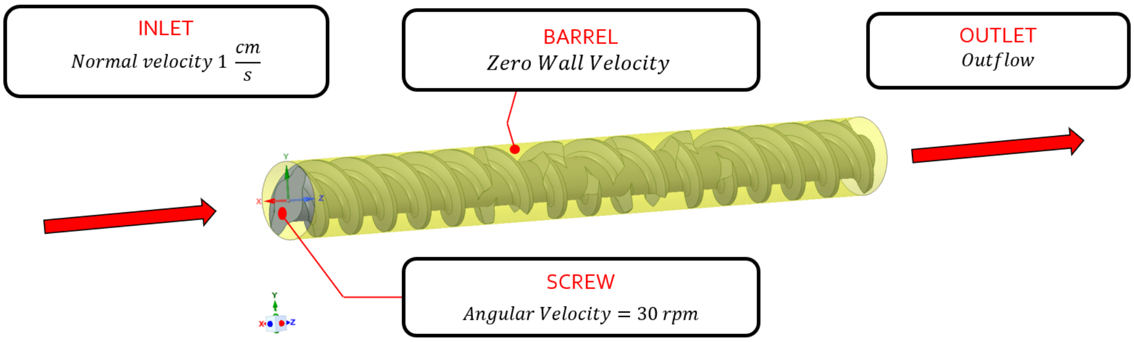

Figure 10: Rappresentazione delle condizioni al contorno per simulare il campo di moto

- Inlet: Alla boundary section "Inlet" è stata imposta la condizione "Inflow" che ci permette di specificare una portata massica o volumica che passa attraverso la boundary section. Più precisamente, per definire la portata volumica, l'input introdotto all'interno del simulatore è stato la velocità di ingresso del fluido ($\frac{\mathrm{cm}}{\mathrm{s}}$). Per le simulazioni principali la velocità di ingresso del fluido è stata fissata ad 1 $\frac{\mathrm{cm}}{\mathrm{s}}$ che corrisponde ad una portata volumica di $0.37449 \cdot 10^{-4} \frac{\mathrm{m}^3}{\mathrm{s}}$.

- Barrel: Alla boundary section "Barrel" è stata imposta la condizione "Cartesin Velocity Condition (v_x, v_y, v_z)". Nel momento in cui si seleziona questa opzione è necessario specificare il 1^{st} ed il 2^{nd} punto dell'asse di riferimento e la velocità angolare. Nel presente lavoro la rotazione del barrel è stata fissata attorno all'asse z e per le principali simulazioni abbiamo fatto ruotare il barrel ad una velocità angolare di 30 rpm. Nonostante si faccia girare il barrel, grazie al sistema di riferimento rotante posizionato sulla vite, vediamo la stessa vite girare a 30 rpm nel postprocessing.

- Screw: Alla boundary section "Screw" è stata imposta la condizione "Zero wall velocity ($v_n = v_s = 0$)". v_n rappresenta la componente normale della velocità e v_s rappresenta la componente tangenziale della velocità (in 3D v_s è un vettore con due componenti). Questa condizione è stata imposta alla vite, la quale è mantenuta fissa ma risulta essere in movimento quando si analizzano i risultati nel postprocessing.

- Outlet: Alla boundary section "Outlet" è stata imposta la condizione "Outflow". Questa condizione permette al simulatore di capire dove il fluido sta uscendo dal dominio computazionale.

In aggiunta alla condizioni al contorno per il campo di moto, per simulare un sistema non isotermo e per risolvere l'equazione di trasporto dell'energia è stato necessario introdurre le condizioni al contorno relative al trasporto di calore (Figura 11):

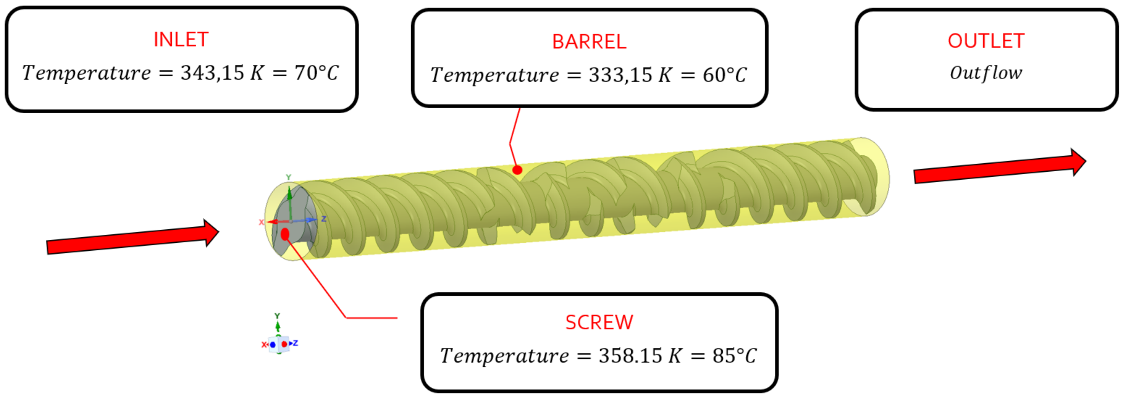

Figure 11: Rappresentazione delle condizioni al contorno per simulare il trasferimento di calore.

- Inlet: Alla boundary section "Inlet" è stata imposta la condizione "Temperature imposed". In particolare una temperatura costante di 343,15 K (70° C) è stata introdotta per il fluido entrante nel dominio computazionale.

- Barrel: Alla boundary section "Outlet", allo stesso modo, è stata imposta la condizione "Temperature imposed". Analizzando le realistiche condizioni operative dell'estrusore monovite si è deciso di fissare la temperatura a 333,15 K (60° C).

- Screw: La condizione "Temperature imposed" è stata assegnata anche alla boundary section "Screw" impostando un valore di temperatura di 358,15 K (85° C) basandosi sulle realistiche condizioni operative dell'estrusore monovite investigato.

- Outlet: Alla boundary section "Outlet" è stata imposta la condizione "Outflow". Similmente per quanto riguarda le condizioni al contorno per il campo di moto questa condizione permette al simulatore di capire dove il dominio computazionale finisce.

In aggiunta alle condizioni introdotte finora, all'interno di ANSYS Polydata, è stato necessario introdurre delle proprietà aggiuntive riguardanti il fluido:

- Dipendenza della viscosità dalla temperatura: A differenza della dipendenza della viscosità dallo shear rate questa opzione è stata trascurata e la viscosità è stata considerata indipendente dalla temperatura.

- Densità: L'ipotesi di fluido incomprimibile è stata fatta e per questo motivo si è impostata una densità costante. In particolare alcuni dati sperimentali relativi alla variazione della densità in funzione della temperatura sono stati ricevuti dai ricercatori della Continental AG e si è deciso di fissare la densità ad un valore di 1170 $\frac{\text{kg}}{\text{m}^3}$.

- Termini relativi all'inerzia: Questi sono stati presi in considerazione e l'opzione "Inertia will be taken into account" è stata selezionata was selected.

- Conduttività termica: Un valore costante è stato imposto per questa proprietà ed in particolare è stato imposto un valore di 0,40 $\frac{\mathrm{W}}{\mathrm{m \cdot K}}$. Questo è un tipico valore adottato nella letteratura riferita al melt processing (Questo valore è stato preso dagli esempi forniti con ANSYS Polyflow) ed è stato confermato essere, dai ricercatori della Continental AG, una buona apporssimazione della realistica conduttività termica del polimero analizzato.

- Capacità termica per unità di massa: Un valore costante è stato imposto per questa proprietà ed in particolare un valore di 1600 $\frac{\mathrm{J}}{\mathrm{kg \cdot K}}$ è stato selezionato.

- Calore generato per dissipazione viscosa: Generalmente questa opzione è trascurata nell'equazione di trasporto dell'energia. Per aggiungerla e per tenerla in considerazione è stato necessario selezionare "Viscous + wall friction heating will be taken into account".

- Termini relativi alla gravità: Questa opzione è stata trascurata durante le simulazioni.

Dopo che il problema è stato definito in ANSYS Polydata e una volta che ANSYS Polyflow ha terminato la computazione, un file di risultato è stato generato e la fase di postprocessing è iniziata.

Postprocessing

Per analizzare i risultati ottenuti durante le simulazioni il software Paraview è stato sfruttato. La flessibilità di questo programma lo ha reso noto tra le aree relative alle scienze computazionali come ad esempio la fluidodinamica o la astrofisica, le quali sfruttano metodi di risoluzione come gli elementi finiti o i volumi finiti. Questo software è in grado di leggere il file nel formato Ensight generato come "file.case" da ANSYS Polydata. Una volta introdotto il "file.case" del nostro modello all'interno del programma di postprocessing, Paraview ci permette di creare e applicare dei flitri per estrapolare determinati dati. In particolare grazie a questi filtri come ad esempio "Slice" or "Extract block" è stato possibile estrapolare i contour plots delle principali proprietà del fluido e immagini ad alta risoluzione del modello creato.

Risultati

I principali risultati estrapolati dalle simulazioni per entrambe le geometrie sono:

- Contour plots delle principali proprietà del fluido.

- Pressione in funzione della portata (linee caratteristiche della vite).

- Profili di temperatura.

Per ottenere i contour plots è stato necessario introdurre tre piani, i quali sezionano la vite:

- Slice 1 o Sezione 1; presa sul piano $z = 37$ cm.
- Slice 2 o Sezione 2; presa sul piano $z = 72$ cm.
- Slice 3 o Sezione 3; presa sul piano $x = 0$, il quale taglia la vita a metà.

Questa scelta è stata fatta per mostrare al meglio le principali differenze tra le zone dove il filetto della vite è presente e dove non lo è. Le tre sezioni realizzate sono mostrate nella Figura 12 e nella Figura 13.

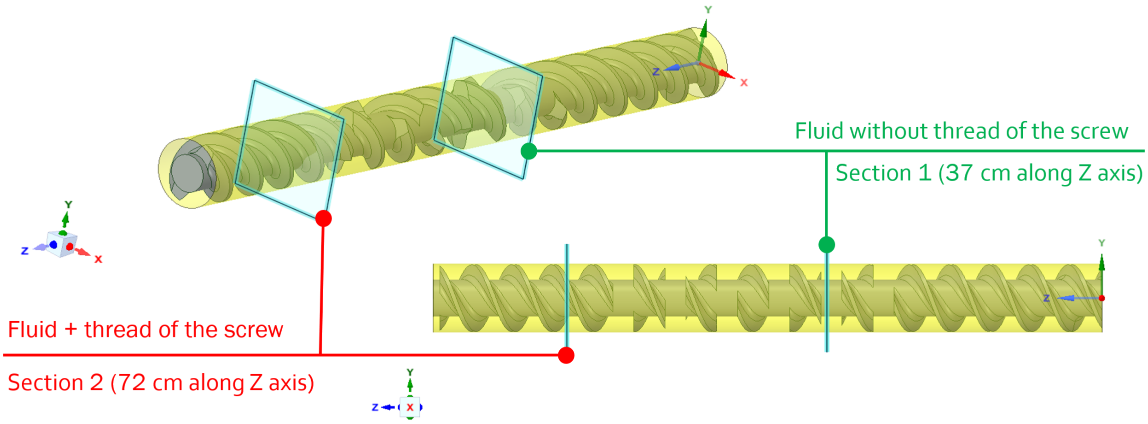

Figure 12: Posizione della Sezione 1 e della Sezione 2.

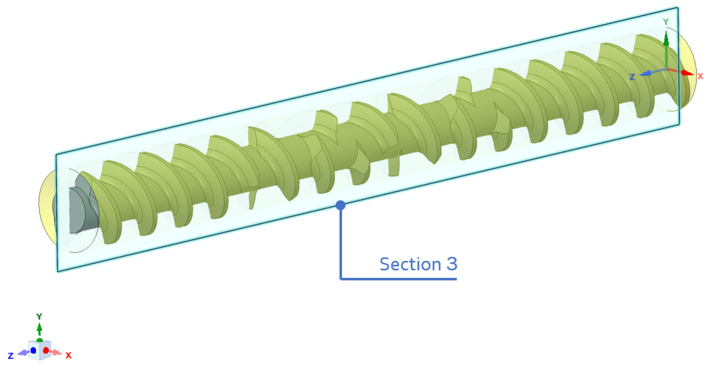

Figure 13: Posizione della Sezione 3.

Sia simulazioni isoterme che simulazioni non isoterme sono state portate avanti:

1. Simulazioni isoterme: In queste simulazioni esclusivamente l'equazione di trasporto del momento è stata risolta, trascurando il trasporto di calore. Da queste simulazioni sono stati estrapolati i contour plots relativi alla velocità, alla pressione e allo shear rate. In aggiunta le curve caratteristiche della vite sono state estrapolate per entrambe le geometrie.

2. Simulazioni non isoterme: In queste simulazioni la condizione non isoterma è stata introdotta per risolvere anche l'equazione di trasporto del calore. Da queste simulazioni è stato possibile estrapolare i contour plots relativi alla temperatura e al calore generato per dissipazione viscosa. In aggiunta, calcolando la temperatura media ponderata sull'area su diversi piani che sezionano la vite è stato possibile risalire alla variazione della temperatura media lungo l'estrusore.

Simulazioni isoterme

Il risultato più importante scaturito dall'analisi delle simulazioni isoterme è la presenza dell'effetto di backflow che si manifesta nella *Nominal screw geometry*. Una piccola porzione del fluido viaggia nella direzione opposta rispetto a quella del moto principale, favorendo fenomeni di miscelazione. Per visualizzare questo effetto è utile analizzare il contour plot della componente z della velocità sulla sezione 3 riportato nella Figura 14.

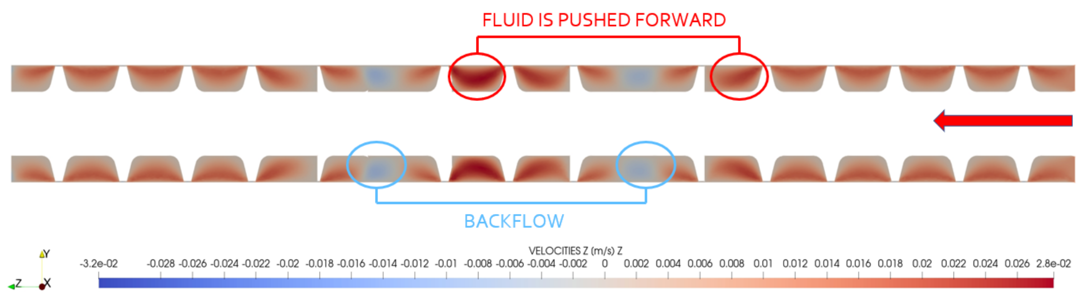

Figure 14: Contour plot della componente z della velocità sulla sezione 3 per la *Nominal screw geometry*.

Nella Figura 14 la componente z della velocità è caratterizzata dal colore rosso e dal colore blu. Approssimativamente, dove il colore è rosso la componente z è positiva ed il fluido è spinto nella direzione del moto principale. Al contratio, dove la componente è blu, il valore di questa proprietà è negativo e l'effetto di backflow è generato. Per capire in modo più approfondito questo fenomeno è necessario analizzare i due termini che costituiscono la portata netta di fluido:

$$Q = Q_d + Q_p \tag{2}$$

dove il primo contributo rappresenta il drag flow (Q_d) ed il secondo il pressure flow (Q_p). Il drag flow è la portata di fluido che si genera tra due superfici nelle quali una è in movimento rispetto all'altra. Nel caso in esame il fluido è letteralmente trascinato dal movimento del filetto della vite. Invece il pressure flow è la portata di fluido dovuta all'incremento di pressione generato all'interno dell'estrusore. Nelle zone dove il filetto della vita non è presente, il drag flow è più piccolo e il moto contrario a quello principale generato dal pressure flow può prevalere, causando l'effetto di backflow. È possibile confermare questo risultato guardando ai contour plot della componente z della velocità sulla sezione 1 (Figura 15) e sulla sezione 2 (Figura 16).

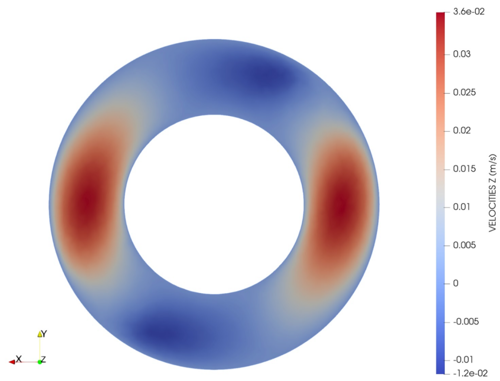

Figure 15: Contour plot della componente z della velocità sulla sezione 1 per la *Nominal screw geometry.*

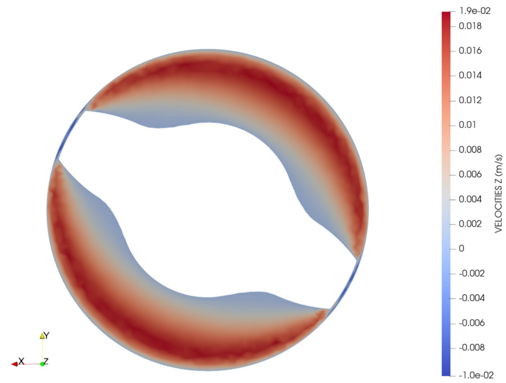

Figure 16: Contour plot della componente z della velocità sulla sezione 2 per la *Nominal screw geometry.*

È possibile notare che in Figura 15 (sezione 1 dove il filetto della vite non è presente) in diverse aree del dominio di fluido la componente z della velocità è negativa, dando origine al fenomeno di backflow. Al contrario in Figura 16 (sezione 2 dove il filetto della vite è presente) si può vedere che l'effetto di backflow è limitato esclusivamente alla zona del gap. In aggiunta la componente negativa della velocità z nel gap in Figura 16 è di un ordine di grandezza inferiore rispetto alla componente negativa della velocità z presente in Figura 15. Altra quantità che vale la pena di essere analizzata è lo shear rate che viene mostrato sulla sezione 1 (Figura 17) e sulla sezione 2 (Figura 18):

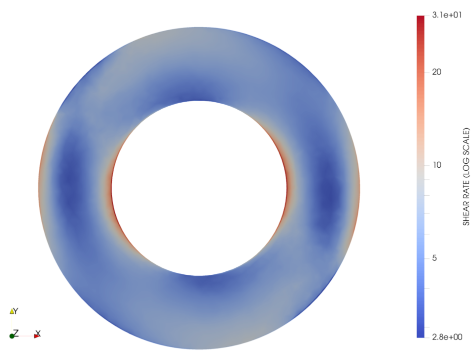

Figure 17: Contour plot dello shear rate $(\frac{1}{s})$ sulla sezione 1 per la *Nominal screw geometry.*

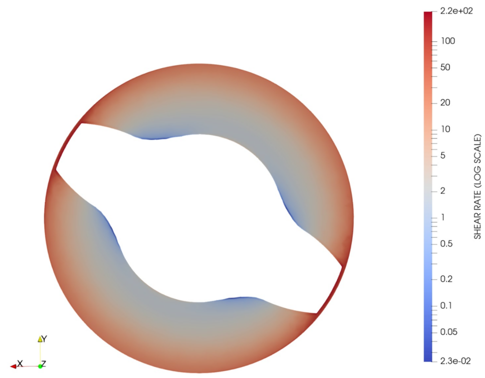

Figure 18: Contour plot dello shear rate $(\frac{1}{s})$ sulla sezione 2 per la *Nominal screw geometry.*

In entrambe le figure lo shear rate è riportato su scala logaritmica. In Figura 17 si nota che lo shear rate è all'incirca omogeneo su tutto il dominio di fluido. Siccome il filetto della vite non è presente il fluido non è forzato a seguire una determinata traiettoria ma è libero di circolare senza ostacoli. Per questo motivo lo shear rate assume dei valori relativamente alti solo nelle vicinanze delle pareti. Al contrario in Figura 18 (sezione 2) il filetto della vite obbliga il fluido a seguire una traiettoria prestabilita, forzandolo a passare all'interno del gap dove si rilevano i valori più alti dello shear rate. Altra proprietà che merita un'analisi è la pressione, della quale viene mostrato il contour plot relativo alla sezione 3 (Figura 19).

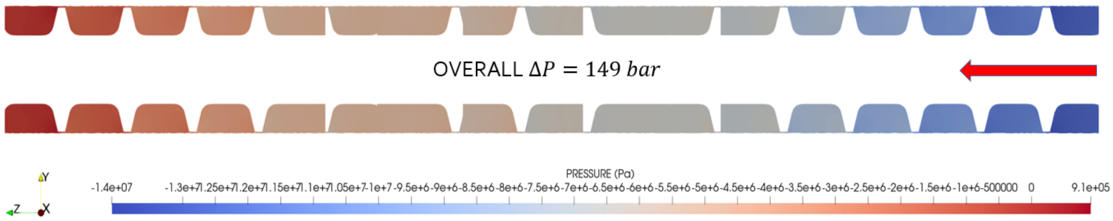

Figure 19: Contour plot della pressione ($\frac{1}{s}$) sulla sezione 3 per la *Nominal screw geometry*.

In Figura 19 l'incremento di pressione è calcolato tra l'ingresso e l'uscita del dominio di fluido. Il salto di pressione calcolato con il modello realizzato è di 149 bar, il quale valore corrisponde in modo adeguato al valore sperimentale (intorno ai 200 bar). Si nota che è presente un certo scostamento tra i due valori e questo può essere collegato al fatto delle ipotesi semplificative che sono state fatte (incompressibilità del fluido, dipendenza della viscosità dalla temperatura trascurata). Per concludere l'analisi sulla pressione nel caso della *Nominal screw geometry* è stata estrapolata la variazione della pressione media lungo l'estrusore (Figura 20):

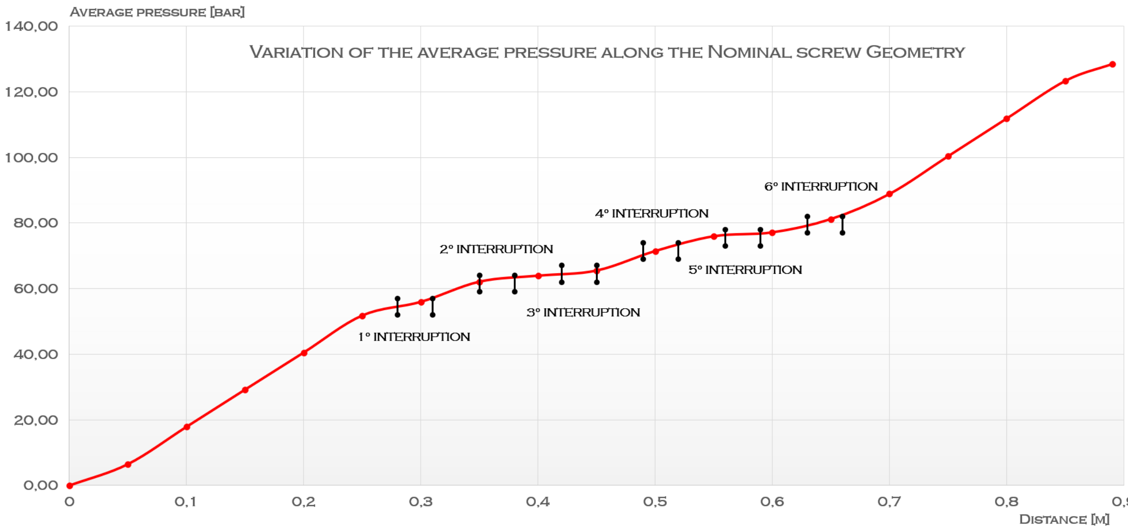

Figure 20: Variazione della pressione media lungo l'asse z della *Nominal screw geometry*.

È possibile notare che nelle zone dove il filetto della vite non è presente l'incremento della pressione è pressochè lineare e questo è dovuto al fatto che il fluido è esclusivamente spinto in avanti. Al contrario nelle zone dove il filetto della vite non è presente, il backflow è presente e per questo motivo l'incremento della pressione è più lento. Infatti le fluttuazioni che compaiono sull'andamento della pressione sono presenti esclusivamente nelle zone dove il filetto della vite è assente. La medesima analisi appena illustrata per la *Nominal screw geometry* è stata eseguita per la *Full screw geometry* mettendo in risalto le principali differenze. In Figura 21 viene riportato il contour plot della componente z della velocità sulla sezione 3:

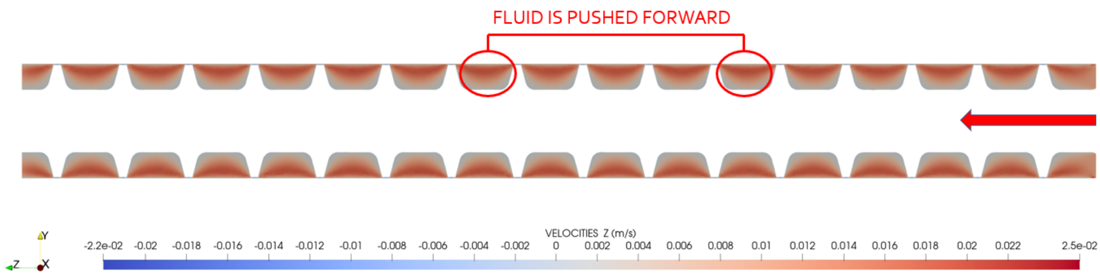

Figure 21: Contour plot della componente z della velocità sulla sezione 3 per la *Full screw geometry*.

Cade subito all'occhio che in questo caso l'effetto di backflow è praticamente assente se non esclusivamente limitato alle zone di gap. Per completare l'analisi viene mostrato il contour plot della pressione sulla sezione 3 (Figura 22):

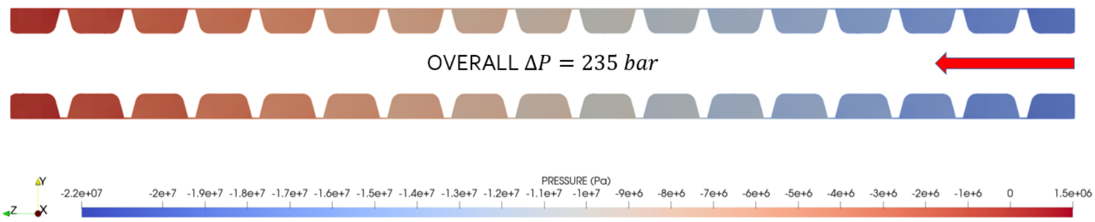

Figure 22: Contour plot della pressione $(\frac{1}{s})$ sulla sezione 3 per la *Full screw geometry*.

Il valore di pressione generato tra l'ingresso ed l'uscita del dominio di fluido in questo caso è di 235. Questo incremento nel salto di pressione rispetto al valore della *Nominal screw geometry* è sicuramente legato al fatto che il filetto è presente ovunque ed il fluido è costretto a seguire un percorso ben definito. Infatti, non essendoci interruzioni del filetto, il fluido viene esclusivamente trascinato dal moto della vite. Anche nel caso della *Full screw geometry* la variazione della pressione media lungo l'estrusore è stata estrapolata (Figura 23).

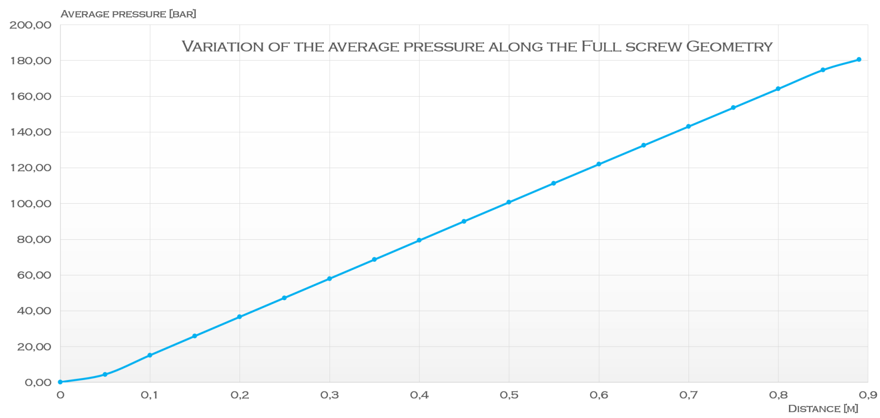

Figure 23: Variazione della pressione media lungo l'asse z della *Full screw geometry*.

In questo caso la pressione cresce linearmente lungo tutto l'asse z dell'estrusore e questo è dovuto al fatto che, come già è stato introdotto, esclusivamente il drag flow è presente.

Linee caratteristiche della vite

L'estrusore monovite generalmente è associato ad una testa di estrusione (die) e la portata netta dell'estrusore, così come il salto di pressione generato ad una certa velocità di rotazione sono dipendenti da entrambi gli strumenti come mostrato in Figura 24.

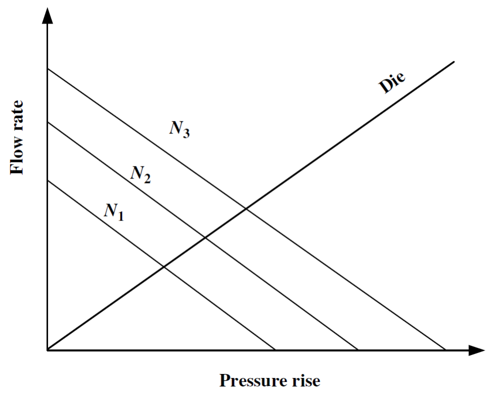

Figure 24: Linee caratteristiche della vite a tre differenti velocità di rotazione $N_1 < N_2 < N_3$ e la linea caratteristica del die.

La linea caratteristica di un estrusore ad una data velocità di rotazione è data da una linea retta (nel caso di fluido Newtoniano). La linea caratteristica del die è linearmente proporzionale alla caduta di pressione attraverso il die stesso. Le condizioni operative, alle quali corrispondono una determinata portata netta ed un determinato salto di pressione, è il punto di incontro tra le due linee caratteristiche degli strumenti. In questo lavoro si solo volute calcolare le linee caratteristiche della vite per entrambe le geometrie create. Per ottenere due diverse linee caratteristiche per ogni geometria la simulazione è stata eseguita a due velocità di rotazione del barrel diverse (rispettivamente 30 rpm e 60 rpm). Il valore della velocità del fluido in ingresso è stata variata in un range che andava da 0 a 1.5 $\frac{\text{cm}}{\text{s}}$ per le simulazioni eseguite a 30 rpm. Per quanto riguarda invece le simulazioni eseguite a 60 rpm la velocità in ingresso è stata variata in un range che andava da 0 a 2.5 1.5 $\frac{\text{cm}}{\text{s}}$. Cambiando la velocità in ingresso e conseguentemente la portata volumica del fluido è stato possibile calcolare il salto di pressione calcolato tra l'ingresso e l'uscita del dominio di fluido. Un riassunto delle condizioni introdotte per realizzare le simulazioni per entrambe le geometrie è riportato nella Figura 25 e nella Figura 26.

30 rpm	INLET VELOCITY [cm/s]	FLOW RATE [m3/s]	PRESSURE [bar]
	0,0	3,75E-07	395,8
	0,5	1,87E-05	276,0
	1,0	3,75E-05	138,6
	1,5	5,62E-05	48,0
		6,30E-05	0,0
60 rpm	INLET VELOCITY [cm/s]	FLOW RATE [m3/s]	PRESSURE [bar]
	0,0	3,75E-07	454,3
	0,5	1,87E-05	396,1
	1,0	3,75E-05	316,1
	1,5	5,62E-05	231,5
	2,0	7,49E-05	170,0
	2,5	9,36E-05	103,4
		1,32E-04	0,0

Figure 25: Velocità d'ingresso, portata volumica e incremento di pressione calcolato per le simulazioni sulla *Nominal screw geometry*.

30 rpm	INLET VELOCITY [cm/s]	FLOW RATE [m3/s]	PRESSURE [bar]
	0,0	3,75E-07	541,5
	0,5	1,87E-05	373,7
	1,0	3,75E-05	191,7
	1,5	5,62E-05	70,3
		6,75E-05	0,0
60 rpm	INLET VELOCITY [cm/s]	FLOW RATE [m3/s]	PRESSURE [bar]
	0,0	3,75E-07	621,6
	0,5	1,87E-05	538,3
	1,0	3,75E-05	428,0
	1,5	5,62E-05	315,1
	2,0	7,49E-05	219,5
	2,5	9,36E-05	144,0
		1,27E-04	0,0

Figure 26: Velocità d'ingresso, portata volumica e incremento di pressione calcolato per le simulazioni sulla *Full screw geometry*.

Siccome il valore della portata volumica alla quale il salto di pressione risultasse nullo non era noto a priori, è stato necessario estrapolare questo valore mediante interpolazione lineare. I valori riportati nelle tabelle delle Figure 25 e 26 sono stati riportati su un grafico mostrato in Figura 27.

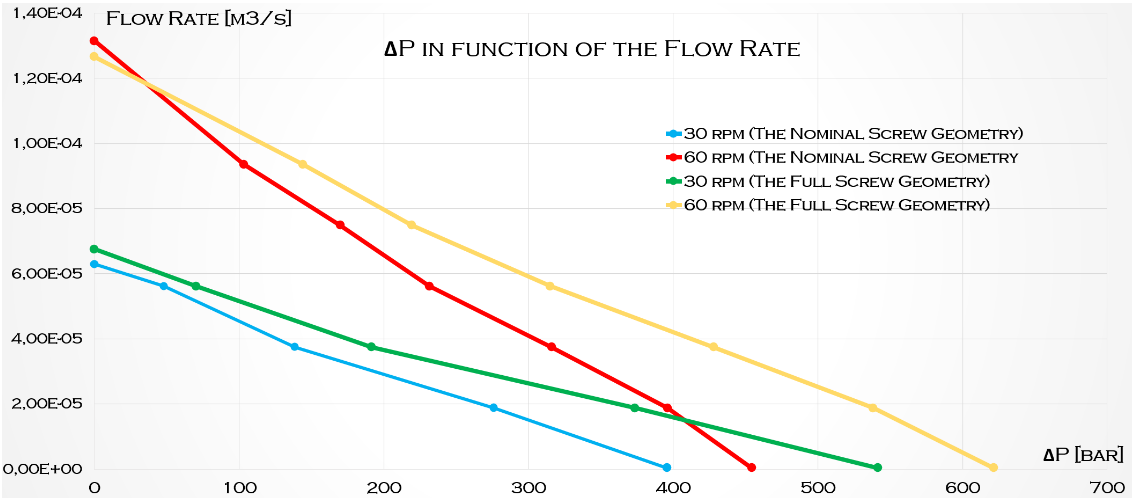

Figure 27: Confronto tra le curve caratteristiche della vite per entrambe le geometrie.

Differentemente dalle linee caratteristiche della vite riportate in Figura 24, in Figura 27 le linee non sono perfettamente delle rette e questo è dovuto al fatto che il fluido in esame presenta carattere non Newtoniano. Prese ad esempio le linee caratteristiche relative alla *Nominal screw geometry* è interessante notare che a parità di portata introdotta all'interno dell'estrusore, l'incremento di pressione generato a 60 rpm risulta più alto rispetto a quello generato a 30 rpm. La principale differenza tra le due geometrie ricade nell'incremento di pressione generato tra ingresso ed uscita. Infatti a parità di portata entrante, è possibile notare che le curve caratteristiche della *Full screw geometry* sono traslate a valori più alti di pressione rispetto a quelli della *Nominal screw geometry*.

Simulazioni non isoterme

Per analizzare nel migliore dei modi i profili di temperatura per prima cosa è necessario studiare i contour plots relativi al calore generato per dissipazione viscosa (Figura 28) e allo shear rate (Figura 29).

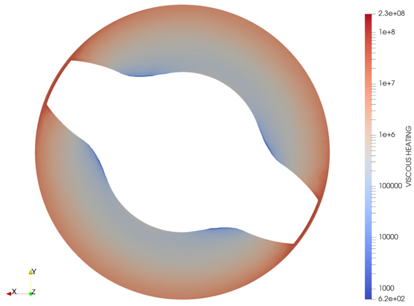

Figure 28: Contour plot del calore generato per dissipazione viscosa sulla sezione 2 per la *Nominal screw geometry*

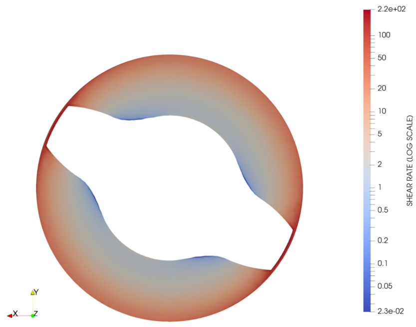

Figure 29: Contour plot dello shear rate sulla 2 per la *Nominal screw geometry*

I contour plots mostrati in Figur 28 ed in Figura 29 sono riferiti alla *Nominal screw geometry* ma lo stesso fenomeno accade in entrambe le geometrie. Si può notare che il calore generato per dissipazione viscosa (riportato su scala logaritmico) presenta i valori più alti nel gap dove anche lo shear rate mostra i suoi massimi valori. Questo vuol dire che dove è presente il filetto il calore generato per questo effetto è massimo. Adesso è possibile esaminare i contour plots della temperatura sulla sezione 3 per la *Nominal screw geometry* (Figura 30) e per la *Full screw geometry* (Figura 31):

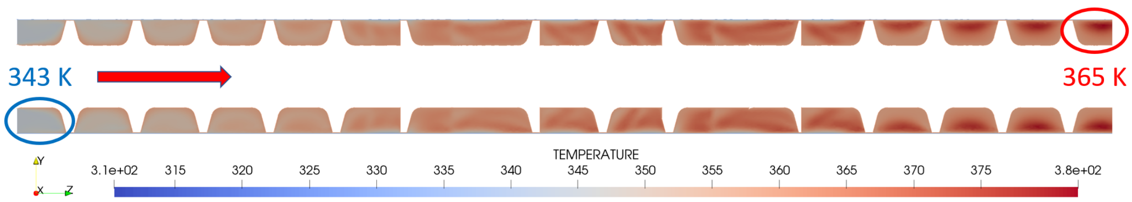

Figure 30: Contour plot della temperatura sulla sezione 3 per la *Nominal screw geometry*

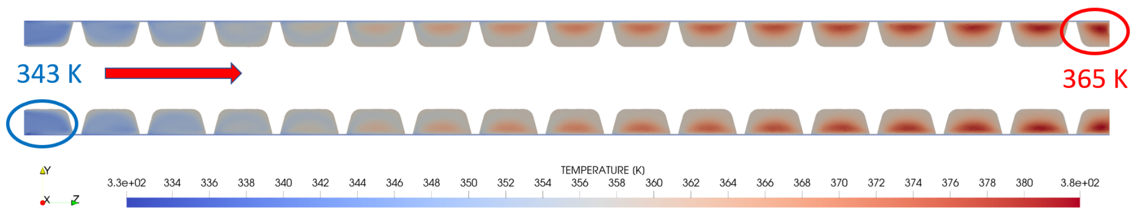

Figure 31: Contour plot della temperature sulla sezione 3 per la *Full screw geometry*

Si fa notare che in queste rappresentazioni la direzione del moto principale va da sinistra verso destra per facilitare il confronto con i profili di temperatura mostrati in Figura 32:

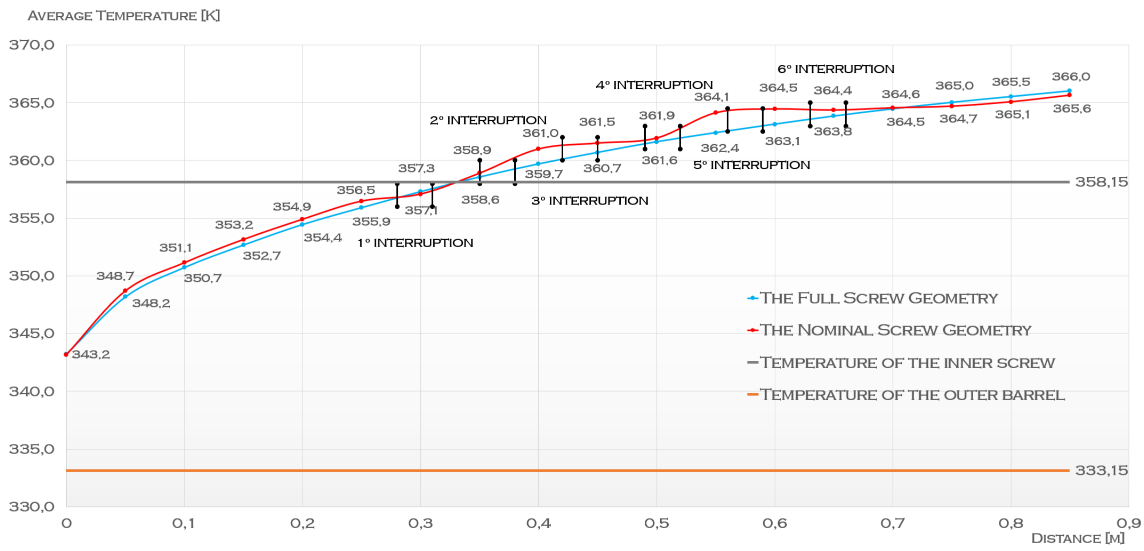

Figure 32: Confronto tra i profili di temperatura delle due geometrie.

In Figura 32 sull'asse delle ascisse è riportata la distanza lungo l'asse z (m) mentre sull'asse delle ordinate è mostrata la temperatura media del fluido. Per ottenere questo grafico è stato necessario calcolare il valore medio della temperatura ponderato sull'area su 18 piani paralleli ed equidistanti. In Figura 32 è importante notare che la variazione della temperatura non è costante lungo la direzione z dell'estrusore. Infatti se si analizza il grafico da sinistra verso destra si può vedere che fino ad una distanza di 35 cm il fluido presenta una temperatura media che è minore rispetto a quella della vite (riportata con la linea retta grigia). Questo significa che il fluido è riscaldato sia dal calore generato per dissipazione viscosa ma anche per effetto del trasferimento di calore da parte della vite. Una parte del calore totale acquistato dal fluido viene perso nel trasferimento di calore verso il barrel che presenta sempre una temperatura più bassa del fluido (riportata con la linea retta arancione). Per questo motivo nella prima sezione dell'estrusore il profilo della temperatura cresce con una pendenza maggiore. Al contrario, partendo da una distanza di 35 cm, il fluido presenta una temperatura che è sempre più alta rispetto a quella della vite. Questo vuol dire che una parte del calore generato per dissipazione viscosa è perso nel trasferimento di calore verso la vite ed il barrel. Questo fenomeno va avanti fino a quando il profilo di temperatura non raggiunge un plateau, dove la temperatura può essere considerata approssimativamente costante. A questo punto si ha un quasi equilibrio tra il calore generato per dissipazione viscosa e quello perso verso la vite ed il barrel. Adesso è possibile analizzare i due profili di temperatura relativi alle due geometrie. Per la *Nominal screw geometry* si può notare che il profilo presenta brusche variazioni della pendenza nei punti dove le interruzioni del filetto sono presenti. Infatti l'effetto di backflow generato in queste zone, andando nella direzione opposta rispetto al principale moto del fluido, aumenta la temperatura media del fluido. Al contrario la *Full screw geometry* non presenta le variazioni brusche nella pendenza del profilo perchè è caratterizzata da un filetto continuo della vite.

Conclusioni

Lo scopo di questo lavoro di tesi era quello di realizzare un modello CFD che potesse simulare uno degli strumenti presente nei dipartimenti di ricerca della Continental AG. Grazie all'analisi di modelli teorici e alla fluidodinamica computazionale (CFD) è stato possibile impostare sia delle simulazioni isoterme che non isoterme per il sistema in esame. Due geometrie sono state esaminate per capire al meglio la risposta del sistema: L'estrusore monovite utilizzato nei dipartimenti di ricerca, caratterizzato dall'interruzione del filetto della vite, è stato confrontato con una specifica geometria creata appositamente caratterizzata da un filetto continuo della vite. Durante il setup delle simulazioni si sono fatte delle ipotesi semplificative come l'incomprimibilità del fluido o il fatto di aver trascurato la dipendenza della viscosità dalla temperatura. Al contratio i termini legati all'inerzia e al calore generato per dissipazione viscosa sono stati tenuti in considerazione. Per eseguire delle simulazioni stazionarie si è sfruttata la tecnica del "rotating reference frame". Grazie al confronto tra i due modelli è stato possibile mettere in luce le principali caratteristiche della *Nominal screw geometry*, come ad esempio l'effetto di backflow e i profili di pressione e temperatura generati all'interno dell'estrusore. Infatti, differenti contour plots sono stati analizzati per far risaltare l'effetto del backflow sui profili di pressione e temperatura. Si è mostrato che nelle zone dove il filetto della vite non è presente l'effetto di backflow favorisce il mixing locale, risultanto in una distribuzione più omogenea della temperatura. Allo stesso tempo il backflow causa la variazione della pendenza dei profili di temperatura e di incremento di pressione. Si è trovato un accordo soddisfacente tra il modello creato e le attuali condizioni operative dell'estrusore. Per esempio, l'incremento di pressione previsto dal modello è intorno ai 150 bar rispetto a quello calcolato sperimentalmente che è intorno ai 200 bar. La differenza tra i due valori può essere collegata alle ipotesi semplificative fatte o al fatto che il fluido reale può avere delle componenti elastiche che non sono state considerate. Una sfida per gli studi su questo sistema può essere quella di aggiungere la dipendenza della viscosità dalla temperatura o la variazione della densità in funzione della temperatura. Questi effetti sono stati trascurati per ridurre la complessità delle simulazioni. Un'altra possibile risiede nel fatto di scegliere un'altra tecnica di risoluzione, come ad esempio la "superposition technique" o la "sliding mesh technique" per meglio valutare la qualità delle soluzioni.

Contents

List of Figures

Abstract

This work was realized in collaboration with the Continental AG Group with the aim to study the fluid dynamic behaviour of a single screw extruder (SSE) used in their R&D laboratories. The work was carried out using a computational fluid dynamics (CFD) code named ANSYS Polyflow which adopts the Finite Element Method (FEM) for discretising the transport equations. Two kind of geometries were realized: the one of interest to the Continental Group, referred to as the *Nominal screw geometry* and characterized by empty spaces interrupting the flight of the screw, and the *Full screw geometry*, similar to the previous one but with a continuous flight. This was made to evalutate the main differences between the two kind of SSEs. Both geometries were created using the CAD software ANSYS SpaceClaim and once generated, they were meshed using ANSYS ICEM CFD. In the CFD model, the material considered is a polymer treated as a non Newtonian fluid. It is really important to highlight that the simulations are not considering a plasticating extruder since the transition from solid to melt of processed polymer is neglected. In particular, a power law was used to model the shear rate dependence of the viscosity. On the contrary the depedence of the viscosity on the temperature was neglected. Both isothermal and non isothermal simulations were conducted to resolve both the momentum transport equation and the energy transport equation. To perform steady state simulations and thus reduce the computational cost, the rotating reference frame technique was adopted. In fact, by rotating the barrel and keeping fixed the screw, the shape of the flow domain does not change in time and stationary simulations are possible, provided that an opportune transformation of the system of reference is performed. During the simulation the inertia of the fluid and the viscous heating were took into account and the hypotesis of incompressible flow was made. By using postprocessing tools on the results of the simulations it was possible to obtain the contour plots of the main physical fields. In particular from the isothermal simulations the contour plots of velocity, pressure and shear rate were extrapolated. Results showed a substantial backflow effect into the *Nominal screw geometry*: a small portion of the fluid inside the extruder travels in the opposite direction of the main motion, thus enhancing mixing. From the non isothermal simulations the contour plots of the temperature and the viscous heating were extrapolated. By calculating the average temperature on different cutting planes it was possible to evaluate the variation of the temperature along the extruder. In addition, by varying the flow rate entering the system, it was possible to derive the screw characteristic lines (pressure rise as a function of the flow rate) which can be coupled with the die characteristic to find the operating point of the extruder. This point is the cross - point between the two characteristic lines and correspond to the flow rate and pressure value at which the system will operate. The comparison between the data obtained from the CFD simulations and the experimental data shows a good agreement both in the temperature profile and pressure increase.

1. Introduction

1.1 State of the art

The single screw extruder is one of the most commonly used devices in the industry to manufacture plastic elements and has been largely investigated, both theoretically and pratically, for over 50 years. The operation and design of this type of equipment is described in depth in a number of books and treatises, such as the texts by Tadmor and Klein [1], Rauweendal [2], Tadmor and Gogos [3], Fenner [4]. The seminal work for the modelling of the screw extruder is the paper of Griffith [5], who solved the governing equations for the flow of an incompressible fluid flow along the screw. Other examples of the earliest attempts of modeling flow and heat transfer based on the assumption of isothermal Newtonian fluid are reviewed in references [3] and [4]. The nonisothermal case with shear rate and temperature dependent viscosity was first tackled by Colwell and Nicholls [6]. The solution of the problem in the presence of cross channel flow was first presented by Griffith [5] and, subsequently, by Zamodits and Pearson [7]. The point to note is that these studies were concerned with hydrodynamically and thermally fully developed flows. The assumption of a hydrodynamically fully developed flow is reasonable because the very high viscosity of polymer melts inevitably results in a low Reynolds number. The thermally developing flow in a screw channel including downstream convection was analyzed by Fenner [8, 9], Elbirli and Lindt [10] and Lindt [11] who proposed a new solution for power-law fluids. Karwe and Jaluria [12] also studied thermal transport within the channel of a single screw extruder with given barrel termperature distribution and adiabatic screw. In all these models the flow channel is "unwrapped" from the screw to simplify the geometry. The design of single and twin screw extruders have been very limited due to the complexity of the system and the lack of advanced simulation softwares in the past. However, within the last decade, numerous computational fluid dynamic softwares have been developed and are applicable to varieties of products from plastic melts to flour based snack products. Numerical simulations provide an opportunity to study the mechanics of flow and mixing taking into account the actual complex geometry without performing the actual experiments. A detailed analysis on the metering zone of a single screw extruder was performed by Alemaskin and Manas-Zloczower [13], who introduced a particle tracking procedure to obtain information about the spatial distribution of particle tracers of two colors. Another important 3D study of a single screw extruder was conducted by Dhanasekharan and Kokini [14], who propose a computational method to obtain simultaneous scale up of mixing and heat transfer. 2D and 3D numerical studies of mixing efficiency in a pin mixing section of complex shape have been done by Yao et al. [15].

The aim of this thesis is to realize a 3D model to study the fluid dynamic behaviour of the single screw extruders (SSE) described in Chapter 3. For this reason isothermal and non isothermal simulations were carried out with ANSYS Polyflow v19.0 to resolve both the momentum transport and energy equations. In this way it was possibile to evaluate both the flow field and the heat transfer. In addition, since the geometry prescribed is characterized by the interruption of the flight of the screw we wanted to evaluate if these empty spaces have some influences on the behaviour of the fluid (mixing properties). In the CFD model, the material considered is a shear-thinning non Newtonian melt. It is really important to highlight that the simulations are not considering a plasticating extruder since the transition from solid to melt of processed polymer is neglected. In addition some simplifying assumptions were made: the density of the fluid was assumed constant, the temperature dependence of viscosity was neglected. On the contrary inertia terms and viscous heating of the fluid were took into account and a power law was used to model the shear rate dependance of the viscosity. To obtain steady state simulations, exploiting the axial simmetry of the barrel, a rotating reference frame was adopted. With this technique the reference frame was fixed on the screw and we let the barrel rotate. This is the equivalent to simulate a screw rotating with the barrel fixed in a non rotating reference frame. The advantage of this technique is the fact that the shape of the flow domain does not change in time and stationary simulations are possible. An analysis on the melt temperature rise in function of the reference frame was made by Habla1 et al. [16], who showed that the kinematics and the melt temperature rise are equal for screwand barrel rotation and thus independent of the reference frame. The total work is subdivided into 5 Chapters. In Chapter 1 an introduction to the polymer processing and to the single screw extruder is made, focussing on the mathematical model carried out by Tadmor [3]. Chapter 2 describes the adopted approach for the simularions, describing in detail each step. In Chapter 3 the results obtained from simulations are showed analysing both isothermal and non isothermal simulations. Finally, Chapter 4 contains the conclusions of the work.

1.2 Polymer processing

The first important step is to analyse the polymer processing [3] and to define its target. In this case, the objective is undoubtedly shaping polymer products. The shaping operation can be preceded and followed by many manipulations of the polymer to prepare it for shaping, modify its properties, and improve its appearance. Shaping of the polymer takes place only subsequent to a series of preparatory operations. The nature of these operations determines to a large extent the shape, size, complexity, choice, and cost of the processing machinery. One or more such operations can be found in all existing machinery, and we refer to them as elementary steps of polymer processing. There are five clearly identifiable elementary steps:

1. Handling of particulate solids: Subjects such as particle packing, agglomeration, consolidation, gravitational flow, arching, compaction in hoppers, and mechanically induced flow must be well understood to ensure sound engineering design of processing machines and processing plants.

2. Melting: Subsequent to an operation involving solids handling, the polymer must be melted or heat softened prior to shaping. Often this is the slowest, and hence the rate determining step in polymer processing. Severe limitations are imposed on attainable melting rates by the thermal and physical properties of the polymers, in particular, the low thermal conductivity and the thermal

degradation. The former limits the rate of heat transfer, and the latter places rather low upper bounds on the temperature and time the polymer can be exposed. On the other hand, beneficial to increasing the rate of melting, is the very high polymer melt viscosity, which renders dominant the role of the viscous energy dissipation as heat source term. All these factors emphasize the need to find the best geometrical configuration for obtaining the highest possible rates of melting, and for determining the processing equipment needed for rapid and efficient melting.

3. Pressurization and pumping: The molten polymer must be pumped and the pressure must be generated to bring for example the molten flow through dies or into molds. This elementary step, called pressurization and pumping, is completely dominated by the rheological properties of polymeric melts, and profoundly affects the physical design of processing machinery.

4. Mixing: The polymer melt is also mixed by the prevailing laminar flow. Mixing the melt distributively make it possible to obtain uniform melt temperature or uniform composition. Instead, dispersive mixing provides the breakup of agglomerates [17] and fillers.

5. Devolatilization and stripping: The last elementary step of devolatilization and stripping is of particular importance to postreactor compounding, blending, and reactive processing operations, although it also occurs in commonly used processes, for example, devolatilizing in vented two stage Single Screw Extruders.

After these elementary steps the shaping operation can be started. The selection of the shaping method is dictated by product geometries and sometimes, when alternative shaping methods are available, by economic considerations. Reviewing the various shaping methods practiced in the industry, the most important techniques are reported as follows:

1. Calendering and coating: The first shaping method is a steady continuous process. It is among the oldest methods, and is used extensively in the rubber and plastics industries. It includes the classic calendering, as well as various continuous coating operations, such as knife and roll coating.

2. Die forming: Die forming, which is perhaps the most important industrial shaping operation, includes all possible shaping operations that consist of forcing a melt through a die. Among these are fiber spinning, film and sheet forming, pipe, tube, and profile forming, and wire and cable coating.

3. Molding and casting: The next shaping method is molding and casting, which comprises all the different ways for stuffing molds with thermoplastics or thermosetting polymers. These include the most widely used shaping operations of injection molding, transfer molding, and compression molding, as well as the ordinary casting of monomers or low molecular weight polymers, and in situ polymerization

In the systems investigated in this thesis, a die forming tecnique is associated with the single screw extruder. In fact the melt is forced through a die to obtain the shape of a thin slab for the polymer extruded. However, the die has not been considered in the modelling , which is focused only on the operation of the screw.

1.3 Single screw extruder

The single screw extruder was for many years and it is still today the primary form of machine used in the polymer industry. Its key advantages are the relatively low costs, the straightforward design, the ruggedness, the reliability and a favorable performance/cost ratio.

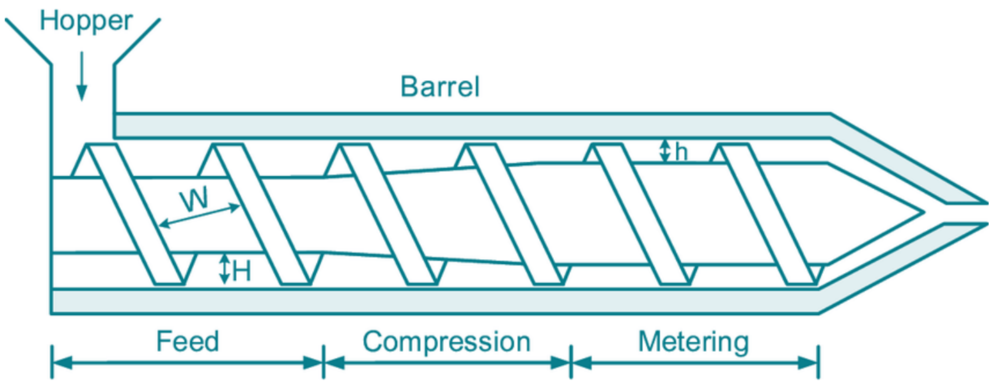

Figure 1.1: Cross section of a single screw extruder showing the main components and sections.

A single screw extruder (Figure 1.1) consists of a hollow cylindrical barrel fitted with external heaters. The inner barrel surface is coated with a hard metal liner to limit wear rates of the barrel and a compatible alloy hard wear surface can be added to the screw flights. A screw is fitted into this cylinder with a specific geometry determined by the polymer and the desired thermal condition of the melt. The screw design will determine the ultimate performance of the extrusion system and is rightly considered the heart of the extrusion process. The screw is driven by an electric motor through a gear reducer sized for the speed and power requirements of the screw. Barrel temperature is maintained by electric heaters, which often contain channels for cooling water. The extruder screw of a conventional plasticating extruder has three geometrically different sections [2]:

1. Feed section or solid conveying section of the screw: The material enters from the feed hopper and generally it flows down by gravity into the extruder barrel. Once the material falls down, it is situated in the annular space between the extruder screw and the barrel and it is further bounded by the passive and active flanks of the screw flight: the screw channel. The barrel is stationary and the screw is rotating. As a result, the frictional forces will act on the material, both on the barrel as well as on the screw surface and these forces are responsible for the forward transport of the material, at least as long as the material is in the solid state (below its melting point). In fact the material in this section will be mostly in the solid state. As the material moves forward, it will heat up as a result of frictional heat generation and because of heat conducted from the barrel heaters. When the temperature of the material

exceeds the melting point, a melt film will form at the barrel surface. This is where the solids conveying zone ends and the plasticating zone starts.

2. Compression or plasticating section of the screw: Plastication [18] is a term that represents the mechanical conversion of the solid polymer into a polymer melt. As the polymer is fed forward it is compacted by the forces generated by solid conveying frictional forces. As the solid is compacted into a compressed solid plug it is rubbed against the extruder barrel. The rubbing action generates heat, which, combined with the energy conducted into the barrel from the barrel heaters, raises the barrel surface above the melting or softening point of the polymer. As the barrel temperature reaches the melting point of the polymer, a thin film of polymer melt forms on the barrel. As the barrel moves relative to the solid, the energy of the motor is dissipated in the melt film and the energy is conducted into the solid melting of the polymer. As the material moves forward, the amount of solid material at each location will reduce as a result of melting. When all solid polymer has disappeared, the end of the plasticating zone has been reached and the melt conveying zone starts.

3. Metering section or melt conveying section of the screw: At the end of the melting section the solid should be completely converted to a melt and the metering section creates a circulating flow of melt by the action of scraping the melt from the barrel and forcing it down to the bottom of the screw flight. The melt is conveyed by two mechanisms in the metering section, drag flow, and pressure driven flow. The balance of the two flows determines the final output of the metering section. The pressure flow is controlled by the pressure difference from the inlet of the metering section and the die restriction at the end of the extruder. In the melt conveying zone, the polymer melt is simply pumped to the die.

As the polymer flows through the die, it adopts the shape of the flow channel of the die. Thus, as the polymer leaves the die, its shape will more or less correspond to the cross sectional shape of the final portion of the die flow channel. Since the die exerts a resistance to flow, a pressure is required to force the material through the die. This is generally referred to as the die head pressure. The die head pressure is determined by the shape of the die (particularly the flow channel), the temperature of the polymer melt, the flow rate through the die, and the rheological properties of the polymer melt. The extruder simply has to generate sufficient pressure to force the material through the die. Mixing is another critical extruder function even when processing only one virgin polymer stream. The two types of mixing occurring in the extruder are:

1. The Distributive Mixing: Distributive mixing is a low shear process accomplished by repeatedly changing the flow directions by breaking the molten polymer into channels and recombining the melt. Distributive mixing is used with fibers, reinforcing fillers, shear sensitive materials, and to provide uniformity of melt temperature. This phenomenon distributes particles throughout the melt.

2. The Dispersive Mixing: Dispersive mixing is a high shear stress process where molten polymer is forced through very small openings generating significant

shear heat. Dispersive mixing is used in alloying different plastics, pigment dispersion and mixing nonreinforcing fillers and additives, such as flame retardants, impact modifiers, and lubricants. This phenomenon breaks up agglomerates or large particles and disperses them evenly throughout the melt.

The degree of mixing [18] is determined by the residence time and the shear rate the fluid is exposed in the mixing section. The type of mixing section to add to the extruder screw depends on the polymer being processed and type of mixing required. Since polymer mixing flows are laminar, the number of changes in the flow direction determines the degree of distributive mixing. Distributive mixing sections divide the flow into a number of channels, recombine the flow, break the flow, and so on, and improve temperature homogeneity. For the energy transfer screws, distributive mixing is purposely increased in the screw design by flight interchanges and the absolute need for a mixer for thermal homogenization is reduced. Mixers are often added to add a high shear section to a screw for the purpose of improving particulate dispersion or breaking down high molecular weight gels. However, the incorporation of a distributive mixer will increase the discharge temperature from the screw.

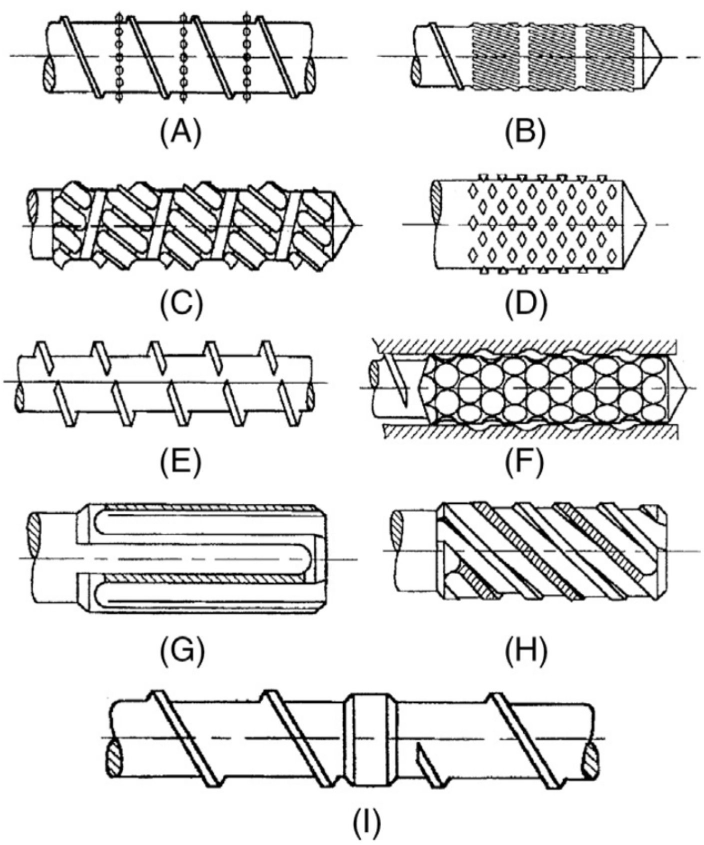

Figure 1.2: Some of the various distributive and dispersive mixer designs present into the polymer processing industry (from [18] pag. 235).

As a result, many modifications have been made to the standard extruder screw, in an effort to improve the mixing capacity. The number of mixing elements that have been used on extruder screws is very large and a number of them is shown in Figure 1.2.

1.4 Baseline model for the single screw extruder

In a single screw extruder the fluid particles move in a helical path through the helical channel between the flights of the screw when the screw is rotating and the barrel is stationary. For the purposes of mathematical modeling, this complicated flow configuration is typically approximated by conceptually unwinding the helical screw channel. As a result, the problem to be considered reduces to a flow in a straight rectangular channel covered by a diagonally moving plate (the barrel). In this section, we discuss the design of a melt extruder and derive the appropriate mathematical model [3]. In Figure 1.3 the geometry of a square pitched and single flighted screw is shown according to this simplification.

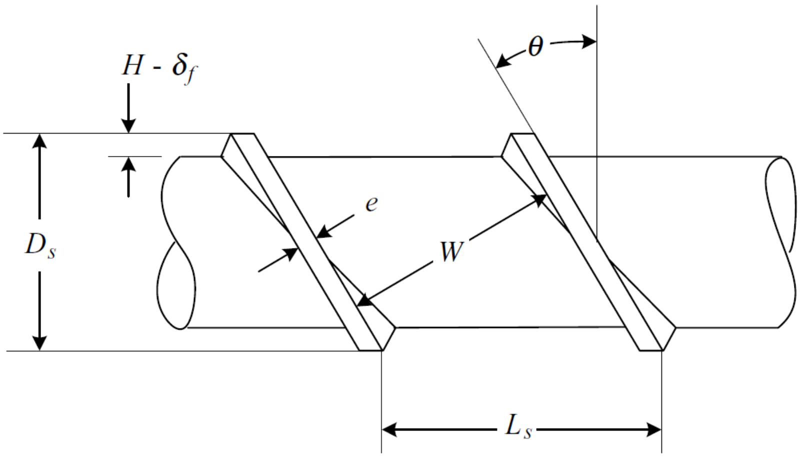

Figure 1.3: Geometry of a square pitched and single flighted screw (from reference [3] pag. 248)

Between the tip of the flight of the screw and the inner surface of the barrel D_b (diameter of the external barrel), there is a small radial clearance δ_f (gap) of the order of 0,1 – 0,3% of D_b. Polymer melt fills this gap and acts as a lubricant, preventing metal to metal contact. The diameter of the screw at the tip of the flights is $D_s = D_b - 2\delta_f$. The axial distance of one full turn of the flight is called the lead L_s. Most screws of SSEs are single flighted, with $L_s = D_s$, referred to as square pitched screws. The radial distance between the root of the screw and the barrel surface is the channel depth H. The main design variable of screws is the channel depth profile that is $H(z)$, where z is the helical, down-channel direction, namely, the direction of net flow of the material. The angle generated between the flight and the plane normal to the axis is called the helix angle θ, which, as is evident from Figure 1.4 , is related to lead and diameter:

$$\tan\theta = \frac{L_s}{\pi D} \tag{1.1}$$

The value of the helix angle is therefore a function of the diameter. At the tip of the flight it is smaller than at the root of the screw.

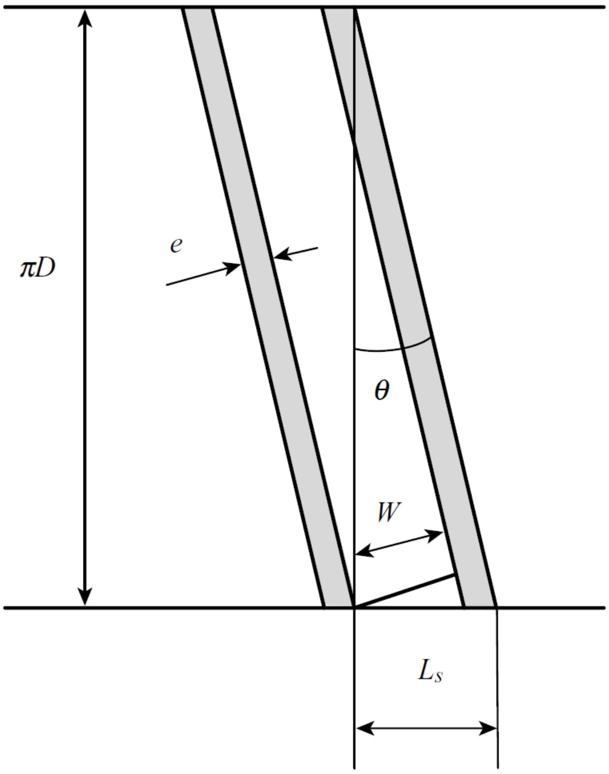

Figure 1.4: Geometry of an unwound channel (from reference [3] pag. 249)

A square pitched screw, neglecting the flight clearance, has a helix angle of 17.65° ($\tan\theta = 1/\pi$) at the flight tip. The width of the channel W is the perpendicular distance between the flights, and as shown in Figure 1.4, is:

$$W = L_s \cos\theta - e \tag{1.2}$$

where e is the flight width. Clearly, since θ is a function of radial distance, so is W. Finally, the helical distance along the channel z is related to the axial distance l:

$$z = \frac{l}{\sin\theta} \tag{1.3}$$

The mathematical model of isothermal flow of a Newtonian fluid in shallow screw channels results in a simple design equation, which gives excellent insight into the flow mechanism and it is very useful for first order calculations. This model serves as the classic pumping model for single screw extrusion. We commence its development by reversing the conceptual synthesis process. The space between a tightly fitting screw and the barrel is a helical channel. We unwind the channel from the screw and lay it on a flat surface. The result is a shallow rectangular straight channel, as in Figure 1.5.

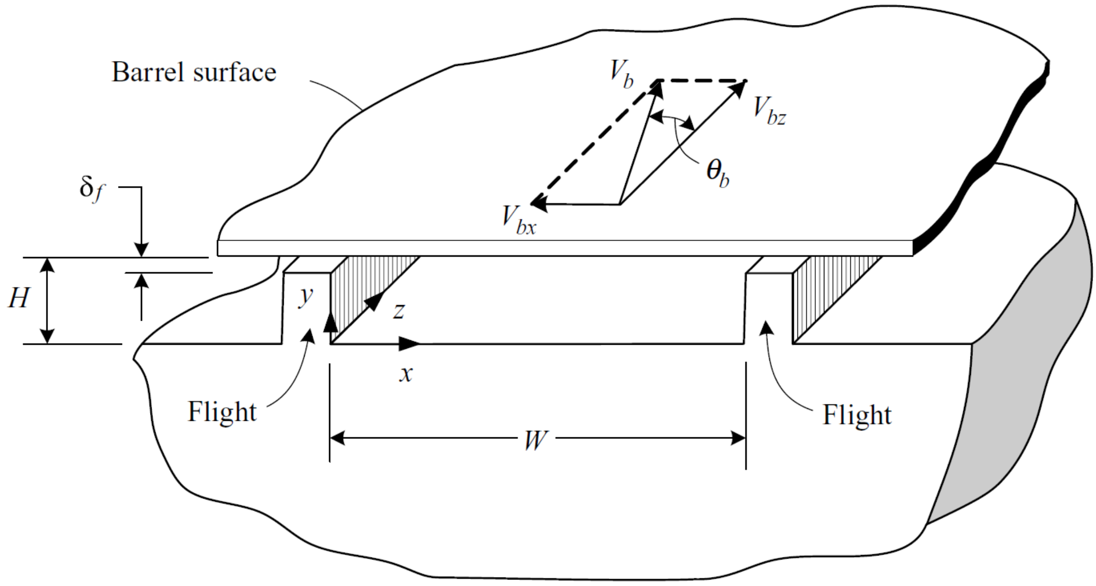

Figure 1.5: Geometry of the unwound rectangular channel (from reference [3] pag. 250)

The barrel surface becomes a flat plate covering the channel and moving at constant velocity of V_b at an angle θ_b to the down channel direction:

$$V_b = \pi N D_b \tag{1.4}$$

where N is the frequency of rotation. The surface velocity of the barrel can be decomposed into down channel and cross channel components, given, respectively, by:

$$V_{bz} = V_b \cos\theta_b \tag{1.5}$$

and

$$V_{bx} = V_b \sin\theta_b \tag{1.6}$$

The former drags the polymer melt toward the exit, whereas the latter induces cross-channel mixing. The simplifying assumptions for solving this flow problem are the flow to be an incompressible steady, isothermal, fully developed flow of a Newtonian fluid. The three components of the Navier Stokes equation in the rectangular coordinates defined in Figure 1.5 reduce to:

$$\rho\big(v_x\frac{\partial v_x}{\partial x} + v_y\frac{\partial v_x}{\partial y}\big) = -\frac{\partial P}{\partial x} + \mu\big(\frac{\partial^2 v_x}{\partial x^2} + \frac{\partial^2 v_x}{\partial y^2}\big) \tag{1.7}$$

$$\rho\big(v_x\frac{\partial v_y}{\partial x} + v_y\frac{\partial v_y}{\partial y}\big) = -\frac{\partial P}{\partial y} + \mu\big(\frac{\partial^2 v_y}{\partial x^2} + \frac{\partial^2 v_y}{\partial y^2}\big) \tag{1.8}$$

$$\rho\big(v_x\frac{\partial v_z}{\partial x} + v_y\frac{\partial v_z}{\partial y}\big) = -\frac{\partial P}{\partial z} + \mu\big(\frac{\partial^2 v_z}{\partial x^2} + \frac{\partial^2 v_z}{\partial y^2}\big) \tag{1.9}$$

In solving the Navier-Stokes equation it is convenient to neglect the effect of the flight clearance. As small as the clearance is, polymer melt is being dragged across the clearance by the barrel surface and the pressure drop may pump melt across the flight width. This creates a continuous leakage flow from downstream locations to (one turn back) upstream locations, reducing net flow rate. It is very difficult to accurately evaluate the effect of leakage flow across the flight in a real situation with significant non Newtonian and nonisothermal effects included. However, for the isothermal Newtonian model this semplification allows the analytical solution of the Navier-Stokes equation. The method is discussed in depth in reference [3], chapter 6, and leads to a design equation:

$$Q = \frac{V_{bz}W\big(H-\delta_f\big)}{2}F_d + \frac{WH^3}{12\mu}\big(-\frac{\partial P}{\partial z}\big)F_p\big(1+f_L\big) \tag{1.10}$$

where δ_f is the radial flight clearance (gap) and F_d and F_p are shape factors for drag and pressure flow, respectively. They assume values that are smaller than 1 and represent the restricting effect of the flight on flow between infinite parallel plates. They are given by:

$$F_d = \frac{16W}{\pi^3 H}\sum_{i=1,3,5}^{\infty}\frac{1}{i^3}\tanh\big(\frac{i\pi H}{2W}\big) \tag{1.11}$$

$$F_p = 1 - \frac{192H}{\pi^5 W}\sum_{i=1,3,5}^{\infty}\frac{1}{i^5}\tanh\big(\frac{i\pi W}{H}\big) \tag{1.12}$$

In addition in equation 2.10 the term f_L is given by the following expression:

$$f_L = \big(\frac{\delta_f}{H}\big)^3\frac{e}{W}\frac{\mu}{\mu_f} + \frac{\big(1+\frac{e}{W}\big)\Big[\frac{1+e/W}{\tan^2\theta} + \frac{6\mu V_{bz}(H-\delta_f)}{H^3(\partial P/\partial z)}\Big]}{1+\frac{\mu}{\mu_f}\big(\frac{H}{\delta_f}\big)^3\frac{e}{W}} \tag{1.13}$$

where μ_f is the viscosity in the flight clearance and μ is the viscosity in the channel. This is an attempt to approximately account for non Newtonian effects by evaluating the viscosity at the prevailing shear rates in the clearance. For Newtonian fluids the two are equal. Equation 1.13 suggests that drag flow is always reduced by the flight clearance by a factor of $(1-\delta/H)$. The effect of pressure flow is more complicated. In the special case of pure drag flow $\big(\partial P/\partial z = 0\big)$, the cross-channel pressure gradient creates higher pressure at the pushing flight than one turn back at the trailing flight, causing pressure leakage backflow across the flight. This leakage flow increases if pressure rises in the down channel direction, and decreases if pressure drops in the down channel direction over that one turn segment.

We carried out the analysis for isothermal flow of a Newtonian fluid, reaching a model (Equation 1.10) that is satisfactory for gaining a deeper insight into the pressurization and flow mechanisms in the screw extruder, and also for first-order approximations of the pumping performance of screw extruders. Now it is necessary to consider the entire system constituted by the screw plus its barrel. The screw is placed within a barrel of diameter $D_b = D_s + 2\delta_f$ where δ_f is the radial flight clearance. This is reported schematically in Figure 1.6.

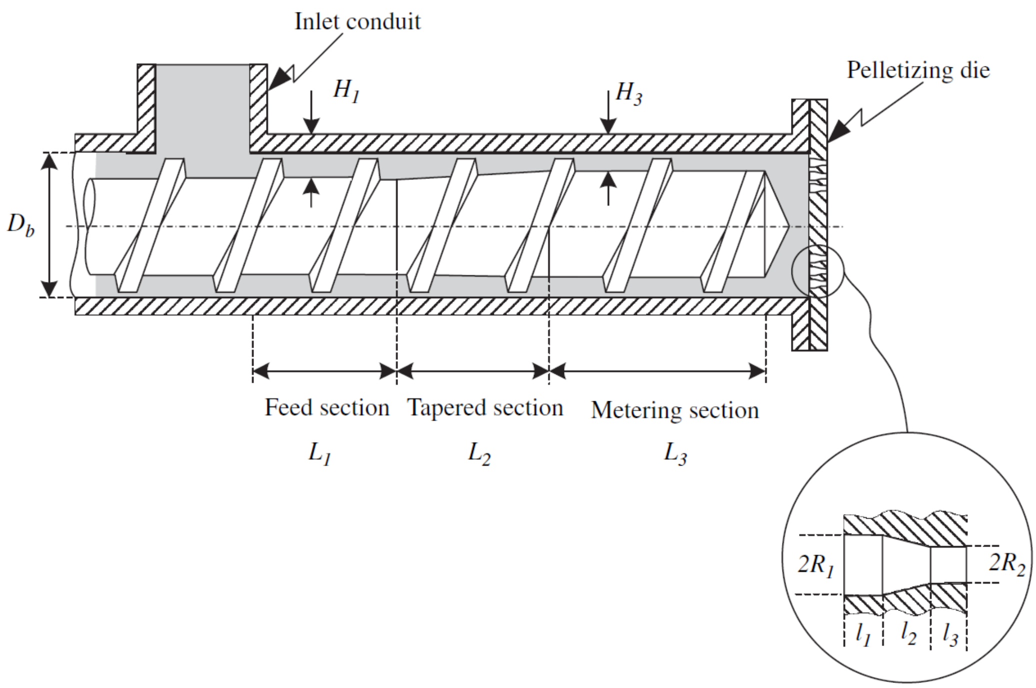

Figure 1.6: Schematic view of a melt extruder and the instrument is equipped with a feed port and a pelletizing plate (from reference [3] pag. 449)

The discussion that follows is valid for any melt extruder equipped with any kind of die, and for the melt region in a plasticating extruder as well. The system consists of three subsystems: the feed port, the screw, and the pelletizing plate, which are connected in series. Therefore, for steady state operation with atmospheric inlet and outlet conditions, the mass flow rate in each subsystem G_i is constant:

$$G_i = G_0 \tag{1.14}$$

where G_0 is the throughput, and the sum of pressure changes over the entire process is zero:

$$\Delta P_i = 0 \tag{1.15}$$

which implies that the pressure rise in the extruder equals the pressure drop over the pelletizing plate. In designing a pelletizing system, therefore, we first of all need to relate flow rate to pressure change over each subsystem. The inlet flow to the extruder is simple gravitational flow through (generally) a tubular conduit. In such slow flows, the shear rate range is very low and the isothermal Newtonian assumption is valid. For a vertical tubular entrance, the flow rate is given by the Haagen–Poiseuille law:

$$Q = \frac{\pi(P_0 - P_L)R^4}{8\mu L_0} \tag{1.16}$$

where $P_z = P_0 - \rho g z$, z is the downward distance in the inlet conduit of height L_0. Therefore, for a melt column of height L_0, $P_0 - P_L = \rho g L_0$ and:

$$Q = \frac{\pi \rho g R^4}{8\mu} \tag{1.17}$$

Drag-induced pressurization in shallow screw channels was discussed previously and the flow rate was given in Equation 1.10 and Equation 1.13. The former can be rewritten as:

$$Q_s = \frac{1}{2}\pi N D_b \cos\theta_b W(H-\delta_f)F_d - \frac{WH^3}{12\mu}\frac{\Delta P_s}{L}\sin\overline{\theta}(1+f_L)F_p \tag{1.18}$$

where:

- Q_s = volumic flow rate in the extruder
- N = frequency of rotation
- L = axial Length of the screw
- D_b = diameter of the barrel calculated as $D_b = D_s + 2\delta_f$
- θ_b = angle to the down channel direction
- W = perpendicular distance between the flights calculated with Equation 1.2
- H = radial distance between the root of the screw and the barrel surface (Channel depth)
- δ_f = radial flight clearance (gap)
- F_d = shape Factor for drag flow calculated with Equation 1.11
- μ = viscosity in the channel
- ΔP_s = pressure rise over the screw from inlet to outlet
- L = axial length of the screw
- f_L = calculated with Equation 1.13
- F_p = shape Factor for pressure flow calculated with Equation 1.12

Note that in Equation 1.18 we use an average helix angle to convert helical length to axial length; whereas, for the barrel velocity, we use the helix angle at the barrel inner surface. Equation 1.18 can be represented by plotting the flow rate Q_s versus the pressure rise ΔP_s. Such plots are called screw characteristics where the intersection with the ordinate gives the drag flow rate value and that with the abscissa, the maximum pressure at closed discharge.

2. Methods

The total work made to realize a realistic model of the single screw extruder was subdivided into four main stages which are reported in the following flux scheme (Figure 2.1).

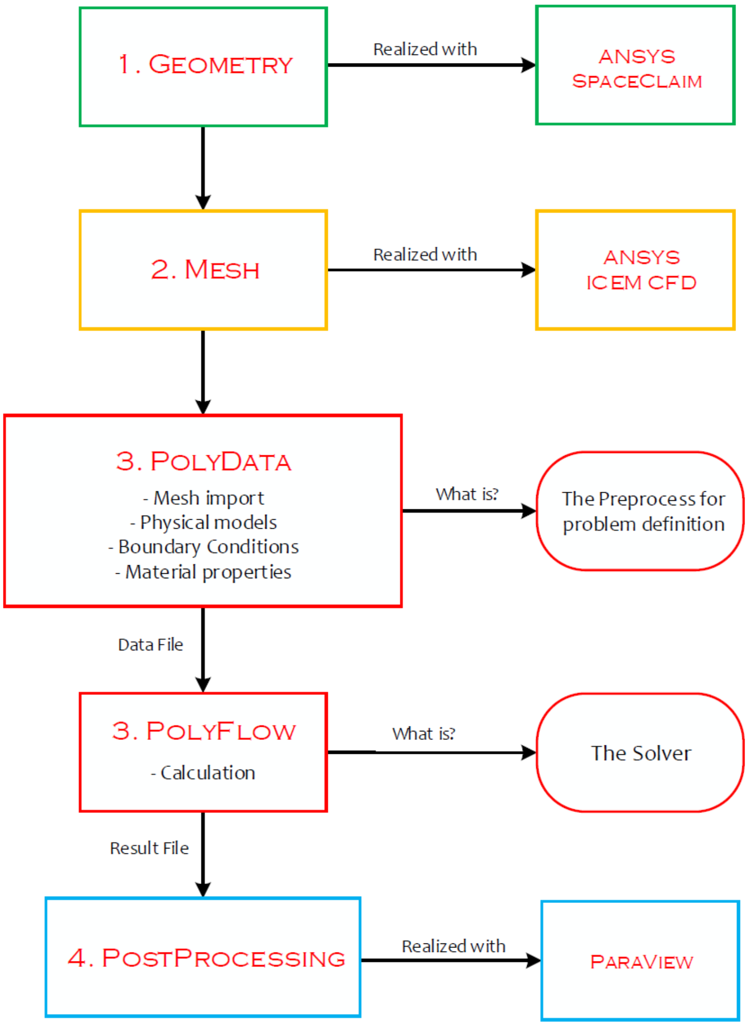

Figure 2.1: Flux scheme of the total work subdivision.

1. Geometry: The first step was the realization of the prescribed geometry received from the Continental AG and it was realized with ANSYS SpaceClaim. The model realized is a 3D model which represents a realistic extruder present in the Continental AG R & D laboratories.

2. Mesh: The second step was the creation of the mesh and it was realized using the software ANSYS ICEM CFD. After the creation of the mesh four boundary surfaces were created (Inlet, Outlet, Barrel and Screw).

3. Simulations: The software adopted for the simulations was ANSYS Polyflow. This program allows us to solve the transport and energy equations adopting the resolution tecnique called FEM (Finite Element Method). More precisely ANSYS Polydata is the preprocessor for the problem definition (where all the input informations are introduced on screen) and ANSYS Polyflow is the solver. To run the simulation both ANSYS Polydata and ANSYS Polyflow were used.

4. PostProcessing: The final step was the analysis of the simulation results and it was done adopting a software called ParaView. It is an open-source, multi-platform scientific data analysis and visualization tool that enables analysis and visualization of extremely large datasets. By adopting this software it was possible to obtain the contour plots of the main physical fields and the high resolution pictures of the 3D model realized.

2.1 Geometry

Two 3D geometries, characterized by the following parameters, were created with ANSYS SpaceClaim:

- L = Axial length of the screw = 90 cm.
- δ_f = Radial flight clearance (gap) = 1 mm.
- D_s = Diameter of the screw = 90 mm.
- D_b = Diameter of the barrel calculated as $D_b = D_s + 2\delta_f = 92$ mm.

More precisely the main information relative to the 3D geometries created are reported as follows:

1. *Nominal screw geometry*: This geometry is the requested one from the Continental AG. The *Nominal screw geometry* is not a typical single screw extruder configuration because there are different empty spaces which interrupt the flight of the screw.

2. *Full screw geometry*: To understand if the interruptions of the flight have some influences on the behaviour of the melt fluid, a second geometry was realized to obtain a comparison with the *Nominal screw geometry.* The second geometry is characterized by a full flight of the screw without empty spaces and for this reason it is called the *Full screw geometry.*

To complete the extruder geometries, a cylindrical barrel containing the screw was introduced. The barrel was designed such that, as introduced in the initial parameters, the minimum distance between the screw and the barrel wall (radial flight clearance or gap) was equal to 1 mm. The barrel is completely smooth and has no internal pins.

In Figure 2.2 and in Figure 2.3 the *Nominal screw geometry* without and with the barrel, respectively, is illustrated.

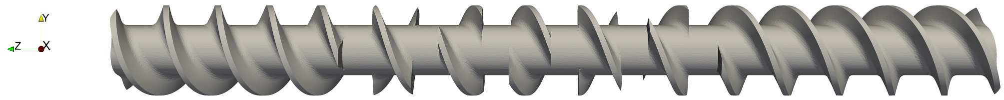

Figure 2.2: 3D representation of the *Nominal screw geometry*.

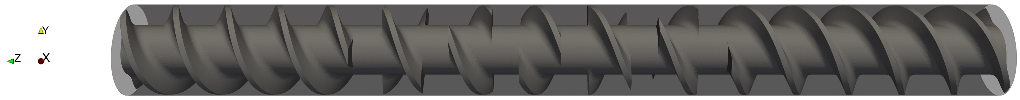

Figure 2.3: 3D representation of the *Nominal screw geometry* sorrounded by the barrel.

Similarly Figure 2.4 and Figure 2.5 illustrate the *Full screw geometry*.

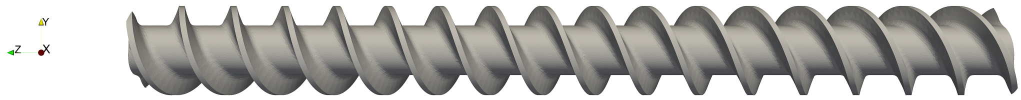

Figure 2.4: 3D representation of the *Full screw geometry*.

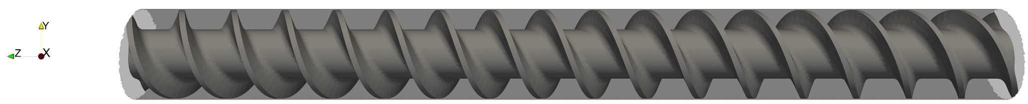

Figure 2.5: 3D representation of the *Full screw geometry* sorrounded by the barrel.

The last passage made on ANSYS SpaceClaim was the extrapolation of the volume of the fluid. This volume is the one present between the external surface of the screw and the internal wall of the barrel and this is the volume which specifically was meshed. Further details about the procedure used to build the two geometries is reported in Appendix A.

2.2 Mesh

At this point the generation of the mesh was the next step. The detailed step by step procedure (analysing the inputs introduced into the software) is reported in Appendix B. The software adopted is ANSYS ICEM CFD v19.0 [19]. This software provides advanced geometry acquisition, mesh generation, mesh diagnostic and repair tools. Maintaining a close relationship with the geometry during the mesh generation, ANSYS ICEM CFD is designed for use in engineering applications such as computational fluid dynamics and structural analysis. In ANSYS ICEM CFD, it is possible to introduce the input geometry in almost any format (from a commercial CAD design package, third part universal database, scan data or point data). The mesh generation tool of this software offers the capability to parametrically compute meshes from geometry in numerous formats:

- Unstructured hexahedral.
- Unstructured tetrahedral.
- Hybrid meshes comprising hexahedral, tetrahedral, pyramidal and/or prismatic elements.
- Wedge based and triangular surface meshes.

More precisely the main properties of the different meshing methods are reported as follows:

- Tetra: Tetra mesher is suitable for complex geometries offering a rapid model setup (fast algorithm) and the surface mesh is not necessary. In fact the tetra mesher can use different meshing algorithms to fill the volume with tetrahedral elements and to generate a surface mesh on the objects. For this reason as input we need just to select the geometry that need to be meshed and the software automatically generates the mesh. The tetrahedral mesh can be merged into another tetra, hexa, or hybrid mesh and then can be smoothed. On the contrary the tetra meshing is not efficient for capturing shear or boundary layer physics creates an unstructured mesh of tetrahedral cells. Due to the tetra limits it is possible to avoid this kind of problem adopting inflation elements (prism or hexa).

- Prism (wedge based): Prism mesher generates hybrid meshes consisting of layers of prism elements near the boundary surfaces and tetrahedral elements in the interior for better modeling of near wall physics of the flow field. When compared to pure tetrahedral meshes, this results in smaller analysis models, better convergence of the solution, and better analysis results. Calculations are done between nodes or elements, and a prism mesh gives you more elements perpendicular to the surface. This is an efficient way to achieve better resolution (more calculations per unit distance) of the solution normal to the surface, without increasing the number of elements along the surface. This gives us a quicker and more accurate solution compared to the one that can achieved with a very fine tetra mesh.

- Hexa: Hexa mesher is a semi automated meshing module that allows rapid generation of multi block structured or unstructured hexahedral volume meshes. ICEM CFD Hexa represents a new approach to mesh generation where the operations most often performed by experts are automated and made available at the touch of a button. Blocks can be built and interactively adjusted to the underlying CAD geometry.

- Hybrid meshes: Tetra and Hexa meshes can be united (merged) at a common interface in which a layer of pyramids is automatically created to make the two mesh types conformal. These meshes are suitable for models where it is preferred to have a structured hexa mesh in one part and is easier to create an unstructured tetra mesh in another more complex part.

In this work a hybrid mesh characterized by tetrahedral and wedged based elements was created. In fact two main zones in the fluid domain can be defined:

1. The gap between the screw and the barrel: This is a critical zone due to its small thickness and when the tetrahedral mesh type is applied on the total model, the number of nodes (where the solver solve the transport and energy equations) generated in this zone is low. For this reason the results obtained could be affected by errors or inaccuracy. To obtain a better analysis in this critical zones it was necessary to introduce an ordered and more refined mesh (wedge based mesh).

2. The bulk of the fluid: This zone did not need the accuracy of the previous zone and for this reason was sufficient to compute a tetrahedral mesh type.

In Figure 2.6 both the zones and their meshes are reported.

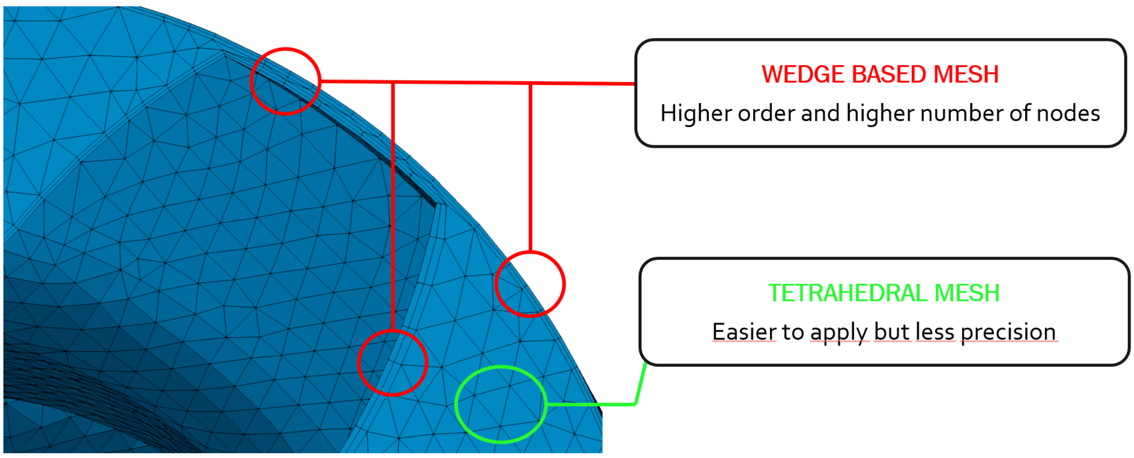

Figure 2.6: Details of the main zones with their meshes.

It can be seen that by using this approach a larger number of mesh elements is obtained in the gap and in the region close to the screw compared to the zone of the bulk of the fluid. A 3D representation of the total mesh created for the volume of the fluid is showed in Figure 2.7.

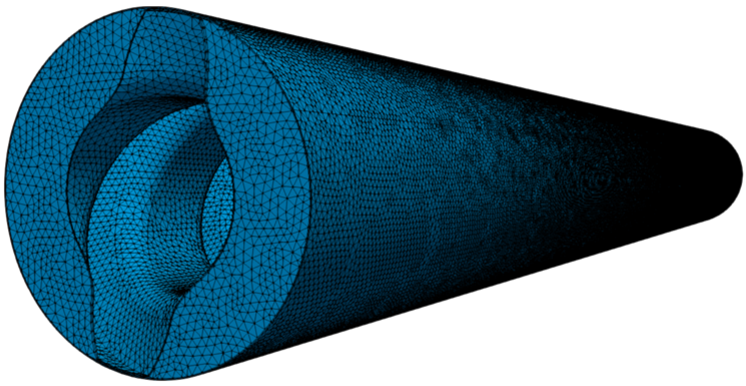

Figure 2.7: 3D representation of the total mesh generated for the volume of the fluid.

In Figure 2.8 a detail of the generated mesh is illustrated by a node based representation.

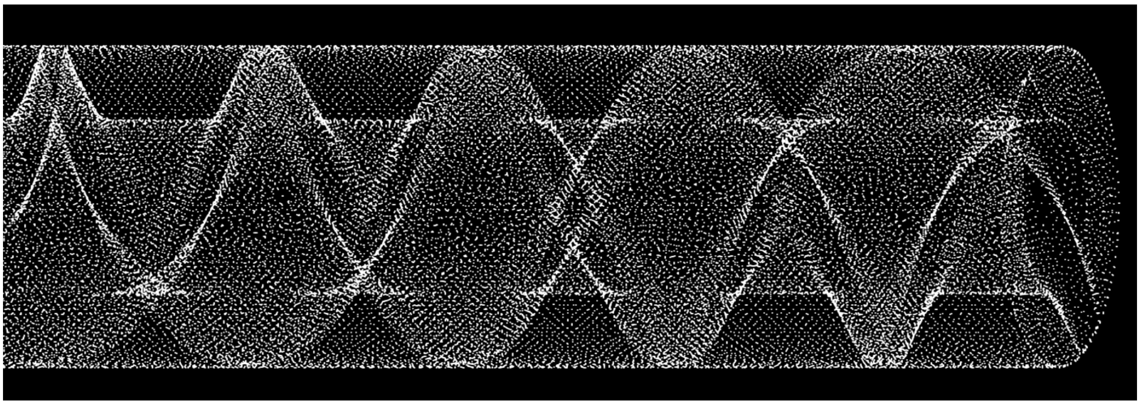

Figure 2.8: Volume discretization by a node based representation.

It can be seen that in the critical zones (i.e. the gap between the screw and the barrel) the finest mesh resolution was obtained. For the *Nominal screw geometry* the following information about the generated mesh was reported by the code:

$$\text{Number of bricks} = 2245946$$

$$\text{Number of faces} = 4863229$$

$$\text{Number of nodes} = 601420$$

For the *Full screw geometry* the values become as follows:

$$\text{Number of bricks} = 2227608$$

$$\text{Number of faces} = 4841799$$

$$\text{Number of nodes} = 607557$$

The number of bricks in the *Nominal screw geometry* is higher compared to the other geometry because the empty spaces which interrupt the flight of the screw are responsable of an higher volume of fluid. On the contrary the number of nodes is higher in the *Full screw geometry* because, as illustrated previously, in the regions near the screw the number of nodes is the highest. After the creation of the mesh for the two geometries, it was necessary to define the four boundary sections. "Inlet" and "Screw" boundary sections are showed in Figure 2.9.

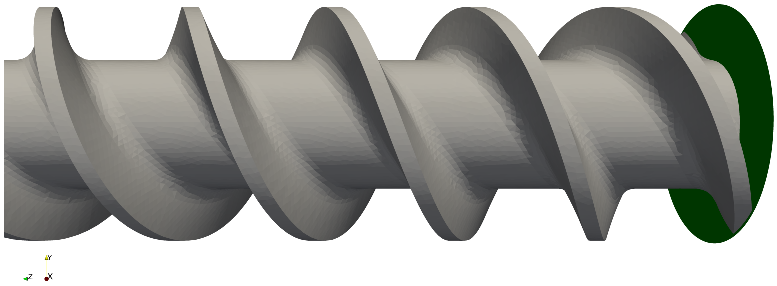

Figure 2.9: Inlet (green) and Screw (grey) boundary sections.

"Outlet" and "Barrel" boundary sections are instead showed in Figure 2.10.

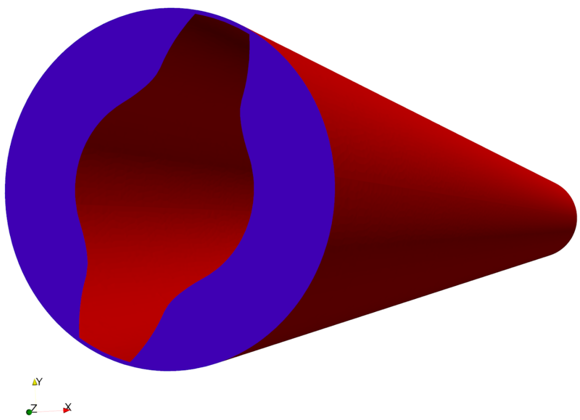

Figure 2.10: Outlet (blue) and Barrel (red) boundary sections.

Once the meshes were created and the boundary sections were defined, an output file was generated and the simulations could be set up.

2.3 Simulations

To perform the simulations, ANSYS Polyflow v19.0 [20] was the software adopted. This software is a Finite Element computational fluid dynamics (CFD) code designed primarily for simulating applications where rheology plays an important role. More precisely it is used primarily to solve flow problems in polymer and rubber processing, food rheology, glasswork furnaces, and many other rheological applications. The calculation of such flows is based on non Newtonian fluid mechanics, characterized by a wide variety of fluid models and strong nonlinearities. In ANSYS Polyflow it is possibile to use the approach of Generalized Newtonian Flow [21]: this category of flows includes both Newtonian and inelastic non Newtonian flows. The flows can be isothermal or nonisothermal, 2D or 3D, steady-state or time-dependent. ANSYS Polyflow was perfectly suited for our application because it offers the possibility to perform a number of complex simulations such as coextrusion of several fluids or three-dimensional extrusion. After determining the most important features of the problem we wanted to solve, the following basic procedural steps were made:

1. ANSYS PolyData was started.
2. The mesh file was introduced into ANSYS PolyData.
3. The physical models were defined and the steady state simulation was selected.
4. The material properties were specified.
5. The boundary conditions were specified.
6. The output format for the results was specified (Ensight format for the Paraview Postprocessor).
7. The data file was saved and ANSYS PolyData was closed.
8. The solution was calculated by ANSYS Polyflow, using the data file as input.
9. A result file was generated.

2.3.1 Finite Element Method

In the last few decades, revolution in the computer technology has led to development of numerous computational techniques for solving many engineering problems [22]. As mathematical modelling became an integral part of the analysis of engineering problems, a variety of numerical methods have been developed. Out of the available numerical techniques, the Finite Element Method (FEM) is one of the most flexible and versatile method for solving engineering problems. The description of the laws of physics for space- and time-dependent problems are usually expressed in terms of partial differential equations (PDEs). For the vast majority of geometries and problems, these PDEs cannot be solved with analytical methods. The unknown state variables are solved at a discrete number of points in the problem domain to obtain approximate solutions. The process of dividing the problem domain into an equivalent system of smaller domains or units and selecting a discrete number of points is called discretization. Once a problem domain is discretized, the solution can be obtained for each of the smaller domains or units considered. Finally, such domainwise solutions can be combined together to obtain solution for the entire domain. The basic idea of FEM is developed from the above principle. Discrete points considered in the domain are called Nodes and the smaller considered domains or units are called Elements. Elements and Nodes together constitute the mesh. FEM offers a way to solve wide variety of complex continuum problems by sub-dividing them into a series of simpler interrelated problems.

Essentially, FEM provides a consistent technique for modelling the whole system as assemblages of discrete parts or finite elements. In many engineering problems, the field variable (such as pressure, velocity and temperature) possesses infinitely many values because it is a continuous function of the coordinates in the solution domain. Hence, the problem becomes one with an infinite number of unknowns. The discretization procedure reduces the problem to one with a finite number of unknowns by dividing the solution domain into elements. Then the unknown field variable is expressed in terms of assumed approximating functions within each element. Approximating functions (or interpolating functions) are defined in terms of values of the field variables at specified nodes or nodal points. Nodes usually lie on the element boundaries (boundary nodes) where adjacent elements are considered to be connected inside the element as interior nodes. The behaviour of the concerned field variable within the element is defined by the nodal values of the field variable and the interpolation function for the element. The nodal values of the field variable become the new unknowns for the finite element representation of the problem. Once the nodal unknowns are obtained, the interpolation functions define the field variable throughout the assemblage of elements of the problem. The nature of the solution and the degree of accuracy depend on the size and number of elements and the kind of interpolation function used. The interpolation functions are chosen such that the field variable or its derivatives are continuous across adjoining element boundaries.

FEM can be applied to almost all branches of engineering but it is important to know that the fact this method can be used to solve a particular problem does not mean that it is the most ideal solution technique. Each method has its own merits or demerits. Here, the merits and demerits of FEM are discussed. Compared to other numerical methods (i.e. Finite Volume Method) some of the merits of this kind of technique are:

- Modelling of complex geometries and irregular shapes are easier as varieties of finite elements are available for the discretization of the domain.
- The boundary conditions can be easily incorporated into the FEM technique.
- Problems with heterogeneity, anisotropy, nonlinearity and time dependancy can be easily dealt with.
- The systematic generality of FEM procedure makes it a powerful and versatile tool for a wide range of problems.
- In FEM it is relatively easy to control the accuracy by refining the mesh or using higher order elements.
- Availability of large number of computer codes and literature makes FEM a versatile and powerful numerical method.
- FEM can be easily coupled with CADs programs in various streams of engineering.
- A FEM model can be developed at different levels and it is possible to interpret the method in physical terms.

Instead some demerits of the FEM are as follows:

- Closed-form expressions in terms of problem parameters are not available in the FEM. Numerical solution is obtained at one time for a specific problem case only. Hence, unlike analytical solutions, there is no advantage of flexibility and generalization.
- A large amout of data is required as input for the mesh used in term of nodal connectivity and other parameters depending on the problem.
- Generally, voluminous output data must be analysed and interpreted.
- Experience, good engineering judgment and understanding of the physical problems are required in the FEM modelling. Poor selection of element type or discretization may lead to faulty results.
- Generally, voluminous output data must be analysed and interpreted.
- Mass, momentum and energy conservation are not natively guaranteed as in a Finite Volume Method.

2.3.2 Generalized Newtonian flow: theory and equations

The flow phenomena observed with polymeric fluids cannot be predicted by the classical Navier-Stokes equations. In fact non Newtonian behaviour has many facets like the shear rate dependence of the shear viscosity, presence of normal stresses in viscometric flows, high resistance to elongational deformation and memory effects associated with the elasticity of the fluid. For this reason for a generalized Newtonian flow, ANSYS Polyflow solves the momentum equations, the incompressibility equation, and (for nonisothermal flows) the energy equation. The form of the momentum equations is:

$$-\nabla p + \nabla \cdot \mathbf{T} + \mathbf{f} = \rho \mathbf{a} \tag{2.1}$$

where:

- p = pressure
- $\mathbf{T}$ = stress tensor
- $\mathbf{f}$ = volume force
- ρ = density
- $\mathbf{a}$ = acceleration

For a generalized Newtonian fluid, ANSYS Polyflow also considers:

$$\mathbf{T} = 2\eta \mathbf{D} \tag{2.2}$$

where $\mathbf{D}$ (rate of deformation tensor) is defined as:

$$\mathbf{D} = \frac{1}{2}((\nabla \mathbf{v})^t + \nabla \mathbf{v}) \tag{2.3}$$

where $\mathbf{v}$ is the velocity and η is a function of the local shear rate $\dot{\gamma}$, defined as:

$$\dot{\gamma} = \sqrt{2tr(\mathbf{D})^2} \tag{2.4}$$

In a simple shear flow, $\dot{\gamma}$ reduces to a velocity gradient. The incompressibility equation is:

$$\nabla \cdot \mathbf{v} = 0 \tag{2.5}$$

These equations were solved to simulate the flow motion inside the system. Some simulations were run to solve only the flow field without considering the energy transport equation (isothermal system). Some others (non isothermal system) were run solving also the energy transport equation [23]:

$$\rho c_p \frac{DT}{Dt} = -\nabla \cdot \mathbf{q} + \boldsymbol{\sigma} : \mathbf{D} \tag{2.6}$$

where:

- ρ = density
- c_p = specific heat capacity
- $\frac{DT}{Dt}$ = material derivative of the temperature
- $\mathbf{q}$ = heat flux
- $\boldsymbol{\sigma}$ = Cauchy stress tensor, $-p\mathbf{I} + \mathbf{T}$
- $\mathbf{D}$ = rate of deformation tensor

In Equation 3.6 the material derivative of the temperature can be expressed as:

$$\frac{DT}{Dt} = \frac{\partial T}{\partial t} + \mathbf{v} \cdot \nabla T \tag{2.7}$$

In Equation 3.6 the heat conduction is governed by Fourier's law:

$$\mathbf{q} = -k \nabla T \tag{2.8}$$

where k is the thermal conductivity, which can be constant or temperature dependent and also c_p can be constant or temperature dependent (In this work both were considered constant). In Equation 3.6 it is also possible to notice the presence of a term, $\boldsymbol{\sigma} : \mathbf{D}$, which represents the viscous dissipation, which can be important for highly viscosity materials.

2.3.3 Shear rate dependence of viscosity

It is well known that a polymer melt is not a Newtonian fluid. Therefore to introduce the method adopted to analyse this fluid is necessary to recall some notions about the Newtonian fluids. The rheological behaviour [24] of a material is described by the relationship between the shear stress and the shear rate and first of all the shear stress is introduced. During a laminar flow, two layers move along each other and this relative displacement results in friction forces acting tangentially to the layers called shear forces (F). The Shear stress arises due to these forces, which are the pair of forces acting on opposite sides of a body with the same magnitude and opposite direction. In Figure 2.11 a representation of these forces and the effect of the shear stress is reported :

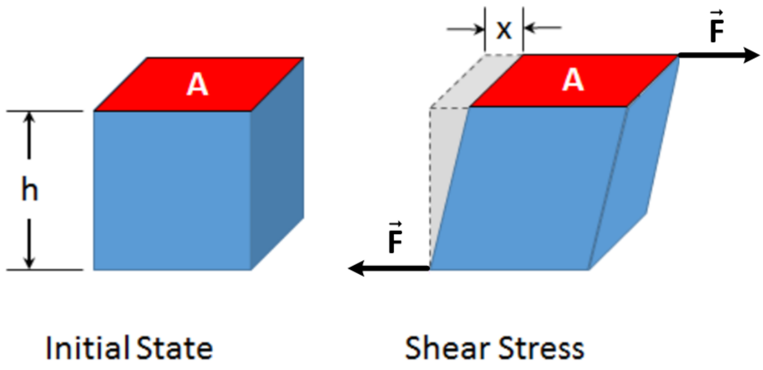

Figure 2.11: Representation of the shear forces and the shear stress.

When reported to the unit areas (A) on which they are acting, these forces result in a physical quantity of great importance in rheology, namely shear stress. This quantity is defined by the following relationship:

$$\tau = \frac{F}{A} \tag{2.9}$$

Where:

- τ = shear stress
- F = force applied
- A = area of cross section, which is parallel to the force vector

The shear stress τ is a force per unit area, and is expressed in Pascal (Pa) in the International System of units. It is a function defined at each point of the material, and varies from one layer to another. Due to symmetry, τ is usually considered constant at all points of the same layer. Now it is necessary to introduce the shear rate and we need to consider the particular case of laminar shear flow with a planar simmetry reported in Figure 2.12.

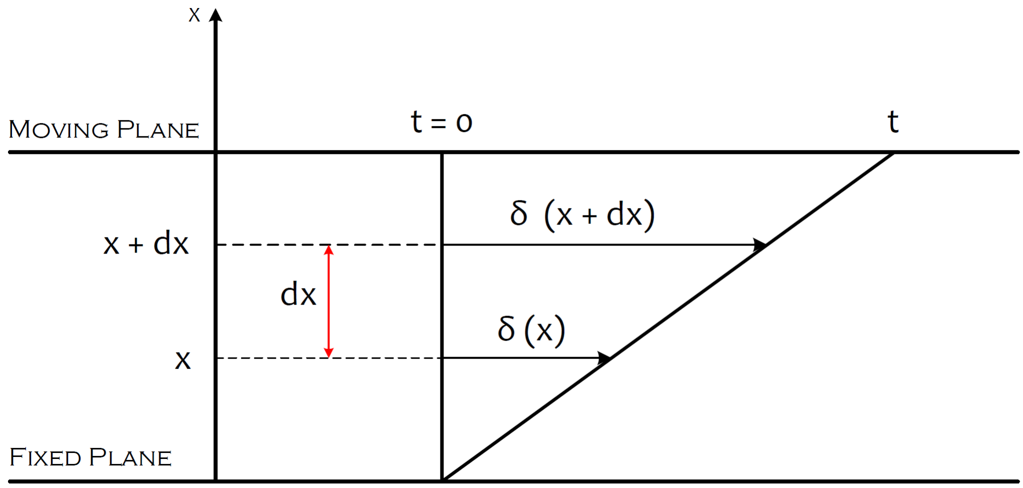

Figure 2.12: Definition of the shear rate.

In this system the material is sheared between two parallel planes, with one moving while the other is fixed to define the shear deformation. At $t = 0$, if we consider some particles, they belong to cross sections located at distances x and $x + dx$ from the fixed plane. At a later time t, the particles of the cross sections located at x and $x + dx$ have travelled the distances $\delta(x, t)$ and $\delta(x + dx, t)$, respectively, where x is the location of the particle relative to the lower (fixed) plane. The shear deformation can be defined by the following relationship:

$$\gamma(x, t) = \frac{\delta(x + dx, t) - \delta(x, t)}{dx} = \frac{d\delta(x, t)}{dx} \tag{2.10}$$

It can be noted that the shear deformation does not depend on the displacement $\delta(x, t)$ itself, but on its variation when passing from one layer to another infinitely close layer. This relates to the shear rate $\dot{\gamma}$, which is the derivative with respect to time of the shear strain γ:

$$\dot{\gamma} = \frac{d\gamma}{dt} \tag{2.11}$$

The shear rate therefore has an inverse dimension of time and is expressed in s^{-1}. Several rheological models have been proposed to describe the relationship between shear stress and shear rate. These models are identified according to the macroscopic response of the material subjected to various shear rates. The most common models are shown in Figure 2.13 and they can be subdivided into:

- Newtonian fluids.
- Pseudoplastic or shear-thinning fluids.
- Dilatant or shear-thickening fluids.
- Viscoplastic fluids.

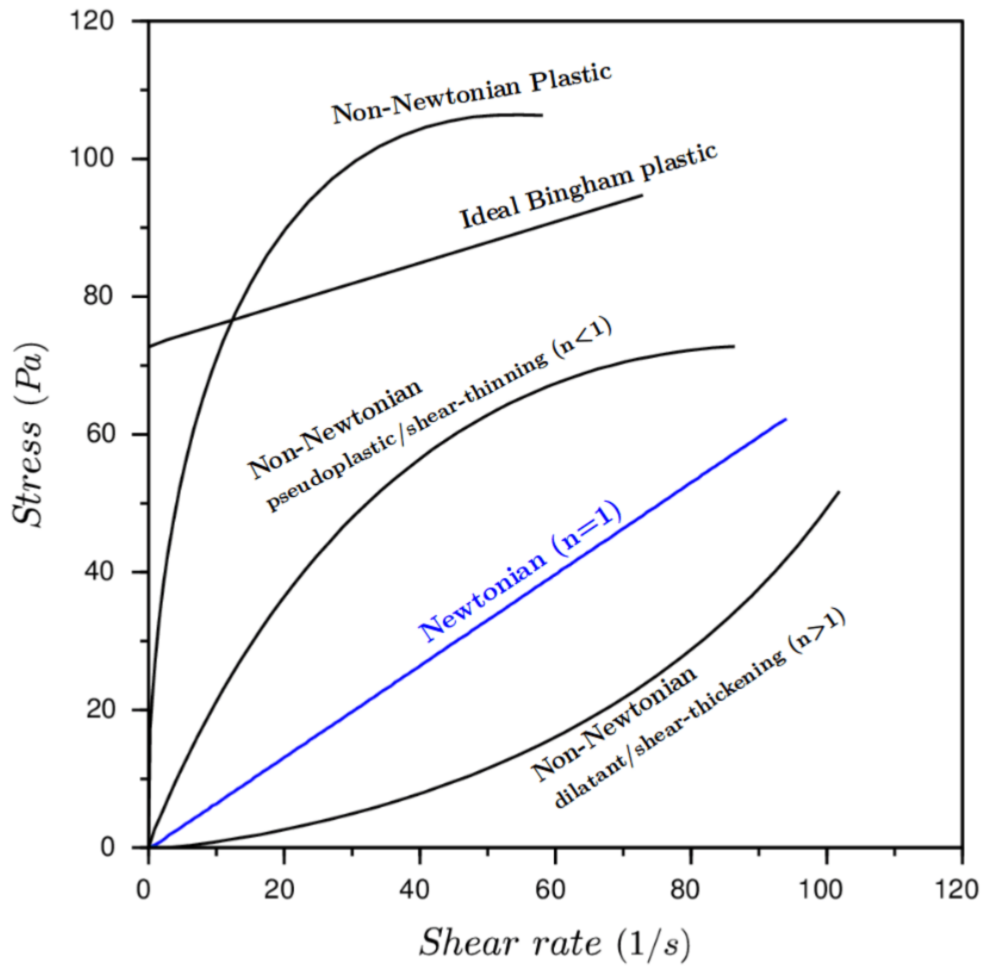

Figure 2.13: Classification of non Newtonian fluids based on the stress-shear rate plot.

- Newtonian fluids display a linear relation (displayed with the blue line in Figure 2.13) between shear stress and shear rate. The only parameter needed to describe the model is the slope of the shear stress - shear rate relationship. By definition, this slope corresponds to the dynamic viscosity η expressed in Pa $\cdot$ s. Newtonian materials are characterized by a constant viscosity, indipendent of shear rate. Newton's law of viscosity is:

$$\tau = \eta\dot{\gamma} \tag{2.12}$$

- Pseudoplastic or shear - thinning fluids are characterized by the decrease of the viscosity with the increase of the shear rate. Typical examples for pseudoplastic fluids are polymer solutions and similar solutions of high molecular weight substances. At low shear rates, these liquids will experience the formation of shear stress. The shear stress results in the reordering of the molecules in order to reduce the overall stress. This induction of a higher degree of order in the fluid reduces the shear stress and leads to the observed nonproportionality between the shear rate and the shear force.

- On the contrary in the dilatant or shear - thickening fluids the viscosity will grow with increasing shear rate. Typical examples of dilatant fluids are thick suspensions of particles in a liquid. If a shear rate is applied to these particles, they need to reorder to reduce the influence of the shear rate. By doing so, the overall shear force can be reduced. If the shear rate applied is small, the particles have enough time to reorder. However, if a high shear rate is applied, the particles do not have the required time to reorganize and a significant shear force is built up. A good example of a dilatant fluid is a suspension of corn starch in water. If such a suspension is compressed quickly by hand, the suspension will turn almost solid. If releasing the pressure, the suspension will flow freely again.

- Viscoplastic fluids do not deform when subjected to a shear stress smaller than a certain value, which is called the yield stress. In this range of applied shear stress, these materials behave as ideal rigid solids. If the shear stress in the fluid exceeds the yield stress then the fluid deforms as a (nonlinearly) viscous fluid and is typically shear thinning since the fluid structure breaks down progressively with shear. A viscoplastic fluid with a linear behaviour is then called a Bingham plastic fluid.

In ANSYS Polyflow several viscosity laws [21] are available for generalized Newtonian flows and the most important are:

1. Power Law (the adopted one for this work).
2. Bird-Carreau Law.
3. Bingham Law

Analysing in more details these models:

1. The power law for dynamic viscosity is:

$$\eta = K \cdot \dot{\gamma}^{n-1} \tag{2.13}$$

   Where:

   - K = flow consistency index
   - $\dot{\gamma}$ = shear rate
   - n = power law index, which is a property of a given material

   Based on the power - law index n:

   - If $0 < n < 1$ the fluid shows *Pseudoplastic* or *Shear-thinning* beahaviour.
   - If $n = 1$ the fluid shows *Newtonian* beahaviour.
   - If $n > 1$ the fluid shows *Dilatant* or *Shear-thickening* beahaviour.

2. The Bird - Carreau law for dynamic viscosity is:

$$\eta = \eta_\infty + (\eta_0 - \eta_\infty)(1 + \lambda^2\dot{\gamma}^2)^{\frac{n-1}{2}} \tag{2.14}$$

Where:

- η_∞ = infinite shear rate viscosity.
- η_0 = zero shear rate viscosity.
- λ = natural time (which is the inverse of the shear rate at which the fluid changes from Newtonian to power - law behaviour).

The Bird Carreau law is commonly used to describe the low shear rate behaviour of the viscosity. This model will capture the plateau zone of the viscosity curve for low shear rates better than the power law.

3. The Bingham law for dynamic viscosity is:

$$\eta = \begin{cases} \eta_0 + \frac{\tau_0}{\dot{\gamma}} & \dot{\gamma} \geqslant \dot{\gamma}_c \\ \eta_0 + \tau_0 \frac{(2 - \frac{\dot{\gamma}}{\dot{\gamma}_c})}{\dot{\gamma}_c} & \dot{\gamma} < \dot{\gamma}_c \end{cases} \tag{2.15}$$

- τ_0 = yield stress
- $\dot{\gamma}_c$ = critical shear rate

The Bingham law is commonly used to describe materials such as concrete, mud, dough, and toothpaste, for which a constant viscosity after a critical shear stress is a reasonable assumption, typically at rather low shear rates.

The experimental viscosity-shear rate data for the simulated polymer are shown in Figure 2.14.

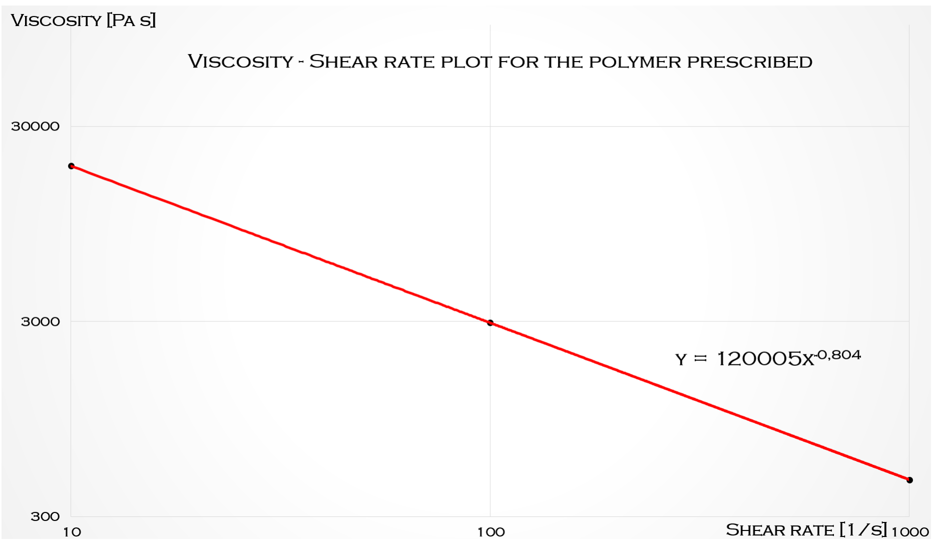

Figure 2.14: Viscosity-shear rate experimental data (black dots). The red line represents the power law fitting curve.

Interpolating with the power law the data provided, a good agreement was found for the following values of the power law parameters:

$$n = 0,1957$$

$$K = 120000 \ \mathrm{N\,s^n\,m^{-2}}$$

2.3.4 Rotating reference frame

When it is necessary to simulate flows with internal moving parts three main techniques can be adopted:

1. Mesh superposition technique
2. Sliding mesh technique
3. Rotating reference frame technique (the adopted choice made in this work)

The mesh superposition technique [25] can be employed as an efficient tool for grid generation in complex geometries. This technique is based on the subdivision of the physical domain into overlapping subdomains. In particular two meshes are generated: one is kept fixed and applied on the volume of the fluid and the other is applied on the moving parts. If the volumes of stationary and rotational components are constructed and gridded separately, so that grid cells are free to overlap, mesh quality is preserved in each of the separate domains. Subsequently, the system of flow equations is solved on each subdomain separately, and the global solution is obtained by iteratively adjusting the boundary conditions on each subdomain. The mesh superposition technique has three major advantages:

- Mesh generation is much simpler since no complex intermeshing region must be generated.
- It is possible to define a library of moving parts, and to combine them to generate new meshes for new simulations.
- The method is robust, since no remeshing algorithms are needed.

The mesh superposition technique also has several limitations:

- It can be used only for 2D planar and 3D models.
- Currently in ANSYS Polyflow can be applied only to generalized Newtonian flow.
- The detailed variation of the velocity in the neighborhood of the moving part is not well resolved.
- As the physical boundaries do not match finite-element limits, the mass conservation Equation 2.5 cannot be satisfied in every element. For this reason some limited fluid leakage can be present, reducing the accuracy of the solution.

The basic solution process of the sliding mesh technique [26] starts from a single computational mesh, which is subdivided into a moving and a static part. The moving and the static parts are separated by the sliding interface, which consists of a set of identical surface elements, accessible from both sides of the interface. In a single movement step, the mesh in the moving part slides with a predefined velocity across the mesh in the static part. After each step, the interface vertices in the moving and static parts will be re-attached according to the initially computed vertex map list. Due to the implicit approach the grid nodes will be rotated into their final position already at the beginning of each calculation time step. For the integration of the fluid flow equations, the grid nodes will remain attached in order to ensure strong implicit coupling across the interface. At the beginning of a new calculation time step, the grid movement mechanism will be repeated and the vertices at the interface will be again mapped into their final position. ANSYS Polyflow incorporates a sliding mesh technique, which can be used to to simulate transient flows with internal moving parts. The advantages of using the sliding mesh technique over the mesh superposition technique are as follows:

- The sliding mesh technique is more accurate.
- It does not make any approximation on the shape of moving part. In the mesh superposition technique instead the shape of moving part depends on the mesh discretization of the flow region.

The limitations of the sliding mesh technique are as follows:

- You can solve only the simple rotation of a moving part around a fixed axis.
- It does not allow the intermeshing of moving parts.
- in the sliding mesh technique each moving part must be surrounded by a cylinder in 3D models. These cylinders should neither overlap nor cross boundaries of the flow domain during simulation. In 2D cases, the moving parts must be surrounded by circles.
- It is available in ANSYS Polyflow only for Generalized Newtonian fluids (isothermal or nonisothermal) and heat conduction problems. It is not available for viscoelastic fluids and transport of species.

The last technique that can be adopted is the rotating reference frame technique. In analytical approaches two different ways of creating the screw-motion are used: either by rotating the screw and keeping the barrel stationary or by fixing the screw and rotating the barrel. The latter uses a rotating coordinate system and is usually preferred in theoretical approaches due to its simplified analysis. This choice was made because by keeping the reference frame on the screw and letting the barrel rotate, the shape of the flow domain does not change in time and stationary simulations are possible, provided that an opportune transformation of the system of reference is performed. For this reason transient simulations could be avoided and we could save in terms of computational time.

ANSYS Polyflow has the ability to model flows in an accelerating reference frame and in this situation the acceleration of the coordinate system is included in the equations of motion describing the flow. A common example of an accelerating reference frame is flow in rotating equipment and this is perfectly suitable for the model analyzed. Many such flows can be modeled in a coordinate system that is moving with the rotating equipment and thus experiences a constant acceleration in the radial direction. This class of rotating flows can be treated using a rigid rotation task in ANSYS Polyflow. The fluid velocities can be transformed from the stationary frame to the rotating frame using the following relation:

$$\mathbf{v_r} = \mathbf{v} - \mathbf{u_r} \tag{2.16}$$

where:

- $\mathbf{v_r}$ = relative velocity (the velocity viewed from the rotating frame)
- $\mathbf{v}$ = absolute velocity (the velocity viewed from the stationary frame)
- $\mathbf{u_r}$ = whirl velocity (the velocity due to the moving frame)

In Equation 3.16 the term $\mathbf{u_r}$ can be written as:

$$\mathbf{u_r} = \Omega \times \mathbf{x} \tag{2.17}$$

where:

- Ω = angular velocity of the rotating frame
- $\mathbf{x}$ = position vector in the rotating frame

2.3.5 Flow boundary conditions

Solving a problem in ANSYS Polyflow requires the user to define a proper set of boundary conditions [27]. The flow boundary conditions used to solve the momentum transport Equation 3.1 are illustrated in Figure 2.15.

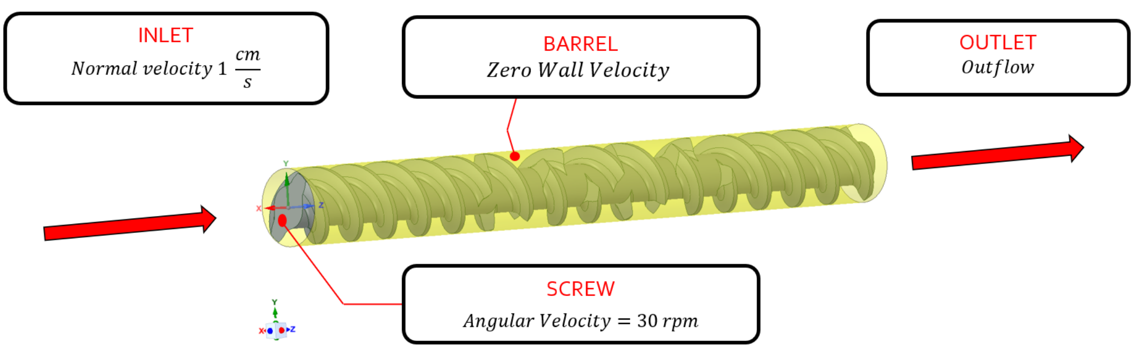

Figure 2.15: Representation of the flow boundary conditions.

- Inlet: At the "Inlet" boundary section the condition "Inflow" was imposed. This condition allows us to specify a volumetric or a mass flow rate across the boundary section. More precisely, to define the volumic flow rate, the input introduced into the simulator was the normal inlet velocity ($\frac{\mathrm{cm}}{\mathrm{s}}$) of the fluid. For the main simulation the inlet velocity was fixed to 1 $\frac{\mathrm{cm}}{\mathrm{s}}$ which correspond to a volumic flow rate of $0.37449 \cdot 10^{-4}\frac{\mathrm{m}^3}{\mathrm{s}}$.

- Barrel: At the "Barrel" boundary section the condition "Cartesin Velocity Condition (v_x, v_y, v_z)" was prescribed. When selecting this condition is necessary to specify the 1^{st} and 2^{nd} point of the axis, and the angular velocity. In this work the rotation was fixed around the z axis and we let the barrel rotate at 30 rpm. Despite we let the barrel rotate, thanks to the rotating reference frame fixed on the screw, we can see the screw rotating in the post processing. For this reason Figure 2.15 shows the screw rotating at 30 rpm.

- Screw: At the "Screw" boundary section the condition "Zero wall velocity $(v_n = v_s = 0)$" was imposed. v_n represents the normal velocity component and v_s represents the tangential velocity component (in 3D v_s is a vector with two components). This condition was imposed to the screw which is kept fixed during the simulations but resulting in motion when analysing the results.

- Outlet: At the "Outlet" boundary section the condition "Outflow" was imposed. This condition let to the simulator understand where the fluid is going out from the computational domain. It replaces a long channel with fully developed flow at the exit of the flow domain by a single boundary condition.

2.3.6 Thermal boundary conditions

In addition to the flow boundary conditions introduced in subsection 2.3.5, to simulate the non isothermal flow and to solve the energy Equation 2.6 it was necessary to introduce into the simulator the thermal boundary conditions. In Figure 2.16 these boundary conditions [23] are represented.

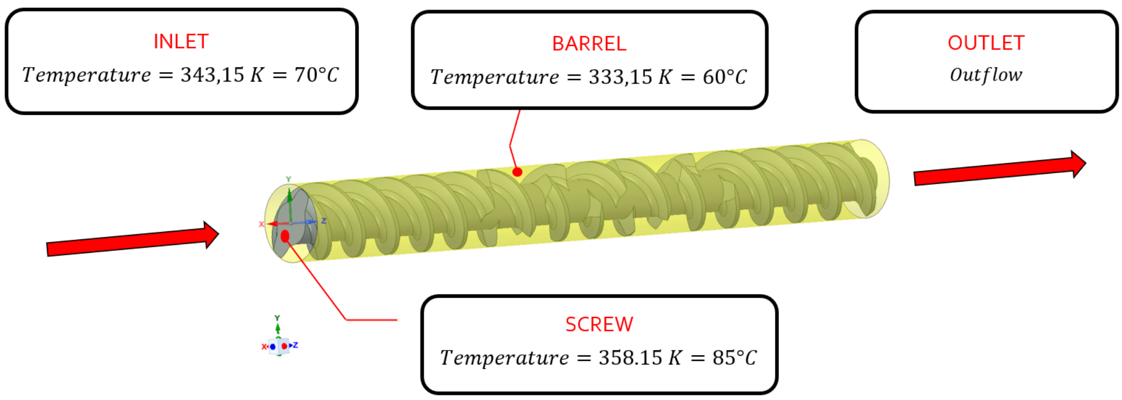

Figure 2.16: Representation of the thermal boundary conditions.

- Inlet: At the "Inlet" boundary section the condition "Temperature imposed" was introduced. In particular a constant temperature of 343,15 K (70° C) was chosen for the fluid entering into the computational domain.

- Barrel: At the Barrel boundary section the condition "Temperature imposed" was imposed as well. The temperature value was set at 333,15 K (60° C) based on the realistic operative conditions of the investigated single screw extruder.

- Screw: The "Temperature imposed" condition was prescribed also at the "Screw" boundary section, by setting a value of 358,15 K (85° C), based on the realistic operative conditions of the single screw extruder.

- Outlet: At the "Outlet" boundary section the condition "Outflow" was introduced. Similarly to the flow boundary conditions this condition let the simulator understand where the fluid is going out from the computational domain.

2.3.7 Material properties

When the problem is getting defined in ANSYS Polydata in addition to the introduction of the shear rate dependence of viscosity described in subsection 2.3.3, some other important properties related to the fluid must be selected:

- Temperature dependence of viscosity: In contrast to the shear rate dependence of the viscosity this option was neglected and viscosity was considered indipendent of temperature.

- Density: The hypotesis of incompressible flow was made and for this reason a constant density was chosen. In particular some experimental data of the density variation as a function of the temperature were received from the Continental AG researchers and an average value was fixed (1170 $\frac{\text{kg}}{\text{m}^3}$).

- Inertia terms: These terms were considered and the condition "Inertia will be taken into account" was selected.

- Thermal conductivity: A constant value was fixed for this property and in particular a value of 0,40 $\frac{\text{W}}{\text{m}\cdot\text{K}}$ was imposed. This is a typical value adopted in literature for melt processing (taken from the examples given with ANSYS Polyflow) and was confirmed by the Continental AG researchers as good approximation of the realistic thermal conductivity of the fluid.

- Heat Capacity per unit mass: A constant value was fixed for this property and in particular a value of 1600 $\frac{\text{J}}{\text{kg}\cdot\text{K}}$ was selected.

- Viscous plus wall friction heating: By default, viscous and wall friction heating (or dissipation) is neglected in the energy equation. To add viscous and wall friction heating to the energy equation it was necessary to select the option "Viscous + wall friction heating will be taken into account".

- Gravity: This option was neglected during the simulations.

Once the problem was totally set in ANSYS Polydata and once ANSYS Polyflow ended the computation a result file was generated. At this point the step of post processing was ready to get started.

2.4 Post processing

To analyse the results obtained from the simulations the software Paraview was adopted [28]. The flexibility of this applcation has made it popular among computational science areas such as Structural Analysis, Fluid Dynamics, Astrophysics which use methods like finite elements, finite volumes and point set. The visualization created by this application is powerful because it makes use of the Visualization Toolkit (VTK) which produces 3D graphics for data processing as well as the rendering engine. This software is able to read the file Ensight generated as ”file.case” by ANSYS Polydata. Once introduced the ”file.case” of our model into the software, Paraview allows us to create and apply filters to transform the data. There are several types of filters, each perfoming different operations and types of processing, and the most important adopted during the work are:

- Extract Block: This filter allows us to extract a certain part of the total geometry and in particular it was adopted to take some 3D pictures of the entire model generated.
- Slice: This filter cuts the input dataset with an implicit function such as a plane, a sphere, or a box. Since this filter returns data elements along the implicit function boundary, this is a dimensionality reducing filter. In fact if the input dataset has 3D elements like tetrahedrons or hexahedrons, the output will have 2D elements, line triangles and quads. The Slice filter can be used on any type of 3D dataset and the plane adopted used by this filter to cut the input dataset can be placed arbitrarily (by specifying the normal vector). Adopting this technique it is possible to visualize the physical properties of the fluid on the plane generated. Adopting this technique it was possible to obtain, on arbitrary planes, the contour plots of the main physical fields of the fluid.
- PointDataToCellData: This filter transforms data supplied per point into cell data by averaging the point data values of a cell. This was necessary as preliminary step to apply the filter Integrate Variables.
- Integrate Variables: This filter integrates point and cell data over lines and surfaces. It also computes length of lines, area of surface, or volume and allow us to calculate the area integral of each variable. For example it was used to calculate the average temperature on each Slice generated.

3. Results

In this chapter the results obtained from the simulations are discussed. Different aspects will be analysed and in particular for both geometries the following results will be examined:

- Contour plots of the main physical fields.
- Pressure rise as a function of the flow rate (the screw characteristic lines).
- Temperature profiles along the extruder.

To obtain the contour plots two slices perpendicular to the screw and one parallel (for both geometries), were considered:

- Slice 1 or Section 1; taken on the plane $z = 37$ cm.
- Slice 2 or Section 2; taken on the plane $z = 72$ cm.
- Slice 3 or Section 3; taken on the plane $x = 0$, which cuts the screw in half.

This choice was made to illustrate the main differences between the zone where the flight of the screw is present and the zone where is not. The three sections are illustrated in Figure 3.1 and in Figure 3.2.

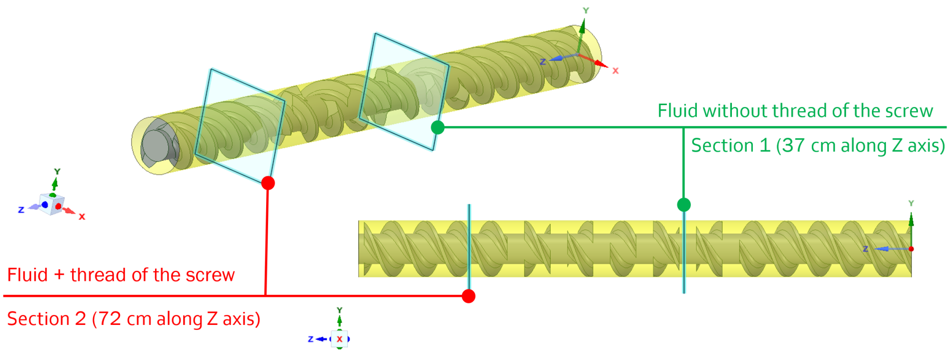

Figure 3.1: Location of Section 1 and Section 2.

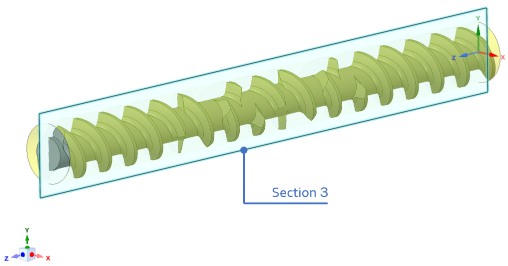

Figure 3.2: Location of Section 3.

Both isothermal and non isothermal simulations were conducted:

1. Isothermal simulations: In these simulations only the momentum transport equation was solved, neglecting heat transfer. For this case, contour plots relative to velocity, pressure and shear rate will be shown In particular contour plots relative to velocity, pressure and shear rate will be shown and the screw characteristic lines for both geometries will be evaluated.

2. Non isothermal simulations: In these simulations the non isothermal condition was introduced to solve also the energy transport equation. These simulations also provide the contour plots relative to temperature and viscous heating. In addition, by calculating the average temperature on several planes slicing the total geometry, the variation of the temperature along the extruder was evaluated.

3.1 Isothermal Simulations

The boundary conditions introduced to solve the momentum transport equation 2.1 are summarized in Figure 3.3. Whereas the main properties of the fluid are listed in Figure 3.4.

FLOW BOUNDARY CONDITIONS

1. $Inlet = Normal\ velocity\ 1\,\frac{cm}{s}$
2. $Screw = Angular\ Velocity\ 30\ rpm$
3. $Barrel = Zero\ Wall\ Velocity$
4. $Outlet = Outflow$

Figure 3.3: Boundary conditions for the isothermal simulations.

FLUID CHARACTERISTICS

- $Density = 1170\ \frac{Kg}{m^3}$
- $Inertia\ taken\ into\ account$

VISCOSITY

- $Power\ law\ \eta = K \cdot \gamma^{n-1}$ where
- $K = 120'000$
- $n = 0{,}1957$

Figure 3.4: Main properties of the fluid in the isothermal simulations.

To ease the comprehension of the inputs for the isothermal simulations a visual summary is reported in Figure 3.5.

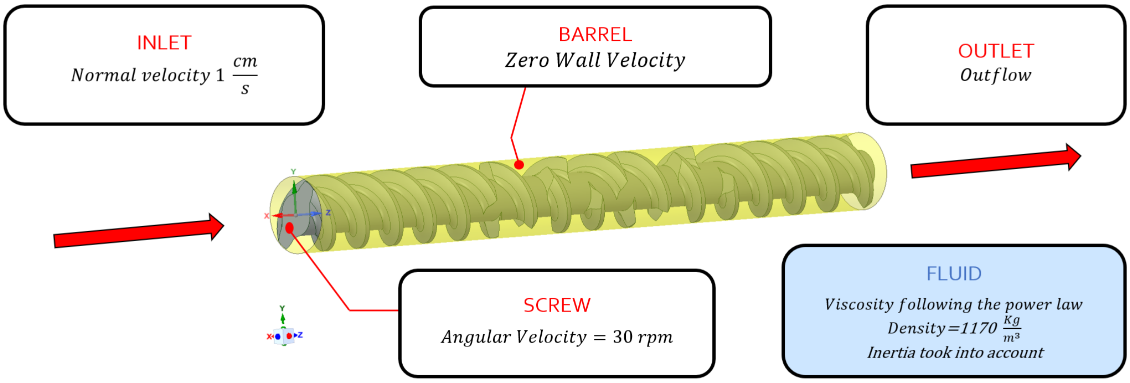

Figure 3.5: Summary of the inputs introduced into ANSYS Polyflow during isothermal simulations.

3.1.1 Isothermal contour plots for the *Nominal screw geometry*

The main feature of the flow field in the *Nominal screw geometry* is the presence of a backflow effect. A small portion of the fluid inside the extruder travels in the opposite direction to the main motion, thus enhancing mixing. To visualize this effect it is useful to analyse the contour plot of the z velocity component in section 3, as reported in Figure 3.6.

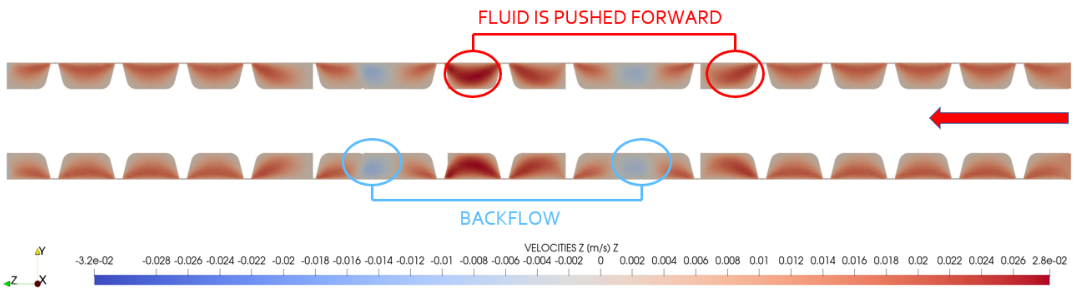

Figure 3.6: Contour plot of the z velocity component in section 3 for the *Nominal screw geometry.*

In Figure 3.6 the z velocity component is characterized by the red and the blue colors. Roughly, where the color is red the z velocity component is positive and it means that the fluid is pushed forward. On the contrary, where the z velocity component is blue, the value of this property is negative and in these zones the backflow effect is present. To understand in more detail how the backflow is generated it is necessary to analyse the two components of the net flow rate inside the extruder [3].

$$Q = Q_d + Q_p \tag{3.1}$$

where the first represents the contribution of drag flow (Q_d), and the second is the pressure flow (Q_p).

The drag flow is the flow between two surfaces caused by the movement of one relative to the other. In this case the fluid is dragged by the moving flight of the screw. Instead the pressure flow is the flow due to the pressure rise. In the regions where the drag flow is smaller, because of the absence of the flight of the screw, the counter flow generated by the pressure may prevail, resulting in the generation of the backflow effect. It is possible to confirm this result, looking at the z velocity component in section 1 (zone where the flight of the screw is not present) showed in Figure 3.7.

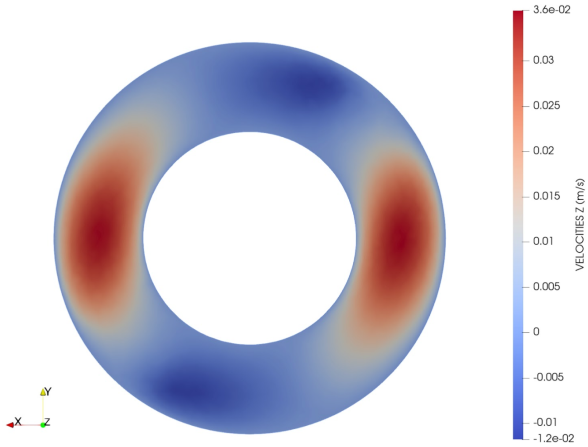

Figure 3.7: Contour plot of the z velocity component in section 1 for the *Nominal screw geometry*.

In fact, it can be seen that in several areas of the flow domain the z velocity component is negative, causing the backflow effect. Another confirmation is given by the contour plot of the z velocity component in section 2 (zone where the flight of the screw is present) showed in Figure 3.8.

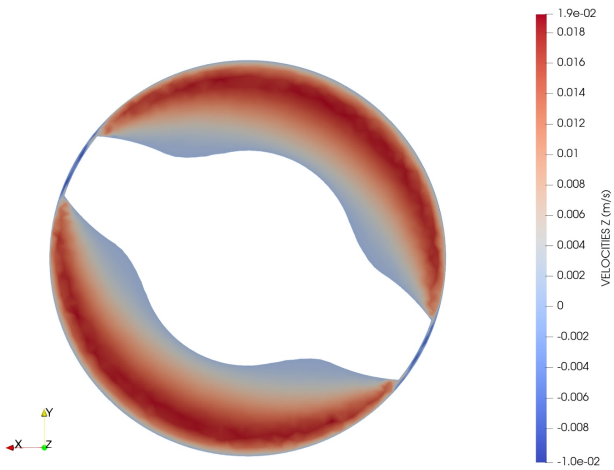

Figure 3.8: Contour plot of the z velocity component in section 2 for the *Nominal screw geometry*.

In Figure 3.8 it is possible to see that the backflow effect is not present in the same zones as section 1 but it is apparent only in the clearance of the screw (gap). The z negative velocity component in the gap is one order of magnitude less compared to z negative velocity component of Figure 3.7 and this demonstrates that the backflow effect is quite negligible into the gap. Another quantity which is worth to be investigated is the shear rate. The contour plot of this property in section 1 is showed in Figure 3.9.

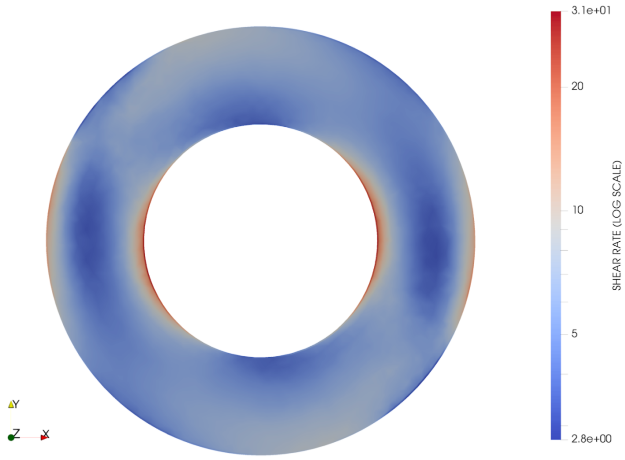

Figure 3.9: Contour plot of the shear rate ($\frac{1}{\mathrm{s}}$) in section 1 for the *Nominal screw geometry*.

In Figure 3.9 the shear rate is reported in logarithmic scale and it can be seen that the shear is more or less homogeneous. Section 1 represents the zone where the flight of the screw is not present and the fluid is free to flow without any forced path. For this reason the shear rate takes on relatively large values only near the walls. On the contrary in section 2 (Figure 3.10) the flight of the screw force the fluid to pass through the gap where the highest values of the shear rate can be observed.

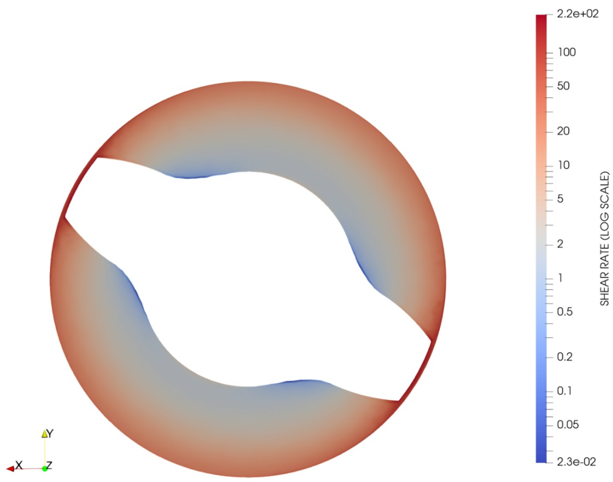

Figure 3.10: Contour plot of the shear rate ($\frac{1}{\mathrm{s}}$) in section 2 for the *Nominal screw geometry*.

It is interesting to analyze the contour plot of the pressure in section 3, showed in Figure 3.11.

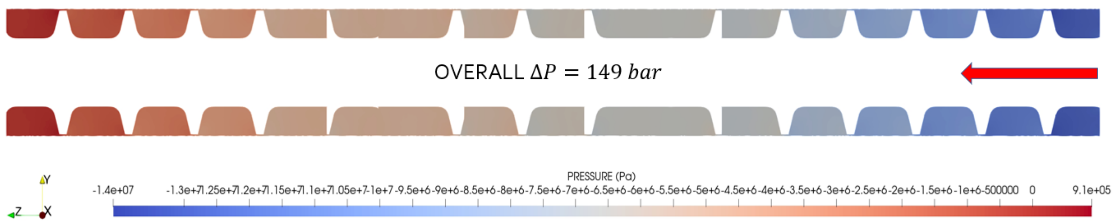

Figure 3.11: Contour plot of the pressure in section 3 for the *Nominal screw geometry*.

In Figure 3.11 the value of the pressure rise is calculated between the inlet and the oulet of the fluid domain. Because of the incompressibility assumption, the pressure calculated by ANSYS Polyflow is a relative value, characterized by a free additive constant. This is why the Figure 3.11 reports negative pressures. The value of the pressure rise calculated with the model is 149 bar, which compares fairly well with the experimental one (around 200 bar). The difference may be due to several reasons such as the hypotesis of incompressibility or the fact that we neglect both the elastic properties of the fluid and the dependence of the viscosity on the temperature. To conclude the analysis on the pressure relative to the *Nominal screw geometry* we extrapolated the variation of the average pressure along the extruder showed in Figure 3.12.

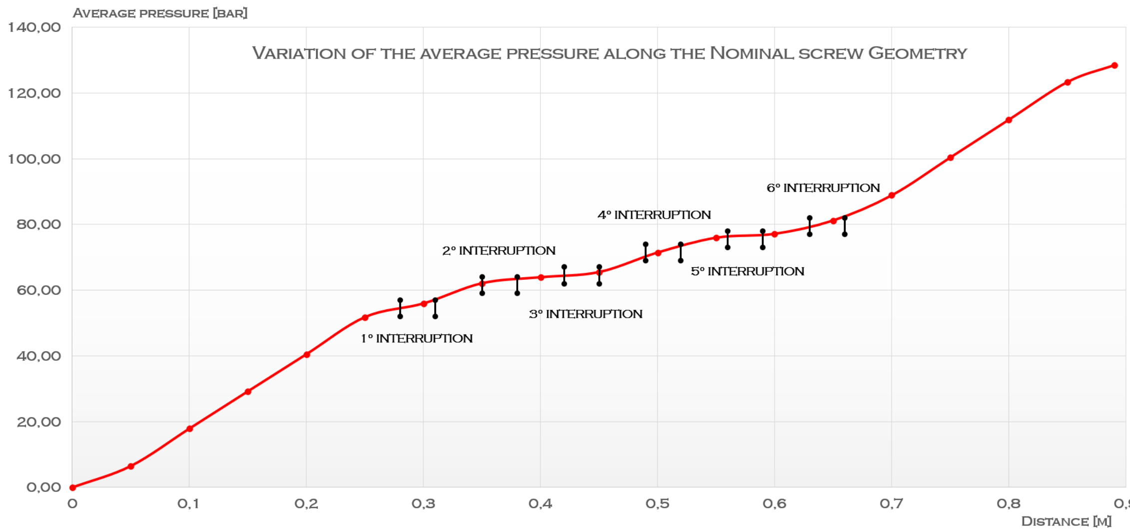

Figure 3.12: Variation of the average pressure along the extruder for the *Nominal screw geometry*.

It can be seen that in the zones where the flight of the screw is present the increase in the pressure is quite linear and steady, because there the fluid is just pushed forward. On the contrary in the zones where the flight of the screw is not present, some backflow occurs and consequently the pressure rises more slowly. In fact the fluctuations on the profile of pressure appear only in the zone where the interruptions of the flight are present. It is important to notice that the pressure jump calculated in Figure 3.12 (128 bar) is not perfectly equal to the pressure jump calculated from Figure 3.11 (149 bar) because in Figure 3.12 we considered the mean value of the pressure in the slice, where ΔP in Figure 3.11 was obtained from the peak values.

3.1.2 Isothermal contour plots for the *Full screw geometry*

The *Full screw geometry* was generated to show the main differences between the two kind of SSEs. Analysing the contour plot of the z velocity component in section 3 (Figure 3.13) it is possible to notice that in this case the backflow effect is not present and the fluid is only pushed forward.

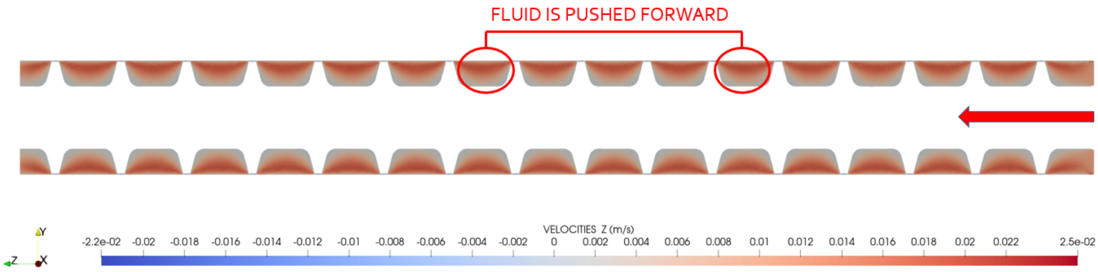

Figure 3.13: Contour plot of the z velocity component in section 3 for the *Full screw geometry*.

Figure 3.14 shows the distribution of the z velocity component on section 1.

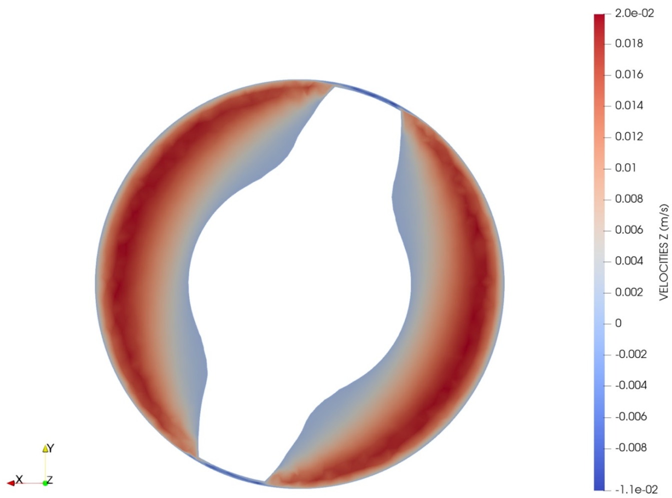

Figure 3.14: Contour plot of the z velocities reported in section 1 for *The Full Screw Geometry*.

The contour plot presented in Figure 3.14 looks very similar to the one showed in Figure 3.8 but in this case the same velocity distribution can be observed at any transversal plane along the z direction. Furthermore, it can be seen that the backflow effect is limited to the gap region. Figure 3.15 reports the shear rate contour plot in section 2. Again, the distribution is very similar to that showed in Figure 3.10, with the largest values of shear rate observed in the gap region and much lower values in the bulk of the fluid. In the *Full screw geometry* the shear rate distribution is the same for any transversal plane taken along z direction.

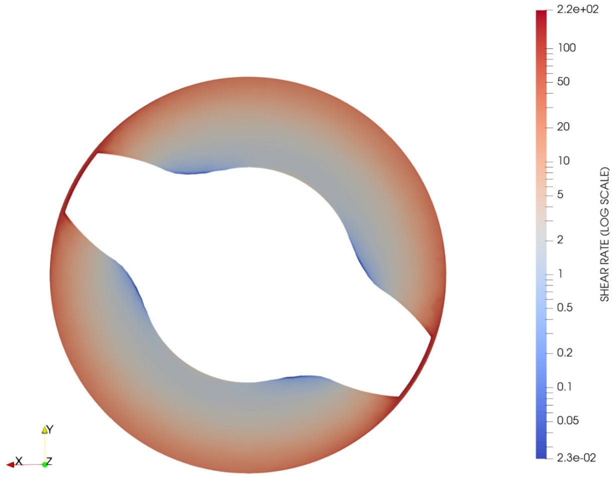

Figure 3.15: Contour plot of the shear rate $(\frac{1}{s})$ in section 2 for the *Full screw geometry*.

It is more interesting to analyse the contour plot of the pressure in section 3 which is reported in Figure 3.16.

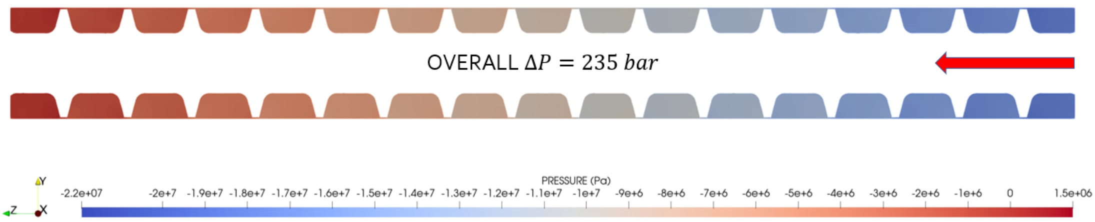

Figure 3.16: Contour plot of the pressure in section 3 for the *Full screw geometry*.

The value of the pressure rise generated between the inlet and the outlet in this case is 235 bar. This increase in the value of the pressure can be for sure correlated to the fact that the fluid is forced to follow the motion of the screw and this is one of the main differences between the two geometries. In fact, since there are not empty spaces, the fluid is only dragged by the motion of the screw and no relevant backflow can be observed. Also for the *Full screw geometry* the average variation of the pressure along the extruder was evaluated and shown in Figure 3.17. In this case the pressure is increasing linearly along the extruder and this is due to the fact that only the drag flow is present. Also in this case the pressure jump calculated in Figure 3.17 (181 bar) differs from the jump calculated in Figure 3.16 (235 bar).

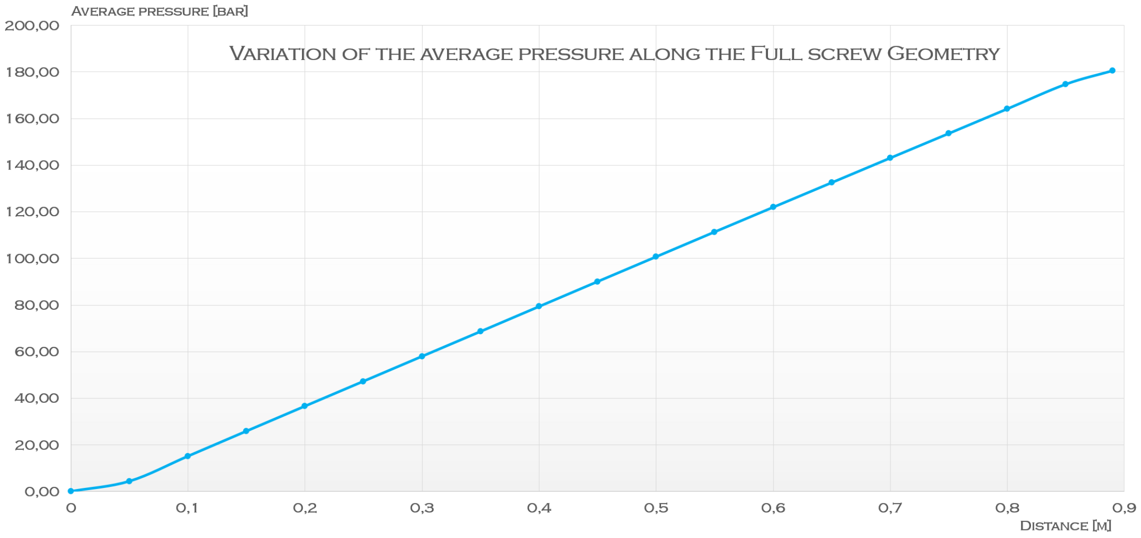

Figure 3.17: Variation of the average pressure along the extruder for the *Full screw geometry*.

To conclude the analysis on the isothermal contour plots and to highlight the main differences between the two geometries some details of the z component velocity contour plots are shown. Figure 3.18 shows a magnification relative to the empty spaces in the *Nominal screw geometry*, where the backflow effect is present.

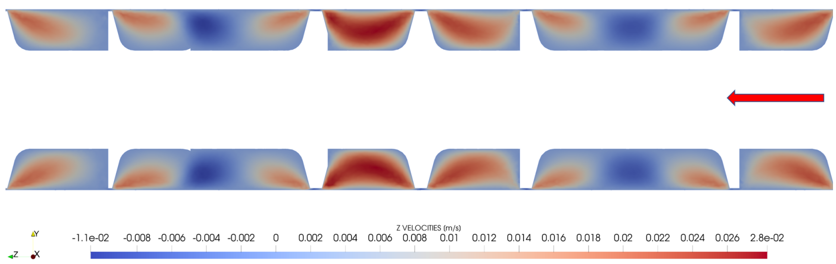

Figure 3.18: Details of the backflow effect in the *Nominal screw geometry*.

The same zone of the extruder but relative to the *Full screw geometry* is shown in Figure 3.19 and it can be highlighted that the backflow effect is present only into the gap zone.

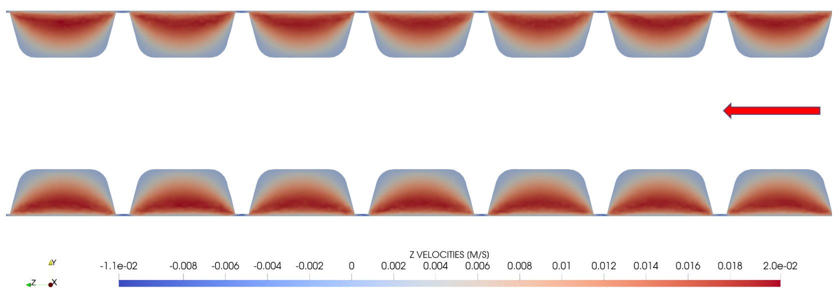

Figure 3.19: Details of the backflow effect (gap) in the *Full screw geometry*.

3.1.3 Screw characteristic lines for the *Nominal screw geometry*

The Single Screw Extruder is generally equipped with a die, and the flow rate of the extruder as well as the pressure rise depends on their coupling. The characteristic [3] of a screw or a die is the line that relates the pressure rise (in a screw) or drop (in a die) and the flow rate. For Newtonian fluids the curve are straight lines, as shown in Figure 3.20.

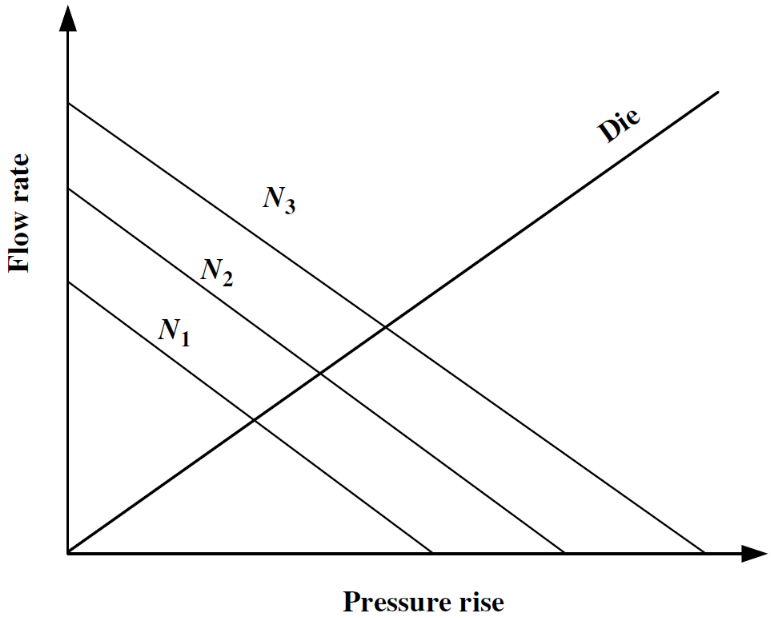

Figure 3.20: Screw characteristic lines at three screw speeds $N_1 < N_2 < N_3$ and the die characteristic line.

The operating point, that is, the flow rate and pressure value at which the system will operate, is the cross-point between the two characteristic lines, when the pressure rise over the screw equals the pressure drop over the die. The aim of this work was to calculate the screw characteristic lines for the investigated systems. To obtain two different screw characteristic lines the simulation was made a two different angular velocities: respectively 30 rpm (the value adopted in the main simulations) and 60 rpm. The value of inlet velocity was ranged between 0 and 1.5 $\frac{\text{cm}}{\text{s}}$ for the simulations made at 30 rpm and between 0 and 2.5 $\frac{\text{cm}}{\text{s}}$ for the simulations made at 60 rpm. Each inlet velocity corresponds to a different value of the volumetric flow rate. By changing the inlet velocity (and consequently the volumetric flow rate) it was possible to calculcate the pressure rise between the inlet and the outlet. A summary of the conditions introduced to realize the simulations is reported in Figure 3.21.

30 rpm	INLET VELOCITY [cm/s]	FLOW RATE [m3/s]	PRESSURE [bar]
	0,0	3,75E-07	395,8
	0,5	1,87E-05	276,0
	1,0	3,75E-05	138,6
	1,5	5,62E-05	48,0
		6,30E-05	0,0
60 rpm	INLET VELOCITY [cm/s]	FLOW RATE [m3/s]	PRESSURE [bar]
	0,0	3,75E-07	454,3
	0,5	1,87E-05	396,1
	1,0	3,75E-05	316,1
	1,5	5,62E-05	231,5
	2,0	7,49E-05	170,0
	2,5	9,36E-05	103,4
		1,32E-04	0,0

Figure 3.21: Input velocity, volumetric flow rate and the pressure rise calculated for the *Nominal screw geometry* simulations.

Since the volumetric flow rate at which the pressure drop was nil was not known a priori, it was necessary to extrapolate it by a linear interpolation. The values summarized in the table are plotted in Figure 3.22.

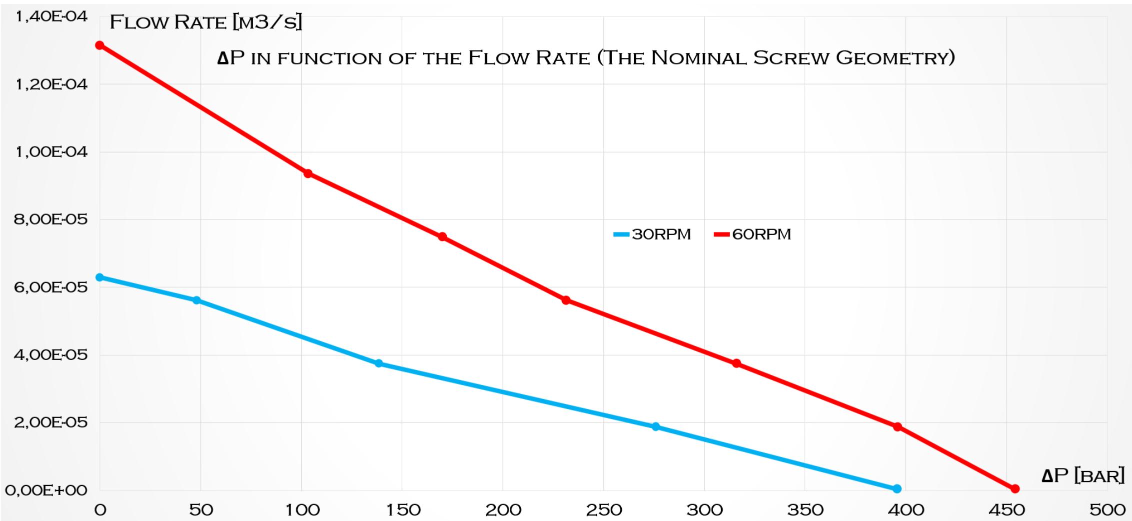

Figure 3.22: Screw characteristic lines for the *Nominal screw geometry*.

Differently from the screw characteristic lines reported in Figure 3.20 in this case the lines are not perfectly straight. This fact is due to the non-Newtonian behaviour of the polymer. It is interessing to notice that under the same flow rate introduced, the pressure rise generated at 60 rpm is higher compared to that at 30 rpm. The importance of Figure 3.22 relies on the fact that if the characteristic line of the die is known, the operating conditions of the extruder can be promptly derived, as schematically illustrated in Figure 3.20.

3.1.4 Screw characteristic lines for the *Full screw geometry*

The same study was made also for the *Full screw geometry*. In this case the conditions are reported in Figure 3.23.

30 rpm	INLET VELOCITY [cm/s]	FLOW RATE [m3/s]	PRESSURE [bar]
	0,0	3,75E-07	541,5
	0,5	1,87E-05	373,7
	1,0	3,75E-05	191,7
	1,5	5,62E-05	70,3
		6,75E-05	0,0
60 rpm	**INLET VELOCITY [cm/s]**	**FLOW RATE [m3/s]**	**PRESSURE [bar]**
	0,0	3,75E-07	621,6
	0,5	1,87E-05	538,3
	1,0	3,75E-05	428,0
	1,5	5,62E-05	315,1
	2,0	7,49E-05	219,5
	2,5	9,36E-05	144,0
		1,27E-04	0,0

Figure 3.23: Input velocity, volumetric flow rate and the pressure rise calculated for the *Full screw geometry* simulations.

And reporting these values on a graph, the plot shown in Figure 3.24 is obtained.

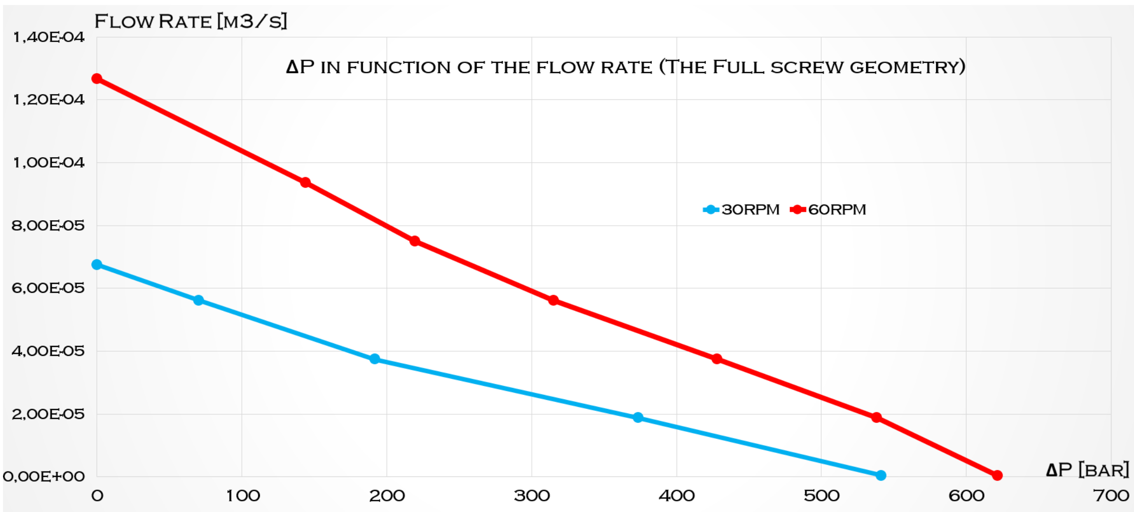

Figure 3.24: Screw characteristic lines for *The Full Screw Geometry*

The situation is pretty similar to the one relative to the *Nominal screw geometry* shown in Figure 3.22. The main difference is the higher pressure rise that originates between the inlet and the outlet. To highilight this difference both series of curves were plotted in the same graph, as reported in Figure 3.25.

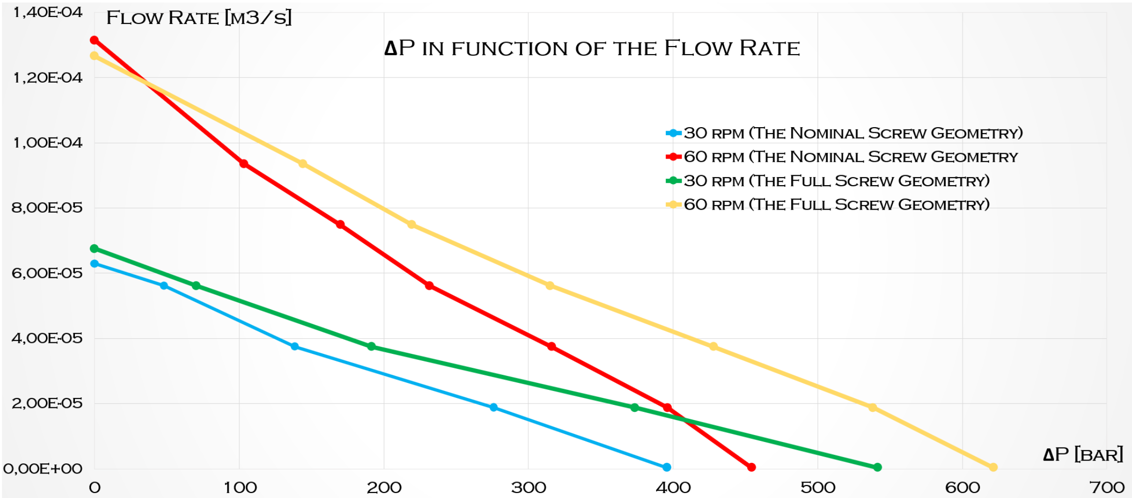

Figure 3.25: Comparison between the screw characteristic lines of the two geometries

The screw characteristic lines present indeed a similar behaviour but a different pressure rise. In fact, considering the same volumetric flow rate at the inlet, the screw characteristic lines for the *Full screw geometry* are translated to higher values of pressure compared to the case of the *Nominal screw geometry*.

3.2 Non Isothermal Simulations

This section shows the results obtained from the non isothermal simulations. The main conditions prescribed in ANSYS Polydata for these simulations are reported in Figure 3.26 and Figure 3.27.

THERMAL BOUNDARY CONDITIONS

1. $Inlet = Temperature\ imposed\ 343.15\ K\ (70°C)$
2. $Screw = Temperature\ imposed\ 358.15\ K\ (85°C)$
3. $Barrel = Temperature\ imposed\ 333.15\ (60°C)$
4. $Outlet = Outflow$

Figure 3.26: Thermal conditions for the non isothermal simulations.

THERMAL FLUID CHARACTERISTICS

- $Heat\ Capacity\ = 1600\ \frac{J}{Kg \cdot K}$
- $Thermal\ Conductivity = 0.40\ \frac{W}{m \cdot K}$
- $Viscous\ heating\ taken\ into\ account$

Figure 3.27: Fluid properties in the non isothermal simulations

It is important to specify that these additional parameters were introduced along with the already discussed flow boundary conditions (Figure 3.3 and Figure 3.4). Therefore the momentum transport equation and the energy balance equation were solved simultaneously. This was not actually required, as the energy transport could be solved on the ”frozen” velocity flow field since we did not consider the effect of temperature on the viscosity. However, the simultaneous solution of the momentum and energy trasnport equation came with only a moderate increase of the computational effort. In fact for example for the *Nominal screw geometry* the flow field was simulated in about 16500 seconds (around 5 hours) and instead the simultaneous solution of flow and temperature fields took more or less 31000 seconds (around 9 hours) to get computed. Figure 3.28 reports all the parameters used in the non isothermal simulations.

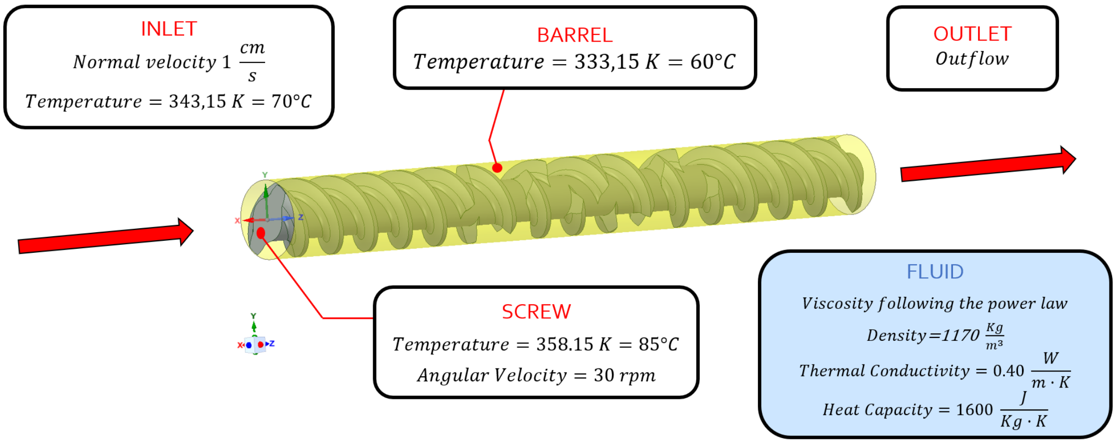

Figure 3.28: Summary of the inputs introduced into *ANSYS Polydata* during the non isothermal simulations.

3.2.1 Temperature profiles for non isothermal simulations

To better introduce the analysis on the temperature profiles for both geometries it is important to analyse the contour plots relative to the viscous heating (Figure 3.29) and the shear rate (Figure 3.30).

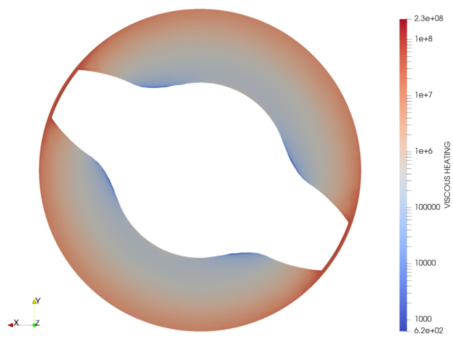

Figure 3.29: Contour plot of the viscous heating in section 2 for the *Nominal screw geometry*.

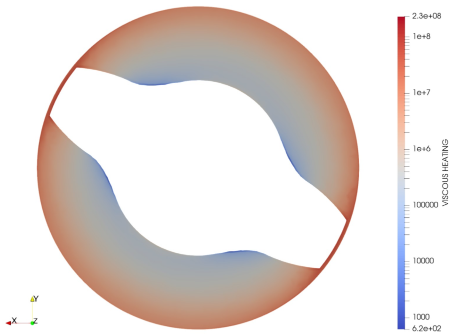

Figure 3.30: Contour plot of the shear rate in section 2 for the *Nominal screw geometry*.

The contour plots shown in Figure 3.29 and in Figure 3.30 regard the *Nominal screw geometry* but the same phenomena appear in both geometries. It can be seen that the viscous heating (reported on a logarithmic scale) has the highest values in the gap where also the shear rate presents its highest values. This means that where the flight of the screw is present the viscous heating is higher compared to the zones where the flight is not present. However, the flight of the screw also enhances the heat transfer from the fluid to the cold wall of the barrel, favouring the cooling of the fluid in the regions where the flight is present. Consequently, we have two contrasting effects and the numerical simulation can identify the prevailing one. Now it is possible to introduce the contour plots of the temperature on section 3 for the *Nominal screw geometry* (Figure 3.31) and for the *Full screw geometry* (Figure 3.32).

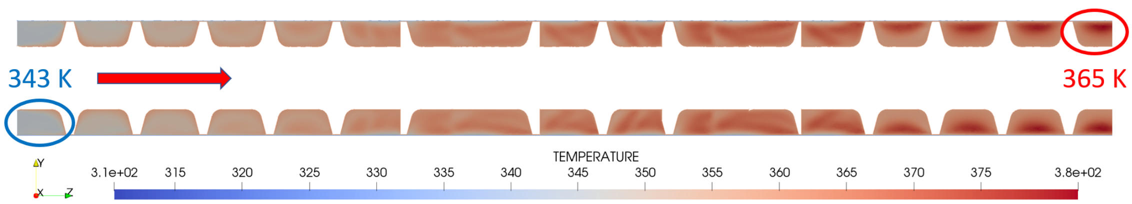

Figure 3.31: Contour plot of the temperature in section 3 for the *Nominal screw geometry*.

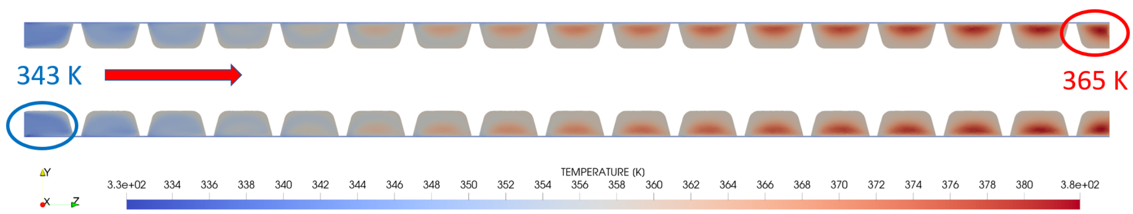

Figure 3.32: Contour plot of the temperature in section 3 for the *Full screw geometry*.

Notice that in this case the main flow motion is from left to right to make the comparison easier with the temperature profiles shown in Figure 3.33.

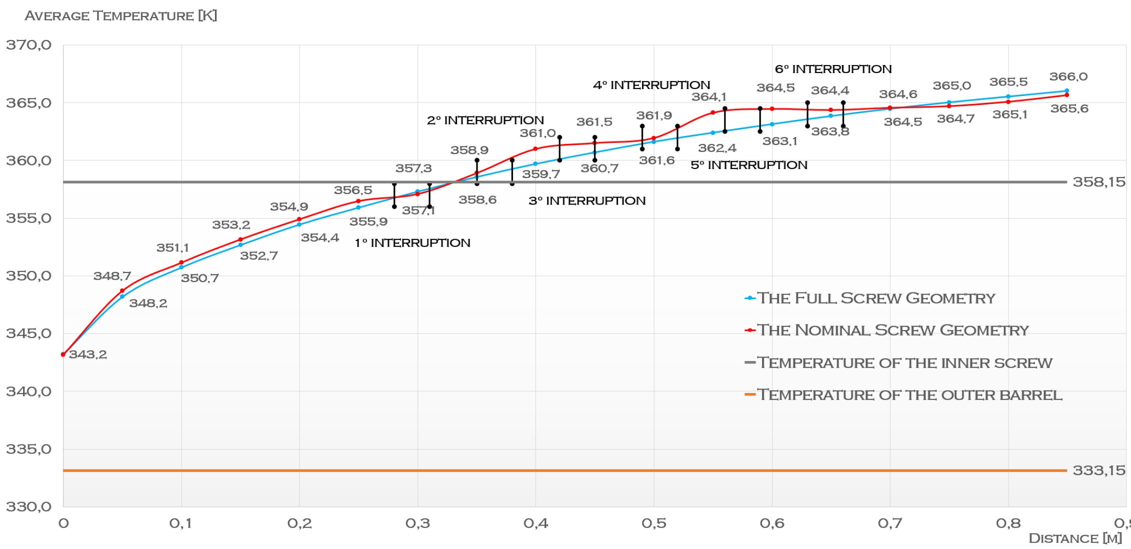

Figure 3.33: Comparison between the axial profiles of temperature in the two models. Temperatures are averaged over the cross-sections.

In this figure on the horizontal axis the distance along the z direction (m) and on the vertical axis the average temperature (K) are reported. To obtain this plot the area-weighted temperatures were calculated on 18 parallel and equidistant slices. In Figure 3.33 it is important to notice that the variation of the temperature is not constant along the z direction of the extruder. In fact, if we look at the graph from the left to the right we can see that till a distance of 35 cm the fluid presents an average temperature which is lower compared to the screw one. This means that the fluid is heated up both by the viscous heating and the heat transfer from the screw. A part of the total heat acquired is lost in the heat transfer to the barrel which presents always a lower temperature compared to the one of the fluid. For this reason in the first section of the extruder the temperature profile increases with an higher slope. On the contrary, starting from a distance of 35 cm, the fluid presents a temperature which is higher compared to the one of the screw. As a consequence, a part of the heat generated by the viscous heating is lost because of the heat transfer to the screw and to the barrel, resulting in a decrease of the slope of the temperature profile. This phenomenon continues till the temperature profile reaches a plateau, where the temperature can be considered more or less constant. At this point we have almost a complete balance between the heat generated by viscous heating and the heat transferred to the barrel and the screw. Now it is possible to analyse the temperature profiles relative to the two geometries. For the *Nominal screw geometry* it can be seen that the temperature profile presents abrupt variations of the slope where the flight of the screw is interrupted. In fact the reduction of the heat transfer to the walls favours the increase of the average temperature of the fluid. On the contrary, the *Full screw geometry* does not present these variations in the slope because it is characterized by a full flight of the screw.

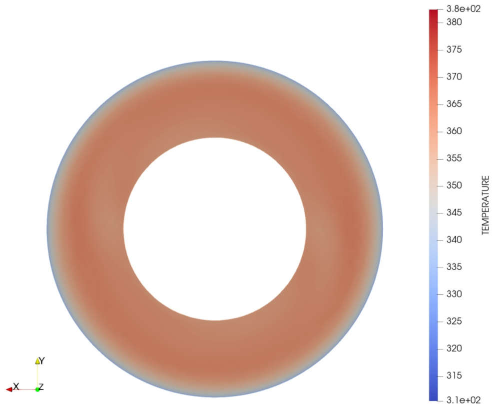

Figure 3.34: Contour plot of the temperature (K) in section 1 for the *Nominal screw geometry*

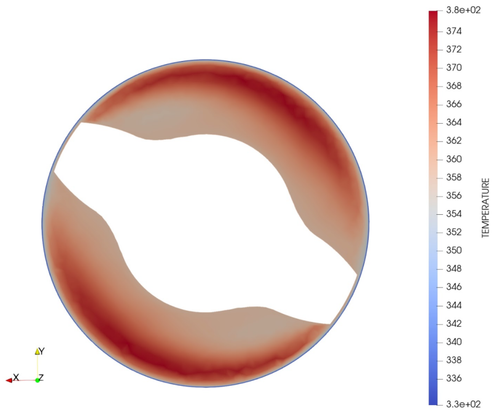

Figure 3.35: Contour plot of the temperature (K) in section 2 for the *Nominal screw geometry*

In Figure 3.34 and in Figure 3.35 the temperature contour plots relative to the *Nominal screw geometry* are shown. It is important to notice that in Figure 3.34 the flight of the screw is not present and the heat generated by the viscous heating is less compared to the section 2 reported in Figure 3.35 (where the flight of the screw is present). For this reason in section 1 the fluid results heated up in a more homogeneously way compared to the section 2 where the highest value of the temperature is reached near the barrel due to the effect of the viscous heating. In Figure 3.36 and in Figure 3.37 the temperature contour plots relative to the *Full screw geometry* are shown:

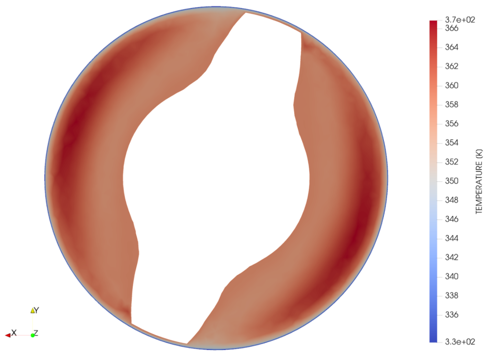

Figure 3.36: Contour plot of the temperature (K) in section 1 for the *Full screw geometry.*

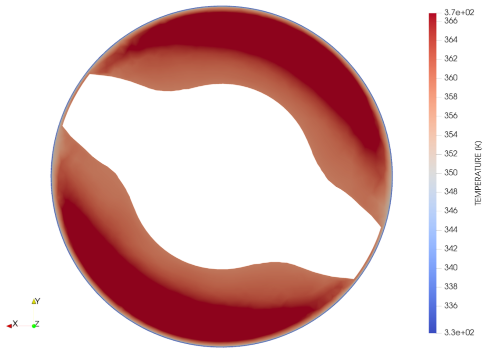

Figure 3.37: Contour plot of the temperature (K) in section 2 for the *Full screw geometry.*

In this case the fluid is heated up by viscosity in the same way at any axial coordinate of the extruder.

As a last element of information to finish the analysis, the computational times for the simulations are reported:

- Isothermal simulation of the *Nominal screw geometry* = 16500 s (around 5 hours)
- Non isothermal simulation of the *Nominal screw geometry* = 31000 s (around 9 hours)

- Isothermal simulation of the *Full screw geometry* = 21000 s (around 6 hours)
- Non isothermal simulation of the *Full screw geometry* = 72000 s (around 20 hours)

The computational time for the non isothermal simulation relative to the *Full screw geometry* has an higher value compared to the others because some problems relative to the convergence of the problem occurred. For this reason it was necessary to use specific techniques (Evolution [29]) to reach the convergence, increasing the computational time.

4. Conclusions

The aim of this work was the realization of a CFD model that could simulate one of the devices used at the R & D laboratories of Continental AG. Thanks to the analysis of theoretical models and to the Computational Fluid Dynamics (CFD) it was possible to set both isothermal and non isothermal simulations for this system. Two geometries were examined to better understand the response of the system: The single screw extruder used at Continental AG (the *Nominal screw geometry*), characterized by the interruption of the flight of the screw, was compared with a specific geometry (the *Full screw geometry*) characterized by a continuous flight in the transport of a pseudoplastic fluid with power law viscosity. During the set up of the simulations also other important simplifications were made: the fluid was assumed incompressible and we also neglected the dependence of the viscosity on the temperature. On the contrary the inertia of the fluid and the viscous heating were taken into account. To perform steady state simulations a reference frame was fixed to the screw and we let the barrel rotate. In this way the flow domain does not change in time and the stationary simulations were possible. Thanks to the comparison between the two models it was possibile to evaluate the main features of the *Nominal screw geometry*, such as the backflow effect and the profiles of pressure and temperature inside the extruder. In fact, different countour plots were analysed to highlight where the backflow effect occurs and the consequences it has on the temperature and pressure profiles. It was shown that in the zones where the flight of the screw is not present the backflow enhances local mixing, resulting in an homogeneusly distribution of the temperature. At the same time the backflow effect causes the variation of the slope of the pressure profile and the pressure rise inside the *Nominal screw geometry* is lower compared to the *Full screw geometry*. Satisfatory agreement between the model created and the actual operating conditions of the extruder was found. For example, the pressure rise predicted by the model is around 150 bar and the one calculated experimentally is around 200 bar. The difference between the values can be related to the simplifying hypotesis we did and to the fact that the real fluid may have elastic components that were not considered in the rheological equation. A challenge for studies on this system could be to add the dependence of the viscosity on the temperature or the variation of the density with the temperature. These effects were not considered to reduce the complexity of the simulations. Another possibility for future studies could be to change the topology of the mesh or adopt another solution tecnique, such us the superposition or the sliding mesh tecnique to better assess the quality of the solution.

A. Geometry realization

In this Appendix A all the passages made to realize both the geometries are illustrated. Before starting, however, it is important to underline the parameters introduced into the software:

- Lenght of the screw: 90 cm
- Diameter of the screw without the relative flight = 50 mm
- Diameter of the screw considering the flight = 90 mm
- Diameter of the external barrel = 92 mm

The first step was the realization of the flight of the screw in 2D. In a first moment just one flight of the screw was realized in the upper part of a 3D cylinder. To obtain the final 2D sketch of the orthogonal section of the screw (Figure A.1) another flight was created in the bottom part.

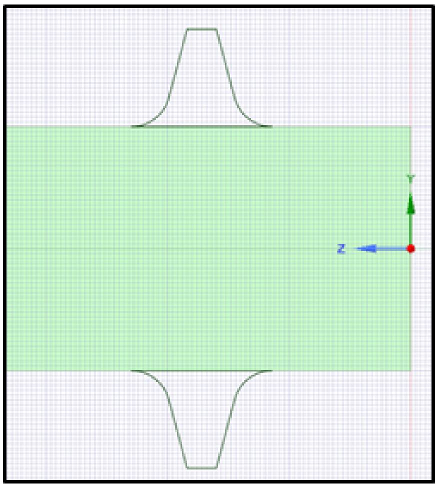

Figure A.1: Final 2D sketch of the orthogonal section of the screw adopted to generate the 3D model.

Once the 2D sketch was ready, the remaining step was to realize the 3D model adopting the classic command "Sweep" present in all the common CADs. By selecting both the flights of the screw present into the 2D sketch and by sweeping them, fixing the pitch, around the 3D cylinder, it was possible to create the final geometry (in the case the *Full screw geometry* the process was stopped here). The final result is showed in Figure A.2.

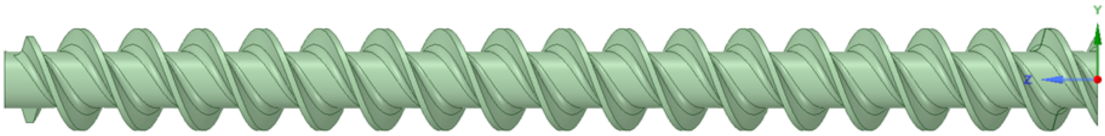

Figure A.2: Final 3D representation of the *Full screw geometry* realized on SpaceClaim.

To realize the *Nominal screw Geometry* it was necessary to realize the empty spaces which are interrupting the flight of the screw. To realize them, the first step was to design an annular cylinder which intersects the total 3D model created. In Figure A.3 a representation of the 3D annular cylinder is showed.

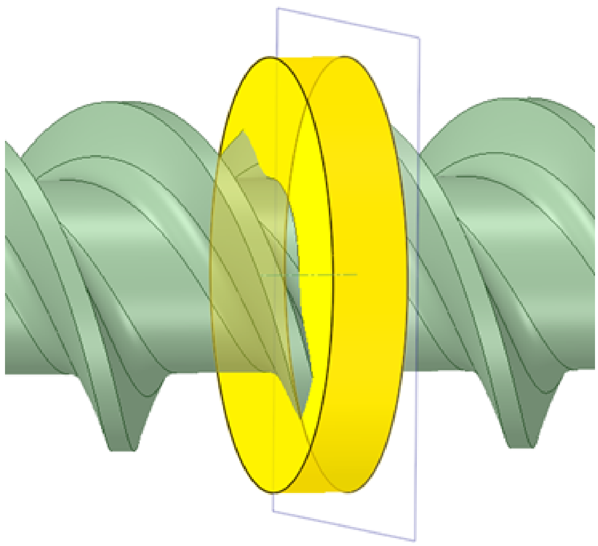

Figure A.3: Representation of the annular cylinder adopted to realize the empty spaces which are interrupting the flight of the screw.

At this point, the final passage was to use the command "Subtraction" to delete the intersections between the annular cylinder and the total 3D model created. In this way all the necessary empty spaces were created and the *Nominal screw geometry* was finally ready. The final model is reported in Figure A.4.

Figure A.4: Representation of the final *Nominal screw geometry* with its quotes.

After the creation of the 3D model, a barrel was added around it considering a gap of 1 mm. In Figure A.5 the representation of the barrel and a detail of the gap are reported.

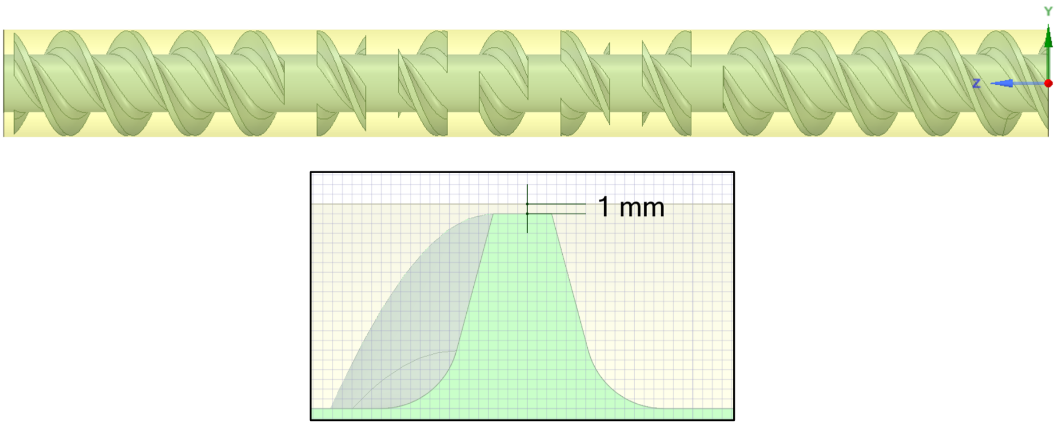

Figure A.5: Representation of the barrel and a detail of the gap.

To complete the study on the geometry, the process to extrapolate the volume of fluid is described. To realize this step it was necessary to use the command "Volume Extraction" present into ANSYS SpaceClaim. First of all it was necessary to select the two surfaces which were delimiting the volume of fluid present between the internal wall of the barrel and the external wall of the screw. The surfaces selected are shown Figure A.6.

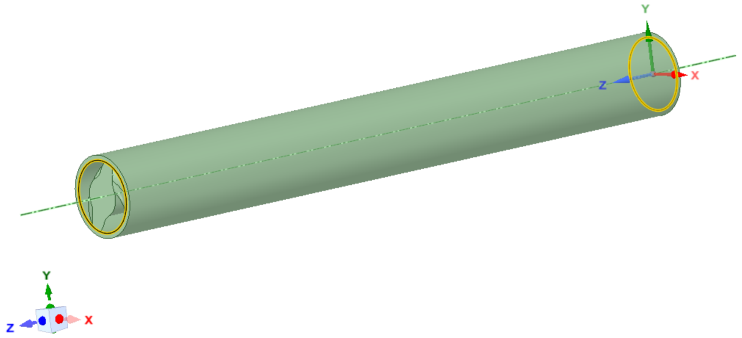

Figure A.6: Representation of the two surfaces delimiting the volume of fluid.

After the selection of the two surfaces, using the command "Volume Extraction" ANSYS SpaceClaim was able to generate automatically the volume of fluid. The final result is showed in Figure A.7.

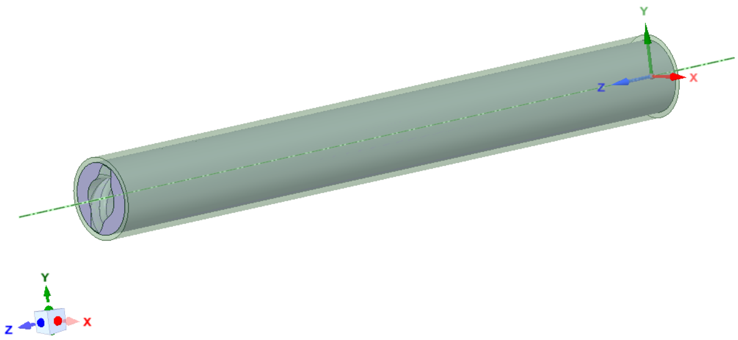

Figure A.7: Representation of the volume of fluid extrapolated.

At this point, to obtain only the volume of fluid (Figure A.8), it was necessary to delete the internal 3D screw and the barrel.

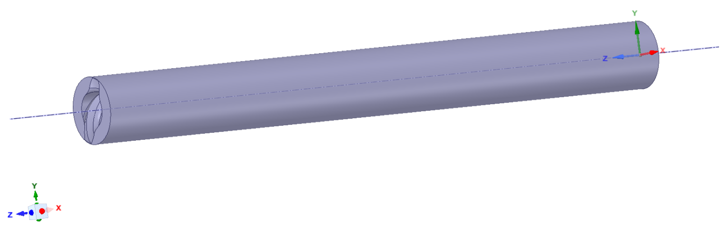

Figure A.8: Final representation of the 3D volume of fluid extrapolated and ready to be meshed.

Once the volume of fluid was finally obtained it was ready to get meshed on ANSYS ICEMCFD.

B. Mesh realization

This section describes the passages needed to realize the mesh on the generated geometries. In particular it is reported only the method to mesh the *Nominal screw geometry* because it is valid for both ones. This appendix is a short tutorial on the little experience I had with ANSYS ICEM CFD in the hope to help someone who could be in trouble with this software.

The first step was to introduce the geometry realized in Appendix A in ANSYS ICEM CFD and to create the four boundary sections (Inlet, Innerwall, Outerwall and Outlet). Once the four boundary sections were created, it was necessary to apply a topology on the geometry (there is a dedicated section on [19]). The result obtained is reported in Figure B.1.

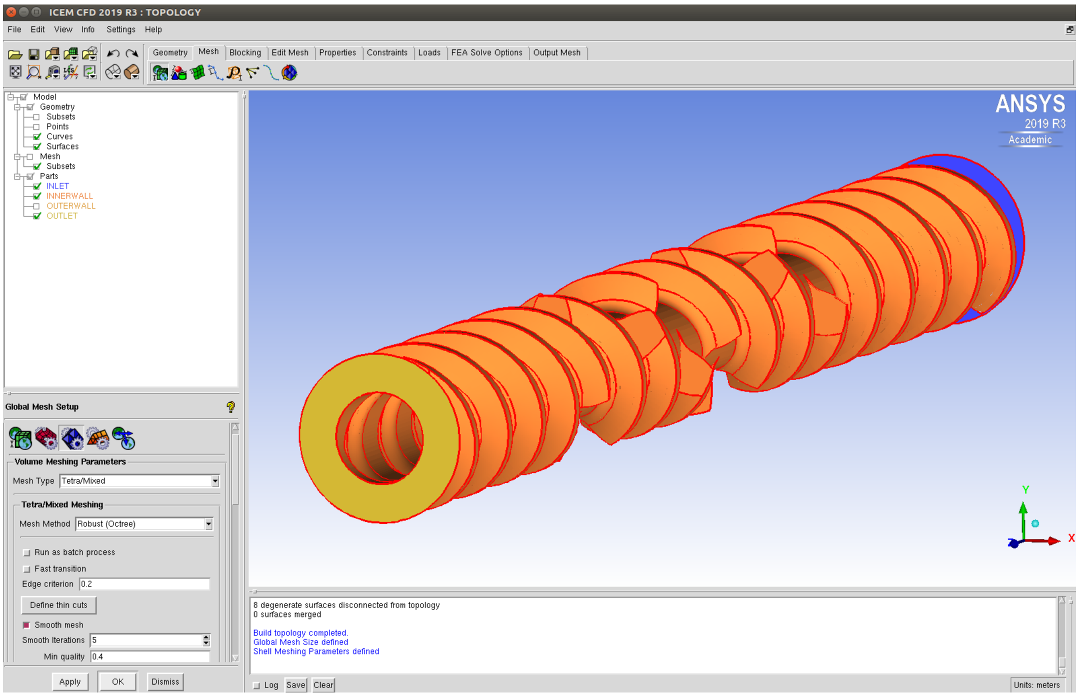

Figure B.1: Application of the topology on the geometry created.

After the realization of the topology, the mesh can be applied on the geometry but first of all it is necessary to move to the section Mesh of the code as shown in Figure B.2.

Figure B.2: Mesh command present into ANSYS ICEM CFD.

By clicking on the first icon reported on the left in Figure B.2, the tree setup of Figure B.3 will be shown.

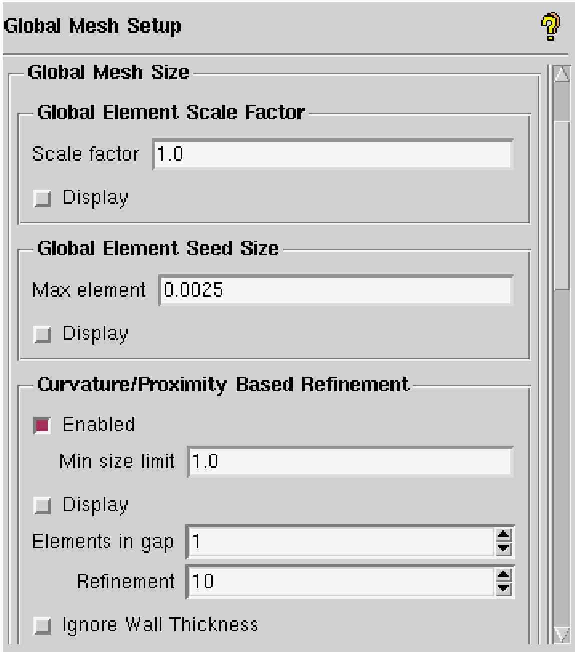

Figure B.3: Global Mesh Setup present into ANSYS ICEM CFD.

In this tree it is possible to set the size of the tetrahedric elements which will be applied on the volume of the fluid. In Figure B.3 the actual size of the tetrahedric elements (2,5 mm) adopted to realized the mesh, is reported. In this tree it is possibile just to select the global mesh setup and the next step is to select which kind of Surface Mesh should be applied to the geometry. The Surface Mesh button is reported in Figure B.4.

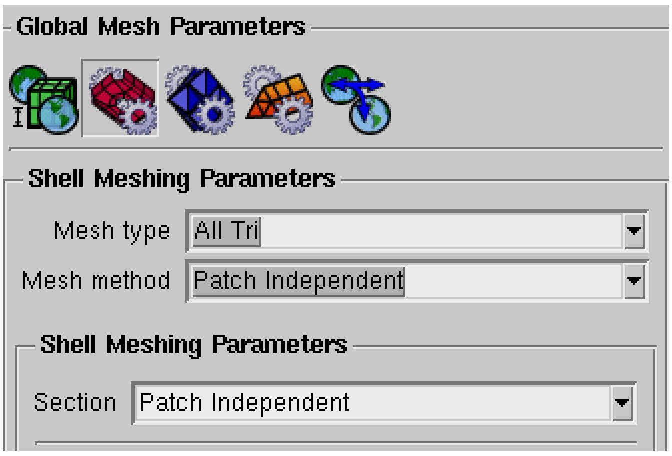

Figure B.4: Surface Mesh Setup present into ANSYS ICEM CFD.

In this menu it is necessary to select which kind of mesh we want to apply for the surfaces. The "All Tri" method was selected, which it is constituted only by tethraedral elements. Patch Indipendent is the standard choice of the software and this choice was mantained.

The next necessary step is to select the Volume Mesh reported in Figure B.5.

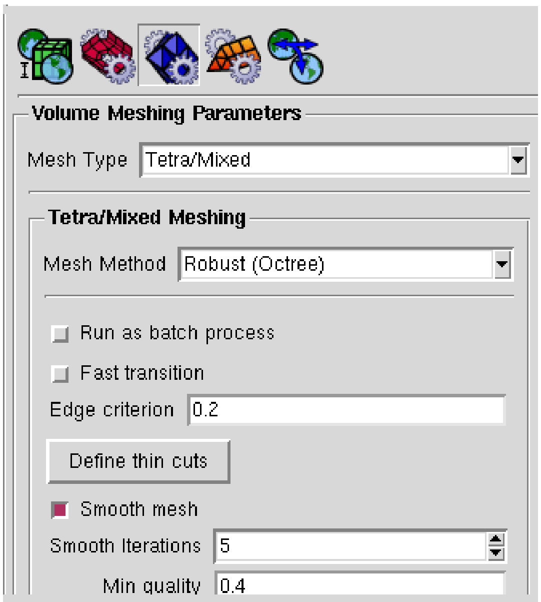

Figure B.5: Volume Mesh Setup present into ANSYS ICEM CFD.

For the moment the method Robust(Octree) must be selected, but, as it will be detailed in the following, the procedure will be repeated later using the Quick method. The information about these methods is reported in [19]. A final step is necessary before the creation of the total mesh and this step is the setup of the prisms that will be adopted to refine the mesh in the critical zones like the gap and the external wall of the screw. The setup of the prisms is reported in Figure B.6.

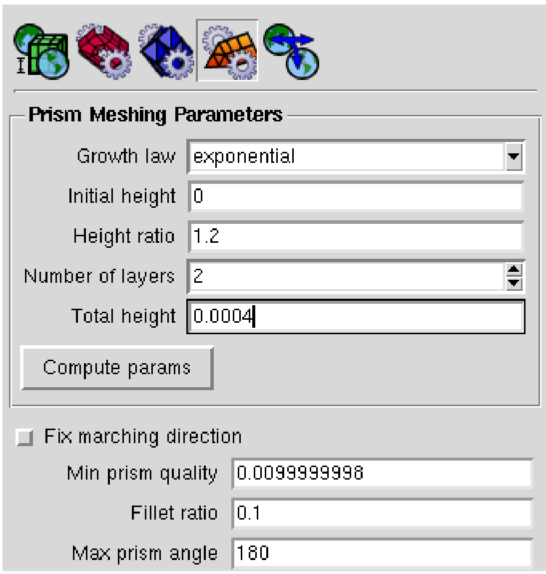

Figure B.6: Prism Mesh Setup present into ANSYS ICEM CFD.

The layer where the prisms are created is set to 0.4 mm because in this way ANSYS ICEM CFD generates automatically these prisms inside the gap and along the surface of the screw. The number of the layers represents the nodes present inside the total height of the layer and it was set to two.

Finally by pressing the command Compute Mesh (the last icon on the right in Figure B.2) it is possible to obtain the first final mesh which is based on the Robust (Octree) method (the computation will take a while to realize), as shown in Figure B.7.

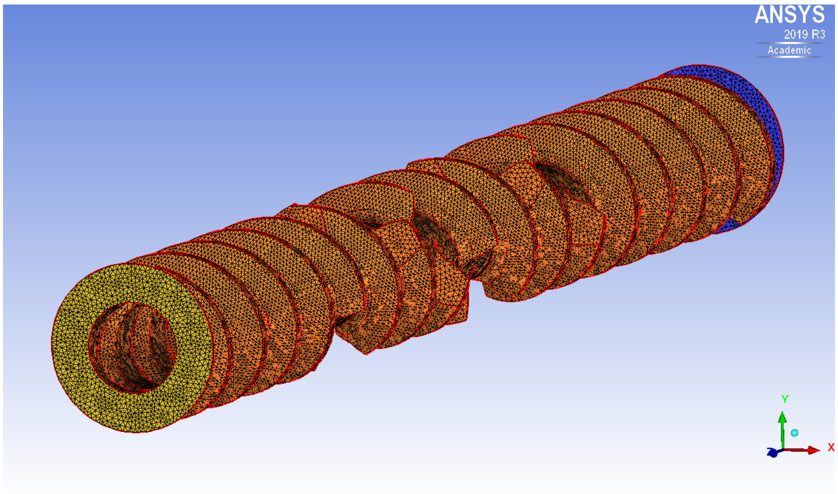

Figure B.7: Representation of the total mesh realized adopting the Robust(Octree) method.

Now it is necessary to analyse in a more detailed way the obtained mesh. For this task we can use the Manage Cut Plane command (Figure B.8), which allows us to cut the mesh obtained and visualize it on a determined slice.

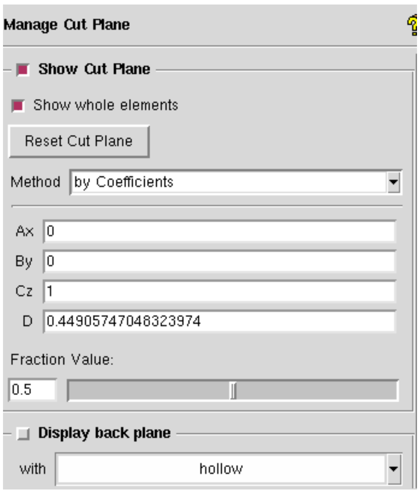

Figure B.8: Manage Cut Plane command present into ANSYS ICEM CFD.

By selecting the slice with the Manage Cut Plane command it was possible to obtain a section where we could analyze the mesh as in Figure B.9.

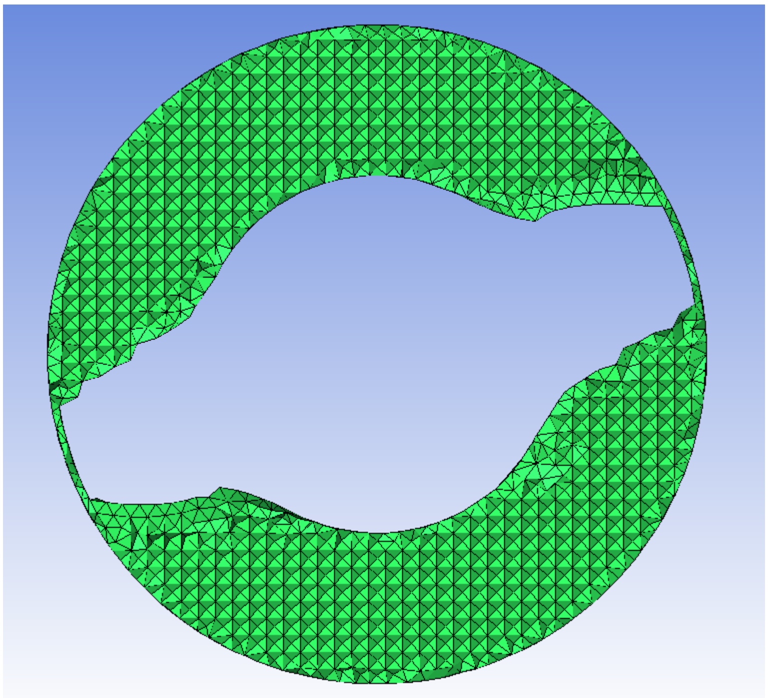

Figure B.9: Representation of the mesh created with the Robust(Octree) method showed on the selected slice.

At this point it was necessary to delete the created mesh to let the method Quick start from the existing mesh. For this reason it was necessary to select the command "Delete Mesh" reported in Figure B.10.

Figure B.10: Delete Mesh command present into ANSYS ICEM CFD.

By pressing this command it is possible to delete the mesh and an empty sheet will be shown. Before returning to the menu where it is possible to select the Quick method it was necessary to set the smoothing. From the same tree showed in the previous picture it was possible to select the "Smoothing Mesh" command (Figure B.11).

Figure B.11: Smoothing Mesh command present into ANSYS ICEM CFD.

After the selection of Smoothing Mesh command the tree reported in Figure B.12 opens.

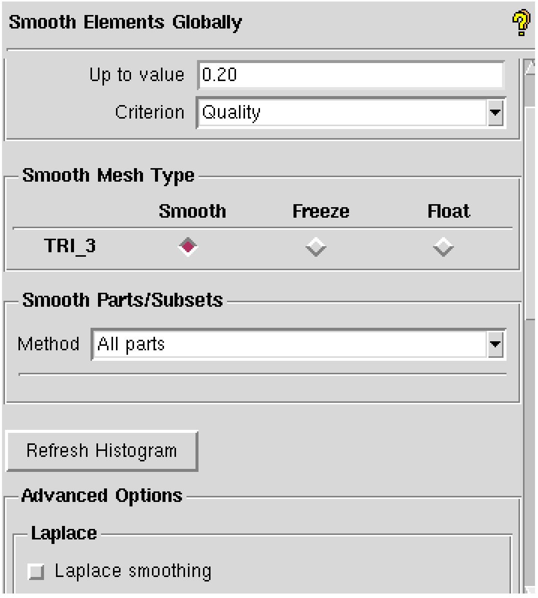

Figure B.12: Tree menu that will appear when pressing the Smoothing Mesh command.

In this tree menu it is really important to select the item ”Laplace Smoothing”. Then, the smoothing can be applied on the mesh and again here the computation is a little bit expensive in cost of time. After this step it is possible to return to the Compute Mesh section and now we can select the Quick method as shown in Figure B.13.

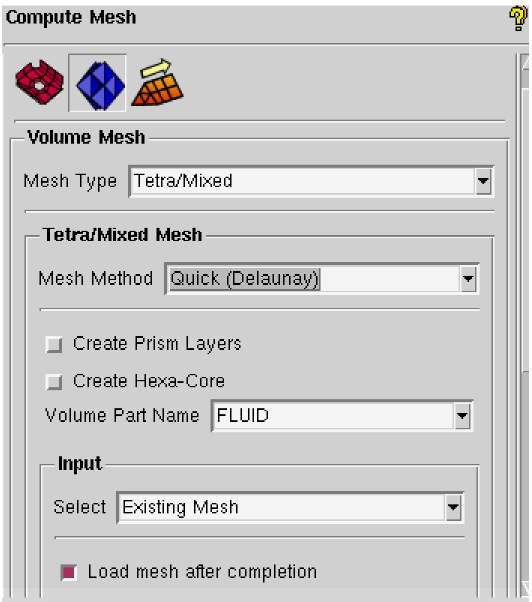

Figure B.13: Selection of the Quick method in the Compute Mesh section.

At this point the mesh will be generated and we have to wait for the end of the computation.

After the creation of the mesh by adopting the Quick method it is possible to analyze the result obtained by applying again a slice with the Manage Cut Plane command. The result is shown in Figure B.14.

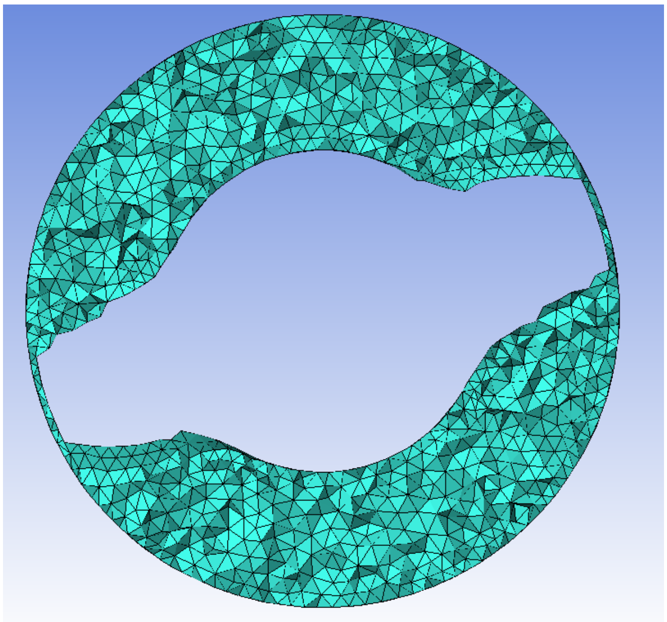

Figure B.14: Representation of the mesh created with the Quick method showed on the selected slice.

As final step it is necessary to compute the prisms set previously and to realize this passage the Prism Mesh command (Figure B.15) in the Compute Mesh section must be selected.

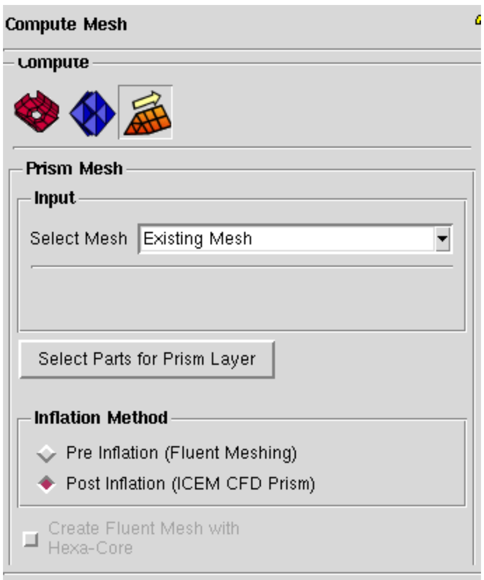

Figure B.15: Prism Mesh command present into ANSYS ICEM CFD.

Finally the total mesh constituted by tetrahedric elements and wedge based ones can be reported in Figure B.16.

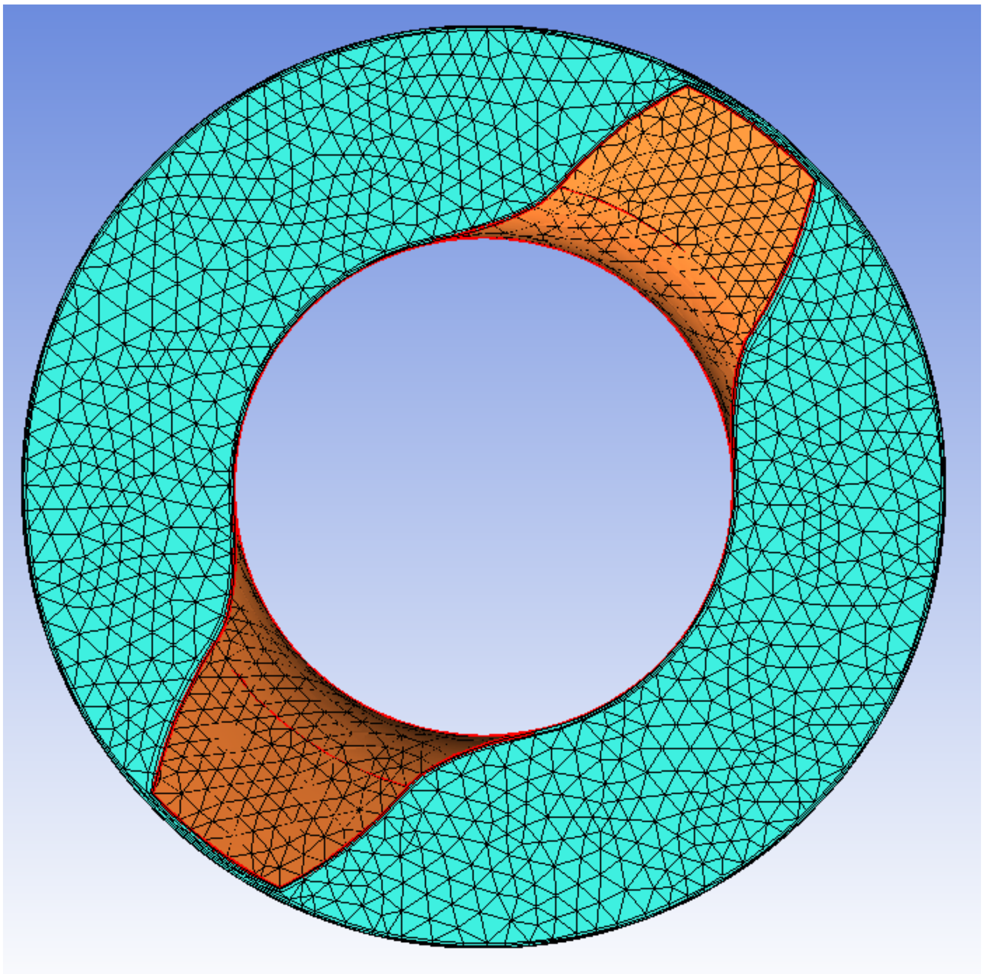

Figure B.16: Representation of the final mesh constituted by tetrahedric elements and wedge based ones.

List of Symbols

Symbol	Description	Unit of measurement
t	time	s
D_b	diameter of the external barrel	m
$D_s = D$	diameter of the screw at the tip of the flight	m
δ_f	clearance (gap)	m
L_s	axial distance of one full turn of the flight (lead)	m
H	channel depth	m
W	perpendicular distance between the flights	m
θ	helix angle	rad
N	frequency of screw rotation	rad/s
V_b	surface velocity of the barrel	m/s
V_{bz}	down channel component of surface velocity of the barrel	m/s
V_{bx}	cross channel component of surface velocity of the barrel	m/s
θ_b	angle to the down channel direction	rad
Q	net flow	m^3/s
Q_d	drag flow	m^3/s
Q_p	pressure flow	m^3/s
F_d	shape factor for drag flow	–
F_p	shape factor for pressure flow	–
μ	dynamic viscosity of the fluid in the channel	Pa s
e	flight width	m
ΔP_s	pressure rise over the screw	Pa
p	Pressure	Pa
$\mathbf{T}$	stress tensor	N/m^2
$\mathbf{f}$	volume force	N/m^3
ρ	Density of the fluid	kg/m^3
$\mathbf{a}$	acceleration	m/s^2
η	dynamic viscosity of the fluid	Pa s
$\mathbf{D}$	rate of deformation tensor	s^{-1}
$\dot{\gamma}$	shear rate	s^{-1}
$\mathbf{v}$	absolut velocity	m/s

$\mathbf{v_r}$	relative velocity	m/s
$\mathbf{u_r}$	whirl velocity	m/s
Ω	angular velocity of the rotating frame	rad/s
$\mathbf{x}$	position vector in the rotating frame	m
c_p	specific heat capacity	J/(K kg)
T	temperature	K
$\mathbf{q}$	heat flux	W/m^2
$\boldsymbol{\sigma}$	Cauchy stress tensor	N/m^2
k	thermal conductivity	W/(m K)
τ	shear stress	N/m^2
F	force applied	N
A	area of cross section	m^2
n	power law index	–
K	flow consistency index	$N\,s^n\,m^{-2}$
η_∞	infinite shear rate viscosity	Pa s
η_0	zero shear rate viscosity	Pa s
τ_0	infinite shear rate viscosity	N/m^2
$\dot{\gamma}_c$	critical shear rate	s^{-1}

Bibliography

[1] Z. Tadmor and I. Klein. *Engineering principles of plasticating extrusion*. Van Nostrand Reinhold Company New York, 1970.

[2] C. Rauwendaal. *Polymer extrusion*. Carl Hanser Verlag GmbH Co KG, 2014.

[3] Z. Tadmor and C. G. Gogos. *Principles of polymer processing*. John Wiley & Sons, 2013.

[4] R. T. Fenner. *Principles of polymer processing*. Chemical Publishing Company, 1980.

[5] R. M. Griffith. Fully developed flow in screw extruders. Theoretical and experimental study. *Industrial & Engineering Chemistry Fundamentals*, 1: 180–187, 1962.

[6] R. E. Colwell and K. R. Nickolls. The screw extruder. *Industrial & Engineering Chemistry*, 51: 841–843, 1959.

[7] H. J. Zamodits and J. R. A. Pearson. Flow of polymer melts in extruders. part i. the effect of transverse flow and of a superposed steady temperature profile. *Transactions of the Society of Rheology*, 13: 357–385, 1969.

[8] R. T. Fenner. The design of large hot melt extruders. *Polymer*, 16: 298–304, 1975.

[9] R. T. Fenner. Developments in the analysis of steady screw extrusion of polymers. *Polymer*, 18: 617–635, 1977.

[10] B. Elbirli and J. T. Lindt. A note on the numerical treatment of the thermally developing flow in screw extruders. *Polymer Engineering & Science*, 24: 482–487, 1984.

[11] J. T. Lindt. Flow of a temperature dependent power-law model fluid between parallel plates: An approximation for flow in a screw extruder. *Polymer Engineering & Science*, 29: 471–478, 1989.

[12] M. V. Karwe and Y. Jaluria. Numerical simulation of fluid flow and heat transfer in a single-screw extruder for non-newtonian fluids. *Numerical heat transfer*, 17: 167–190, 1990.

[13] K. Alemaskin, I. Manas-Zloczower, and M. Kaufman. Color mixing in the metering zone of a single screw extruder: numerical simulations and experimental validation. *Polymer Engineering & Science*, 45: 1011–1020, 2005.

[14] K. M. Dhanasekharan and J. L. Kokini. Design and scaling of wheat dough extrusion by numerical simulation of flow and heat transfer. *Journal of Food Engineering*, 60: 421–430, 2003.

[15] W. G. Yao, K. Takahashi, K. Koyama, and G. C. Dai. Design of a new type of pin mixing section for a screw extruder based on analysis of flow and distributive mixing performance. *Chemical engineering science*, 52: 13–21, 1997.

[16] F. Habla, S. Obermeier, L. Dietsche, O. Kintzel, and O. Hinrichsen. Cfd analysis of the frame invariance of the melt temperature rise in a single-screw extruder. *International Polymer Processing*, 28: 463–469, 2013.

[17] G. Frungieri, G. Boccardo, A. Buffo, D. Marchisio, H. A. Karimi-Varzaneh, and M. Vanni. A CFD-DEM approach to study the breakup of fractal agglomerates in an internal mixer. *The Canadian Journal of Chemical Engineering*, 98: 1880–1892, 2020.

[18] E. M. Mount III. Extrusion processes. In *Applied Plastics Engineering Handbook*, pages 217–264. Elsevier, 2017.

[19] ANSYS, Inc. *ANSYS ICEM CFD User's Manual 19.0, chapter 1: Introduction to ANSYS ICEM CFD*, 2019.

[20] ANSYS, Inc. *ANSYS Polyflow User's Guide 19.0, chapter 1: Getting Started*, 2019.

[21] ANSYS, Inc. *ANSYS Polyflow User's Guide 19.0, chapter 10: Generalized Newtonian Flow*, 2019.

[22] Y. M. Desai, T. Eldho, and A. H. Shah. *Finite element method with applications in engineering*. Pearson Education India, 2011.

[23] ANSYS, Inc. *ANSYS Polyflow User's Guide 19.0, chapter 13: Heat transfer*, 2019.

[24] A. Yahia, S. Mantellato, and R. J. Flatt. Concrete rheology: a basis for understanding chemical admixtures. In *Science and Technology of Concrete Admixtures*, pages 97–127. Elsevier, 2016.

[25] ANSYS, Inc. *ANSYS Polyflow User's Guide 19.0, chapter 21: Flows with Internal Moving Parts*, 2019.

[26] G. Bachler, H. Schiffermüller, and A. Bregant. A parallel fully implicit sliding mesh method for industrial cfd applications. In C.B. Jenssen, H.I. Andersson, A. Ecer, N. Satofuka, T. Kvamsdal, B. Pettersen, J. Periaux, and P. Fox, editors, *Parallel Computational Fluid Dynamics 2000*, pages 501 – 508. North-Holland, Amsterdam, 2001.

[27] ANSYS, Inc. *ANSYS Polyflow User's Guide 19.0, chapter 8: Boundary Conditions*, 2019.

[28] U. Ayachit. *The paraview guide: a parallel visualization application*. Kitware, Inc., 2015.

[29] ANSYS, Inc. *ANSYS Polyflow User's Guide 19.0, chapter 27: Evolution*, 2019.

Acknowledgements

At the end of this long and challenging work I want to thank the people who made it possible. First of all I want to thank my supervisors Marco Vanni and Graziano Frungieri: More precisely I want to thank Marco for the brilliant and technical ideas he had and for managment of the work and Graziano for his high competence and the constant presence during all the year. He was always ready to answer to the thousand of questions I did. In addition I want to thank Dr. Ali Karimi, Dr. Corinna Prange and Dr. Thomas Völker from Contintal AG who gave us important information about the analysed extruder and thank for the conversations we had. Unfortunely my presence there in Hannover could not be possible due to the Covid-19 quarantine. It would have been for sure a good experience. Moreover, I want to thank my family who has always been present to support me and now is tolerating my presence at home in Pescara after 8 years I stayed in Turin. In particular I want to thank my little sister, who teached me what the real sacrifice is. During the period of quarantine I found a person who entered quickly into my life: Maria Andrea. Thank you for the time spent next to me, mainly in the last period where I totally disappeared due to final draft of the thesis. I hope to recover as fast as possible and thank you to support me everyday, with my random talking and my obsessions. Now it is time to thank all my friends. First of all I want to thank my old friends Lorenzo and Niko I grew up with. They have put up with me since 2003 (Niko) and since 2004 (Lorenzo) and they are still here. They should receive a degree "ad honorem" for that. I hope to see you soon and to spend time laughing as we always did. Now it is time to thank my tatooer friend Rebecca, not present physically but always present with her mind. It could be years without a word between us but when we meet it is as if no time had passed. I want to thank my friends Zefe and "The Owl" (Il Falco) for the time we spent together in Turin and the nights we spent random shooting on "Call of Duty". Moreover I want to thank my group of nerds made by Alessandro, Ettorino, Edo, Fabio, Daniele, Roberto, Stefano, Mattia, Jacopo and co.. I want to thank the group of my nerds Now it is time to thank my other family: The "Fulminati" Group which includes the one and only Captain (Big One), Grace Grace (The person with most energy I ever met and with her I always have a reason to laugh), my friend il Cavaliere (Little One) for which I have a deep respect, Lady G (Always sempliciotta) known as "La Matrona" (Nothing more need to be added), Mannalino with his tasty "sfincione" (Unfortunely i didn't eat it), Claudia (The best person in the world with her smile and love), il Camalano (Big fan of technology like me), Angelica (Nerd like me and the one who never took me to play basketball. Already written on the black list), Gaetaaaa (One of the last arrived but as if it had always been there with his symphathy), Sonia (Silent but with a big heart), Gabriele (Pazzo Furioso but the most organised person I ever met), Trunc e Martina (The ones unfortunely with I shared less but always part of the big group) and Stefano (We didn't share a lot of time together but he has my respect). Thank you for the time spent together such as the "Pollame" dinner or the night spent playing "Lupus in Fabula" and similar. I miss you all and thank you to let the Politecnico and Turin become a piece of my heart.